ขั้นตอนวิธีคืนกลับข้อมูลภาพแบบทนทานต่อสัญญาณรบกวนแบบเกาส์และอิมพัลส์ สำหรับคอมเพรสเซนซิง

นางสาวปาริฉัตร เสริมวุฒิสาร

วิทยานิพนธ์นี้เป็นส่วนหนึ่งของการศึกษาตามหลักสูตรปริญญาวิศวกรรมศาสตรดุษฎีบัณฑิต
สาขาวิชาวิศวกรรมไฟฟ้า ภาควิชาวิศวกรรมไฟฟ้า
คณะวิศวกรรมศาสตร์ จุฬาลงกรณ์มหาวิทยาลัย
ปีการศึกษา 2554

ROBUST IMAGE RECONSTRUCTION ALGORITHM IN THE PRESENCE OF GAUSSIAN AND IMPULSIVE NOISE FOR COMPRESSED SENSING

Miss Parichat Sermwuthisarn

A Dissertation Submitted in Partial Fulfillment of the Requirements
for the Degree of Doctor of Philosophy Program in Electrical Engineering
Department of Electrical Engineering
Faculty of Engineering
Chulalongkorn University
Academic Year 2011

Thesis Title	ROBUST IMAGE RECONSTRUCTION ALGORITHM IN THE PRESENCE OF GAUSSIAN AND IMPULSIVE NOISE FOR COMPRESSED SENSING
By	Miss Parichat Sermwuthisarn
Field of Study	Electrical Engineering
Thesis Advisor	Assistance Professor Supatana Auethavekiat, Ph.D.
Thesis Co-advisor	Assistance Professor Vorapoj Patanavijit, Ph.D.

Accepted by the Faculty of Engineering, Chulalongkorn University in Partial Fulfillment of the Requirements for the Doctoral Degree

…….. Dean of the Faculty of Engineering
(Associate Professor Boonsom Lerdhirunwong, Dr.Ing)

THESIS COMMITTEE

…… Chairman
(Associate Professor Mana Sriyudthsak, Ph.D.)

…… Thesis Advisor
(Assistance Professor Supatana Auethavekiat, Ph.D.)

…… Thesis Co-advisor
(Assistance Professor Vorapoj Patanavijit, Ph.D.)

……. Examiner
(Associate Professor Chedsada Chinrungrueng, Ph.D.)

……. External Examiner
(Duangrat Gansawat, Ph.D.)

……. External Examiner
(Sanparith Marukatat, Ph.D.)

ปาริฉัตร เสริมวุฒิสาร : ขั้นตอนวิธีคืนกลับข้อมูลภาพแบบทนทานต่อสัญญาณรบกวนแบบเกาส์และอิมพัลส์สำหรับคอมเพรสเซนซิง. (ROBUST IMAGE RECONSTRUCTION ALGORITHM IN THE PRESENCE OF GAUSSIAN AND IMPULSIVE NOISE FOR COMPRESSED SENSING) อ. ที่ปรึกษาวิทยานิพนธ์หลัก: ผศ.ดร.สุพัฒนา เอื้อทวีเกียรติ, อ. ที่ปรึกษาวิทยานิพนธ์ร่วม: ผศ.ดร.วรพจน์ พัฒนวิจิตร, 88 หน้า.

วิทยานิพนธ์นี้นำเสนอขั้นตอนวิธีคืนกลับข้อมูลภาพแบบคอมเพรสเซนซิงที่ทนทานต่อสัญญาณรบกวนแบบเกาส์ และ/หรือ อิมพัลส์ โดยส่วนแรกกล่าวถึงขั้นตอนวิธีคืนกลับข้อมูลภาพที่ทนทานต่อสัญญาณรบกวนแบบเกาส์ โดยเริ่มจากการสร้างชุดข้อมูลของสัญญาณที่บีบอัดจำนวน L ชุด จากสัญญาณบีบอัดที่ได้รับหนึ่งสัญญาณ แต่ละสัญญาณที่สร้างขึ้นจะทำการคืนกลับแบบอิสระต่อกัน จากนั้นทำการหาค่าเฉลี่ยรวมของสัญญาณคืนกลับ เพื่อลดผลกระทบจากสัญญาณรบกวนแบบเกาส์ ผลการทดลองโดยวัดจากค่า PSNR และภาพที่สร้างคืนกลับ ของภาพทดสอบ 40 ภาพ แสดงให้เห็นว่า ขั้นตอนวิธีที่นำเสนอนั้นสามารถสร้างภาพคืนกลับที่มีคุณภาพของภาพดีขึ้นได้

ส่วนที่สองของวิทยานิพนธ์ที่นำเสนอเกี่ยวกับขั้นตอนวิธีการสร้างสัญญาณคืนกลับที่ทนทานต่อสัญญาณรบกวนแบบอิมพัลส์ เนื่องจากขั้นตอนการสร้างคืนกลับสัญญาณที่ทนทานต่อสัญญาณรบกวนแบบอิมพัลส์แบบดั้งเดิม มักประยุกต์ใช้ Lorentzian norm ซึ่งเป็น Robust statistics แต่ทว่าการ Optimization ของวิธีดังกล่าวมีความซับซ้อน และมีความยุ่งยากในการปรับค่าตัวแปรต่าง ๆ ในวิทยานิพนธ์นี้ได้นำเสนอขั้นตอนการทำ Preprocessing เพื่อกำจัดสัญญาณรบกวนแบบอิมพัลส์จากสัญญาณที่บีบอัด การแปลงเวฟเล็ตแบบต้นไม้ถูกนำมาใช้สร้างสัญญาณกลวง ซึ่งทำให้เกิดสัญญาณกลวงมีรูปแบบที่คงตัว เมื่อสัญญาณบีบอัดถูกรบกวนจากสัญญาณรบกวนแบบอิมพัลส์ สัญญาณคืนกลับ (สัญญาณกลวง) จะมีการรูปแบบกระจายตัวของพลังงานที่เปลี่ยนแปลงจากเดิมมาก ดังนั้นรูปแบบการกระจายตัวของพลังงานสามารถใช้ในการตรวจสอบการถูกรบกวนได้ หลังจากตรวจพบตำแหน่งที่ถูกรบกวนในสัญญาณบีบอัดแล้ว จะทำการประมาณ และแทนค่ากลับไปยังตำแหน่งที่ตรวจพบ โดยขั้นตอนวิธีที่นำเสนอนี้ในส่วนนี้ ไม่มีการทำ Optimization ที่ซับซ้อน และมีการปรับค่าตัวแปรอย่างง่าย

ทั้งนี้ ในกรณีที่ถูกรบกวนจากทั้งสัญญาณรบกวนแบบเกาส์ และอิมพัลส์ สองขั้นตอนวิธีที่นำเสนอข้างต้นสามารถประยุกต์ใช้ร่วมกันเพื่อลดผลกระทบต่อสัญญาณรบกวนได้

ภาควิชา	วิศวกรรมไฟฟ้า	ลายมือชื่อนิสิต	
สาขาวิชา	วิศวกรรมไฟฟ้า	ลายมือชื่อ อ.ที่ปรึกษาวิทยานิพนธ์หลัก	
ปีการศึกษา	2554	ลายมือชื่อ อ.ที่ปรึกษาวิทยานิพนธ์ร่วม	

5171817621 : MAJOR ELECTRICAL ENGINEERING
KEYWORDS : COMPRESSED SENSING (CS)/ MODEL-BASED METHOD/ ORTHOGONAL MATCHING PURSUIT WITH PARTIALLY KNOWN SUPPORT (OMP-PKS)/ DISTRIBUTED COMPRESSED SENSING/ GAUSSIAN NOISE/ IMPULSIVE NOISE

PARICHAT SERMWUTHISARN: ROBUST IMAGE RECONSTRUCTION ALGORITHM IN THE PRESENCE OF GAUSSIAN AND IMPULSIVE NOISE FOR COMPRESSED SENSING. ADVISOR: ASST. PROF. SUPATANA AUETHAVEKIAT, Ph.D., CO-ADVISOR: ASST. PROF. VORAPOJ PATANAVIJIT, Ph.D., 88 pp.

The Compressed Sensing (CS) reconstruction methods robust to Gaussian and/or impulsive noise are proposed in this dissertation. In the first part, the reconstruction in the Gaussian noise environment is proposed. The compressed measurement signal is subsampled for L times to create the ensemble of L compressed measurement signals. Orthogonal Matching Pursuit with Partially Known Support (OMP-PKS) is applied to each signal in the ensemble to reconstruct L noisy outputs. The L noisy outputs are then averaged for Gaussian denoising. The proposed method was evaluated on 40 test images and found to improve both PSNR and visual quality of the reconstructed results.

In the second part of this dissertation, the reconstruction in the impulsive noise environment is investigated. In conventional methods, the impulsive noise tolerance is acquired by using the Lorentzian norm of robust statistics. The optimization of the robust statistic function is iterative and usually requires complex parameter adjustments. In this part, the impulsive noise rejection for the compressed measurement signal with the design for image reconstruction is proposed. It is used as the preprocessing for any compressed sensing reconstruction given that the sparsified version of the signal is obtained by utilizing octave-tree discrete wavelet transform with db8 as the mother wavelet. The presence of impulsive noise is detected from the energy distribution of the reconstructed sparse signal. After the noise removal, the noise corrupted coefficients are estimated. Moreover, the proposed method requires neither complex optimization nor complex parameter adjustments.

In addition, the two proposed methods can be combined to create the reconstruction robust to both Gaussian and impulsive noise.

Department :	Electrical Engineering	Student's Signature	.....
Field of Study :	Electrical Engineering	Advisor's Signature	.....
Academic Year :	2011	Co-advisor's Signature	.....

ACKNOWLEDGEMENTS

This work contained in this dissertation represents the accumulation of four years of work made possible only by the collective support of family, mentors, friends, colleagues. First, I would like to express my deep gratitude to my advisor Asst. Prof. Dr. Supatana Auethavekiat and Dr. Duangrat Gansawat. It was a great privilege and honor to work and study under their guidance. I would like to thank them for their support, friendship, empathy and great vision.

My thanks also to my co-advisor, Asst. Prof. Dr. Vorapoj Patanavijit, and the other members of my dissertation defense committees: Assoc. Prof. Dr. Mana Sriyudthsak, Assoc. Prof. Dr. Chedsada Chinrungreung and Dr. Sanparith Marukatat for reviews and invaluable comments.

Several other people helped in the production of this dissertation. In particular, I thank Dr. Sopon Phumeechanya for his insightful suggestions and supports. I am grateful to Suwichaya Suwanwimonkul for many interesting discussions and help in the presentation preparation. I thank Thanissorn Panarungsun for her support. Many thanks to all my colleagues at DSPRL (Digital Signal Processing Research Laboratory) for academic documentary help, technical/theory information and programming/data information.

I also would like to acknowledge the Telecommunications Research Industrial and Development Institute (TRIDI) for National Telecommunications Commission Fund.

Finally, my life has been constantly fulfilled by love and support of my family. I am extremely grateful to my parents, Peera Sermwuthisarn and Prapaporn Naranuwat, for their love, caring, sacrifices, education and preparing me for my future life since I was a kid. This work is dedicated to them

.

CONTENTS

Page

Page

List of Tables

List of Figures

Figure Page

Figure Page

Figure Page

Figure Page

CHAPTER I
INTRODUCTION

1.1 Introduction

Compressed sensing (CS) is a sampling paradigm that provides compressible signals at a rate significantly below the Nyquist rate. It reveals that a compressible or sparse signal can be recovered by a small amount of measurements [1]-[3]. The connection between sampling and reconstruction methods of CS and those of other sparse signal processing is presented in [4]. The description of commonly used reconstruction algorithms is also given. Consider a measurement process in CS that is modeled as

$$\mathbf{y} = \mathbf{\Phi x}, \tag{1.1}$$

where $\mathbf{y}$ and $\mathbf{\Phi}$ are an $M\times 1$ compressed measurement signal and an $M\times N$ random measurement matrix, respectively; $\mathbf{x}$ is an $N\times 1$ compressible signal. In CS, it is considered that $M < N$. A signal is compressible if it is sparse in some domain; thus, $\mathbf{x}$ can be written as follows.

$$\mathbf{x} = \mathbf{\Psi s}, \tag{1.2}$$

where $\mathbf{s}$ and $\mathbf{\Psi}$ are a k-sparse signal and an $N\times N$ orthogonal basis matrix, respectively. k is the number of non-zero elements or a sparsity level. Without loss of generality, $\mathbf{\Psi}$ is defined as an identity matrix in this dissertation and $\mathbf{x}$ is equivalent to $\mathbf{s}$.

In practice, $\mathbf{y}$ can be corrupted by noise during transmission in a noisy channel. The measurement process in the noisy channel is modeled as

$$\mathbf{y} = \mathbf{\Phi s} + \mathbf{e}, \tag{1.3}$$

where $\mathbf{e}$ is the additive noise.

CS reconstruction methods aim to find the sparsest **s** that creates **y**. The reconstruction of **s** in the noisy channel can be written as the following optimization problems.

$$\arg\min_{\mathbf{s}} \|\mathbf{s}\|_0 \, s.t. \, \|\mathbf{y} - \mathbf{\Phi s}\|_2 \le \varepsilon, \tag{1.4}$$

where ε and $\|\mathbf{u}\|_P$ are the error bound and the L_P norm of **u**, respectively. The error bound is set based on the noise characteristics, such as bounded noise, Gaussian noise, finite variance noise, etc [5]-[15]. L_0 norm in equation (1.4) is relaxed to L_1 norm in the reconstruction by Basis Pursuit Denoising (BPDN); whereas, it is replaced by heuristic rules in the reconstruction by greedy algorithms.

The optimization problems in BPDN [7] is given

$$\arg\min_{\mathbf{s}} \|\mathbf{s}\|_1 \, s.t. \, \|\mathbf{y} - \mathbf{\Phi s}\|_2 \le \varepsilon, \tag{1.5}$$

which is equivalent to

$$\arg\min_{\mathbf{s}} \frac{1}{2}\|\mathbf{y} - \mathbf{\Phi s}\|_2^2 + \tau \|\mathbf{s}\|_1, \tag{1.6}$$

where τ is a regularization parameter.

When $\mathbf{\Phi}$ satisfies the Restricted Isometry Property (RIP) condition [7], the BP approach is an effective reconstruction approach and does not require the exactness of the sparse signal. However, it requires high computation. In the greedy approach [8][16], the heuristic rule is used in place of L_1 optimization. One of the popular heuristic rules is that the non-zero components of **s** correspond to the coefficients of the random measurement vectors having the high correlation to **y**. The examples of greedy algorithm are OMP [16], Regularized OMP (ROMP) [8], etc. The greedy approach has the benefit of fast reconstruction.

The reconstruction of the noisy compressed measurement signals requires the relaxation of the $\mathbf{y} - \mathbf{\Phi s}$ constraint. Most algorithms provide the acceptable bound for

the error between **y** and **Φs** [5]-[13]. The error bound is created based on the noise characteristic such as bounded noise, Gaussian noise, finite variance noise, etc. The authors in [5] show that it is possible to use BP and OMP to reconstruct the noisy signals, if the conditions of the sufficient sparsity and the structure of the overcompleted system are met. The sufficient conditions of the error bound in BPDN for successful reconstruction in the presence of Gaussian noise is discussed in [9]. In [10], the Danzig selector is used as the reconstruction technique. L_∞ norm is used in place of L_2 norm.

OMP is robust to the small Gaussian noise in **y** due to its L_2 optimization during parameter estimation. Regularized OMP (ROMP) [8][13] and Compressed Sensing Matching Pursuit (CoSaMP) [11][13] have the stability guarantee as the L_1-minimization method and provide the speed as greedy algorithm. In [12], the authors used the mutual coherence of the matrix to analyze the performance of BPDN, OMP, and Iterative Hard Thresholding (IHT) when **y** was corrupted by Gaussian noise. The equivalent of cost function in BPDN was solved through IHT in [14]. IHT gives faster computation than BPDN but requires very sparse signal.

When the noise is impulsive noise, **e** in equation (1.3) is considered to be very large. It is well known that the optimization of L_2 norm is not robust to outliers in **y**; thus, the optimization leads to the incorrect result of **s**. In [17], the reconstruction from the signal corrupted by the impulsive noise is performed by solving one of the following two optimization problems.

$$\arg\min_{\mathbf{s},\mathbf{e}_\delta} \frac{1}{2\alpha}\left\|\mathbf{y}-\mathbf{\Phi s}-\mathbf{e}_\delta\right\|_2^2+\left\|\mathbf{e}_\delta\right\|_1+\tau\left\|\mathbf{s}\right\|_1, \tag{1.7}$$

$$\arg\min_{\mathbf{s},\mathbf{e}_\delta} \frac{1}{2\alpha}\left\|\mathbf{y}-\mathbf{\Phi s}-\mathbf{e}_\delta\right\|_2^2+\left\|\mathbf{e}_\delta\right\|_1+\tau\left\|\mathbf{s}\right\|_{\mathrm{TV}} \tag{1.8}$$

where $\mathbf{e}_\delta$ and α are a sparse vector with large non-zero coefficients (impulsive noise) and a pre-defined threshold, respectively; $\left\|\mathbf{u}\right\|_{\mathrm{TV}}$ is a total variation norm of **u**. First, this method estimates **s** and then estimates $\mathbf{e}_\delta$. The estimation is performed

iteratively. However, the unique solution is guaranteed only when the cost function is convex. The effect of impulsive noise can be suppressed by applying robust statistics [18]-[24]. The Generalized Cauchy Distribution (GCD) based Maximum Likelihood (ML) has been proposed as the optimization algorithm that is robust to impulsive noise [18]. The Lorentzian norm, which is the special case of GCD, is utilized in a number of robust CS reconstructions [20]-[24]. The Lorentzian norm is used in place of L_2 norm in equation (1.5) for the Lorentzian based Basis Pursuit (LBP) [20]. Similar to Basis Pursuit (BP), the LBP is slow to solve. Furthermore, it requires complex parameter adjustments for the effective optimization of the Lorentzian norm. The reconstruction in [21]-[22] applies the iterative algorithm and the weighted myriad operator to solve the following problem.

$$\arg\min_{\mathbf{s}} \left\| \mathbf{H} - \mathbf{R}^T \mathbf{s} \right\|_{LL} + \tau \left\| \mathbf{s} \right\|_0 , \tag{1.9}$$

where $\left\| \mathbf{u} \right\|_{LL}$, $\mathbf{H}$ and $\mathbf{R}$ are the Lorentzian norm of $\mathbf{u}$, a Cauchy random projection signal and a Cauchy random projection matrix, respectively. The reconstruction in [23] applies the weighted median operator and the iterative thresholding to solve the following L_0-regularized Least Absolute Deviation (L_0-LAD) regression problem.

$$\arg\min_{\mathbf{s}} \left\| \mathbf{y} - \mathbf{\Phi s} \right\|_1 + \tau \left\| \mathbf{s} \right\|_0 , \tag{1.10}$$

The Lorentzian based Iterative Hard Thresholding (LIHT) approach is proposed as the fast reconstruction method in [24]. Iterative Hard Thresholding (IHT) is used in place of BP to increase the speed of LBP. However, it faces the same problem as IHT [14]. Consequently, LIHT is suitable for very sparse signals.

1.2 Objectives

1) To propose the robust compressed sensing (CS) reconstruction method for images corrupted by Gaussian noise.

2) To propose the robust CS reconstruction method for images corrupted by impulsive noise.

3) To propose the robust CS reconstruction method for images corrupted by both Gaussian and impulsive noise.

1.3 Problem Statements

The methods robust to Gaussian noise are based on the solution of L_1 minimization. No method makes use of the fact that the signal can be reconstructed from parts of **y** instead of the entire signal. From one given signal, multiple signals can be reconstructed. Each signal can be considered as a signal corrupted by the same noise at different instance. By merging these signals, more accurate signal can be reconstructed.

The robust statistic provides the tolerance against impulsive noise; however, its optimization problem is non-convex. When a compressed measurement signal is corrupted by the impulsive noise, the reconstructed signal has different energy distribution in wavelet domain. When the octave-tree discrete wavelet transform is used to transform signals to sparse domain, the reconstruction from a noise corrupted signal leads to high energy leaking outside the third level subband. Hence, the detection of high energy outside the third level subband can be used in place of robust statistic to detect and remove the impulsive noise.

1.4 Contributions

1) Propose the ideas of subsampling and sampling with replacement in the reconstruction robust to Gaussian noise.

2) Propose the ratio between the energy leaking outside the third-level subband and the total signal energy to detect the presence of impulsive noise in the compressed measurement signal.

1.5 Scopes

1) The proposed CS is for gray-scale image only.

2) The sparse domain is wavelet domain.

3) The compressed measurement signal is corrupted by Gaussian and/or impulsive noises.

4) The magnitude of impulsive noise must be at least five times higher than the peak of signal.

5) The process is performed off-line.

1.6 Research Procedures

1) Study previous research papers relevant to the research works of the dissertation**.**

    1.1) Papers on the fundamental of CS.

    1.2) Papers on applying CS to image.

    1.3) Papers on CS reconstruction of noisy signal.

2) Develop CS reconstruction algorithm in noiseless case.

3) Test the proposed algorithm in Step 2 on 1-D signals.

4) Test the proposed algorithm in Step 2 on standard tested images such as Lena, Peppers, Mandrill, etc.

5) Develop CS reconstruction algorithm in the presence of zero-mean white Gaussian noise.

6) Test the proposed algorithm in Step 5 on standard tested images

7) Develop CS reconstruction algorithm in the presence of impulsive noise.

8) Test the proposed algorithm in Step 7.

9) Collect and analyze computational results obtained from simulation programs.

10) Summarize the major findings as we found in Step 9 and conclude the performance of the proposed CS reconstruction algorithm in all concerned aspects.

11) Check whether the conclusions meet all the objectives of the research work of the dissertation.

12) Write the dissertation.

CHAPTER II

BACKGROUND

This chapter addresses the related research of the dissertation. It is divided into two parts. The compressed sensing theory is described in Section 2.1. The examples of reconstruction method are then given in Section 2.2 where five popular reconstruction methods are described.

2.1 Compressed Sensing

CS is based on the assumption of the sparse property of signals and incoherency between the basis of the sparse domain and the basis of measurement vectors [1]-[3]. CS has three major steps: (1) the construction of *k*-sparse representation, (2) the measurement and (3) the reconstruction. The first step is the construction of the *k*-sparse representation, where *k* is the number of non-zero component of the sparse signal. Most natural signals can be made sparse by applying orthogonal transforms such as wavelet transform, Fast Fourier Transform (FFT), or Discrete Cosine Transform (DCT). This step is represented as previous equation (1.2).

Next step, the random measurement matrix is applied to measure the signal by the following equation.

$$\mathbf{y} = \mathbf{\Phi x} = \mathbf{\Phi \Psi s} \tag{2.1}$$

Since $\mathbf{\Psi}$ is an identity matrix in this dissertation, **s** is equivalent to **x**. The sufficient condition for the high probability of successful reconstruction is as follows.

$$M \geq C\mu^2(\mathbf{\Phi}, \mathbf{\Psi})k \log N, \tag{2.2}$$

for some positive constant *C*. *M* and *N* are the number of measurement and the dimension of sparse signal, respectively. $\mu(\mathbf{\Phi}, \mathbf{\Psi})$ is the coherence between $\mathbf{\Phi}$ and $\mathbf{\Psi}$, and defined by

$$\mu(\mathbf{\Phi},\mathbf{\Psi}) = \sqrt{N}\max_{i,j}\left|\left\langle \varphi_i, \psi_j \right\rangle\right|, \tag{2.3}$$

where φ_i and ψ_j are the *i*-th and the *j*-th column in $\mathbf{\Phi}$ and $\mathbf{\Psi}$, respectively. $\langle A, B\rangle$ stands for the dot product between *A* and *B*. If the elements in $\mathbf{\Phi}$ and $\mathbf{\Psi}$ are correlated, the coherence is large. Otherwise, it is small. From linear algebra, it is known that $\mu(\mathbf{\Phi},\mathbf{\Psi}) \in \left[1, \sqrt{N}\right]$[2]. In the measurement process, the error (due to hardware noise, transmission error, etc.) may occur. The error is added into the compressed measurement vector as described in equation (1.3).

The final step is the reconstruction. There are two major reconstruction approaches: L_1-minimization [5] and greedy algorithm [11]. Convex optimization is applied in the reconstruction by L_1-minimization approach. The successful reconstruction depends on the degree that $\mathbf{\Phi}$ complies with the Restricted Isometry Property (RIP). RIP is defined as follows.

$$(1-\delta_k)\|\mathbf{s}\|_2^2 \le \|\mathbf{\Phi s}\|_2^2 \le (1+\delta_k)\|\mathbf{s}\|_2^2, \tag{2.4}$$

where δ_k is the *k*-restricted isometry constant of $\mathbf{\Phi}$. RIP is used to ensure that all subsets of k columns taken from $\mathbf{\Phi}$ are nearly orthogonal. It should be noted that $\mathbf{\Phi}$ has more columns than rows; thus, $\mathbf{\Phi}$ cannot be exactly orthogonal [2].

2.2 Reconstruction Methods

A number of reconstruction methods have been proposed for CS reconstruction. They can be divided into two main categories: (1) L_1 optimization and (2) the heuristic method. Five reconstruction methods are presented in this section. They are Basis Pursuit DeNoising (BPDN), Orthogonal Matching Pursuit (OMP), OMP with Partially Known Support (OMP-PKS), Lorentzian based Iterative Hard Thresholding (LIHT) and Distributed Compressed Sensing Simultaneous OMP (DCS-SOMP). BPDN is one of the popular reconstruction methods based on L_1 optimization. It is designed for the bounded noisy signal. OMP is one of the popular reconstruction

methods based on heuristic rules. OMP-PKS is the variant of OMP. The advantage of OMP-PKS is the ability to reconstruct the signal with lower measurement rate than the original OMP. LIHT is the reconstruction method that is designed for general noisy signal. LIHT has the advantage over the other four methods in that it can be used in the unbounded noise environment. The example of the unbounded noise is the impulsive noise. DCS-SOMP is the example of the reconstruction method using signal ensemble.

2.2.1 Basis Pursuit Denoising (BPDN)

Basis Pursuit (BP) [5] is one of the popular L_1-minimization methods. The main idea of this algorithm is to relax the L_0-norm in (2.5) to L_1-norm.

$$\arg\min_{s} \|\mathbf{s}\|_0 \; s.t. \;\; \mathbf{y} = \mathbf{\Phi s} \tag{2.5}$$

It reconstructs the signal by solving the following problem.

$$\arg\min_{s} \|\mathbf{s}\|_1 \; s.t. \;\; \mathbf{y} = \mathbf{\Phi s} \tag{2.6}$$

BPDN [6] is the relaxed version of BP and is the reconstruction method for the noisy **y**. It reconstructs the signal by solving the following optimization problem.

$$\arg\min_{x} \|\mathbf{s}\|_1 \;\; s.t. \;\; \|\mathbf{y} - \mathbf{\Phi s}\|_2 \le \varepsilon, \tag{2.7}$$

where ε is the error bound.

BPDN is often solved by linear programming. It guarantees a good reconstruction if $\mathbf{\Phi}$ satisfies RIP condition. However, it has the high computational cost as BP.

2.2.2 Orthogonal Matching Pursuit (OMP)

OMP is a well known reconstruction algorithm [16]. It was developed from Matching Pursuit (MP) [33] u sing different method to estimate the magnitude of the non-zero elements in **s**. Instead of projecting the residual signal onto the selected

basis, it estimates the magnitude of the non-zero elements by solving the least squared error between the projection of the reconstructed **s** and **y**. OMP has the advantage of simple and fast implementations. The algorithm is as follows.

Input:

- The $M \times N$ measurement matrix, $\mathbf{\Phi} = [\varphi_1 \quad \varphi_2 \quad ... \quad \varphi_N]$
- The M-dimension compressed measurement signal, $\mathbf{y}$
- The sparsity level of the sparse signal, k

Output:

- The reconstructed signal, $\hat{\mathbf{s}}$
- The set containing k indexes of non-zero elements in $\hat{\mathbf{s}}$, $\Lambda_k = \{\lambda_1, \lambda_2, ..., \lambda_k\}$

Procedure:

a) Initialize the residual ($\mathbf{r}_0$), the index set (Λ_0) and the iteration counter (t) as follows.

$$\mathbf{r}_0 = \mathbf{y}, \Lambda_0 = \varnothing, t = 1$$

b) Find the index λ_t of the measurement basis that has the highest correlation to the residual in the previous iteration, $\mathbf{r}_{t-1}$.

$$\lambda_t = \arg \max_{j=1,...,N} \left| \left\langle \mathbf{r}_{t-1}, \varphi_j \right\rangle \right|$$

If the maximum occurs in multiple bases, select one deterministically.

c) Augment the index set and the matrix of chosen bases: $\Lambda_t = \Lambda_{t-1} \bigcup \{\lambda_t\}$ and $\mathbf{\Phi}_t = \left[\mathbf{\Phi}_{t-1} \quad \varphi_{\lambda_t} \right]$, where $\mathbf{\Phi}_0$ is an empty matrix.

d) Solve the following least squared problem to obtain the new reconstructed signal, $\mathbf{z}_t$.

$$\mathbf{z}_t = \arg \min_z \left\| \mathbf{y} - \mathbf{\Phi}_t \mathbf{z} \right\|_2$$

e) Calculate the new approximation, $\mathbf{a}_t$, that best describes $\mathbf{y}$. Then, calculate the residual of the t-th iteration, $\mathbf{r}_t$.

$$\mathbf{a}_t = \mathbf{\Phi}_t \mathbf{z}_t$$
$$\mathbf{r}_t = \mathbf{y} - \mathbf{a}_t$$

f) Increment t by one.

g) If $t > k$, terminate; otherwise, go to step b).

The reconstructed signal, $\hat{\mathbf{s}}$, has non-zero elements at the indexes listed in Λ_k. The value of the λ_j-th elements in $\hat{\mathbf{s}}$ equals to the j-th element of $\mathbf{z}_k$ $\left(j = 1, 2, ..., k\right)$. The termination criterion can be changed from $t > k$ to that $\mathbf{r}_{t-1}$ is less than the predefined threshold.

2.2.3 OMP with Partially Known Support (OMP-PKS)

The noise tolerance can be increased by including *a priori* information. One of the popular knowledge is the model of a sparse signal [25], such as the wavelet-tree structure. Model based reconstruction methods have three benefits: (1) the reduction of the number of measurements, (2) the increase in robustness and (3) the faster reconstruction.

OMP-PKS [30] is adapted from the classical OMP [16]. The partially known support gives *a priori* information to determine which subbands in the sparse signal structure are more important than the others and should be selected as non-zero elements. It has the characteristic of OMP that the requirement of RIP is not as severe as BP's [5]. It has a fast implementation but may fail to reconstruct the signal (lacks stability). It requires very low measurement rate. It is different from Tree-based OMP (TOMP) [26] in that the subsequent basis selection of OMP-PKS does not consider the previously selected bases, while TOMP sequentially compares and selects the next good wavelet sub-tree and the group of related atoms in the wavelet tree.

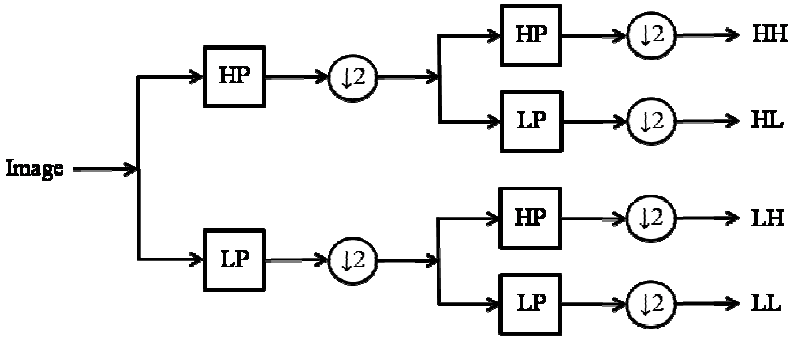

Figure 2.1: Wavelet decomposition by filter bank analysis. HP and LP are high pass filter and low pass filter, respectively.

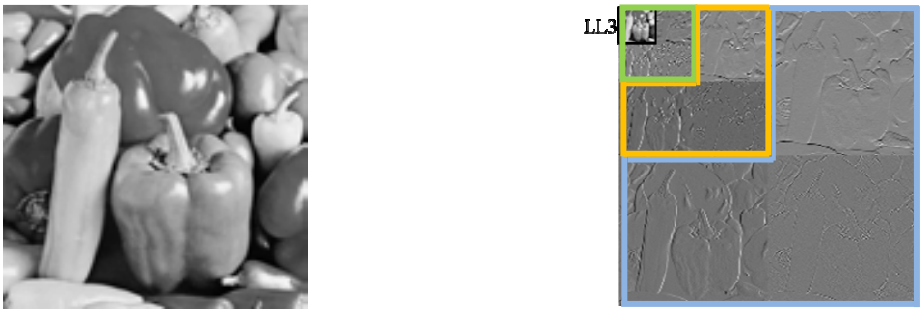

(a) (b)

Figure 2.2: The example of octave-tree discrete wavelet transform; (a) the original image and (b) the wavelet transformed image. Subbands inside the blue, orange and green windows are the first, the second and the third level subbands, respectively.

The wavelet transform of an image is realized using filter banks as shown in Figure 2.1. The image is decomposed into four subbands: HH, HL, LH and LL. The HH, HL, LH and LL subbands contain diagonal details, vertical details, horizontal details and approximation coefficients, respectively. In this paper, octave-tree discrete wavelet transform (DWT) is used to obtain the sparse representation of images. The second and the third level subbands are constructed by applying the filter bank

analysis to the LL subband in the first and the second level, respectively. The example of octave-tree discrete wavelet transform is shown in Figure 2.2. The original image and the wavelet transformed image are shown in Figures 2.2(a) and 2.2(b), respectively. Since the LL subband in the third level (LL_3 subband) contains most information in the image, the signal in the LL_3 subband must be included for successful reconstruction. All elements in the LL_3 subband are selected as non-zero elements without testing for the correlation. The algorithm for OMP-PKS when the data are represented in wavelet domain is as follows.

Input:

- The $M \times N$ measurement matrix, $\mathbf{\Phi} = [\varphi_1 \quad \varphi_2 \quad ... \quad \varphi_N]$
- The M-dimension compressed measurement signal, $\mathbf{y}$
- The sparsity level of the sparse signal, k
- The set containing the indexes of the bases in LL_3 subbands, $\Gamma = \{\gamma_1, \gamma_2, ..., \gamma_{|\Gamma|}\}$

Output:

- The reconstructed signal, $\hat{\mathbf{s}}$
- The set containing k indexes of the non-zero element in $\hat{\mathbf{s}}$, $\Lambda_k = \{\lambda_1, \lambda_2, ..., \lambda_k\}$

Procedure:

Phase 1: Selection without correlation test

a) Select every basis in the LL_3 subband.

$$t = |\Gamma|$$

$$\Lambda_t = \Gamma$$

$$\mathbf{\Phi}_t = \left[\varphi_{\gamma_1} \quad \varphi_{\gamma_2} \quad ... \quad \varphi_{\gamma_t}\right]$$

b) Solve the least squared problem to obtain the new reconstructed signal, $\mathbf{z}_t$.

$$\mathbf{z}_t = \arg\min_z \|\mathbf{y} - \mathbf{\Phi}_t \mathbf{z}\|_2$$

c) Calculate the new approximation, $\mathbf{a}_t$, and find the residual (error, $\mathbf{r}_t$). $\mathbf{a}_t$ is the projection of $\mathbf{y}$ on the space spanned by $\mathbf{\Phi}_t$.

$$\mathbf{a}_t = \mathbf{\Phi}_t \mathbf{z}_t$$
$$\mathbf{r}_t = \mathbf{y} - \mathbf{a}_t$$

Phase 2: Reconstruction by OMP

a) Increment t by one, and terminate if $t > k$.

b) Apply steps b) - g) of OMP described in Section 2.2.2 to find the remaining $k - |\Gamma|$ non-zero elements of $\hat{\mathbf{s}}$.

The reconstructed sparse signal, $\hat{\mathbf{s}}$, has the indexes of non-zero elements listed in Λ_k. The value of the λ_j-th element of $\hat{\mathbf{s}}$ equals to the j-th element of $\mathbf{z}_k$.

2.2.4 Lorentzian based Iterative Hard Thresholding (LIHT)

LIHT [24] was proposed to reconstruct signals in the presence of Gaussian and impulsive noise. It differs from IHT in the usage of Lorentzian norm instead of L_2norm. It reconstructs the signal according to the following function.

$$\arg\min_{\mathbf{s}} \|\mathbf{y} - \mathbf{\Phi s}\|_{LL_2,\alpha} \text{ s.t. } \|\mathbf{s}\|_0 \le k \tag{2.8}$$

where $\|u\|_{LL_2,\alpha}$ is Lorentzian norm (LL_q norm with q (tail parameter) = 2) of u and defined as follows.

$$\|u\|_{LL_2,\alpha} = \log\left(1 + \frac{1}{2}\left(\frac{u}{\alpha}\right)^2\right), \tag{2.9}$$

where α is a scale parameter. The algorithm for LIHT is as follows.

Input:

- The $M \times N$ measurement matrix, $\mathbf{\Phi} = [\varphi_1 \quad \varphi_2 \quad \ldots \quad \varphi_N]$
- The M-dimension compressed measurement signal, $\mathbf{y}$
- The sparsity level of the sparse signal, k

Output:

- The reconstructed signal, **s**

Procedure:

a) Set **s**(0) to zero vector and t to 0.

b) At each iteration, **s**(t+1) was computed by

$$\mathbf{s}(t+1) = \mathbf{H}_k\,(\mathbf{s}(t) + \mu\mathbf{g}(t)),$$

where $\mathbf{H}_k(\mathbf{a})$ is the non-linear operator where the k largest components in **a** are kept but the remaining components are set to zero. μ is the step size. In this dissertation, **g** is defined as follows.

$$\mathbf{g}(t) = \mathbf{\Phi}^T \mathbf{W}_t(\mathbf{y} - \mathbf{\Phi}\mathbf{s}(t))$$

$\mathbf{W}_t$ is an $M \times N$ diagonal matrix. The diagonal element in $\mathbf{W}_t$ is defined as

$$\mathbf{W}_t(i,i) = \frac{\alpha^2}{\alpha^2 + (y_i - \mathbf{\Phi}_i^T s(t))^2}, i = 1, ..., M.$$

The step size is set as

$$\mu(t) = \frac{\left\|\mathbf{g}_{k(t)}(t)\right\|_2^2}{\left\|\mathbf{W}_t^{1/2}\mathbf{\Phi}_{k(t)}\mathbf{g}_{k(t)}(t)\right\|_2^2}.$$

In case that $\left\|\mathbf{y} - \mathbf{\Phi}\mathbf{s}(t+1)\right\|_{LL_2,\alpha} > \left\|\mathbf{y} - \mathbf{\Phi}\mathbf{s}(t)\right\|_{LL_2,\alpha}$, $\mu(t)$ is set to $0.5\mu(t)$.

c) Terminate when the difference between $\mathbf{\Phi}\mathbf{s}$ and **y** is less than or equal to the predefined error.

LIHT is the fast and robust algorithm but it faces the same problem as IHT. It requires that either **s** must be very sparse or **y** must be very large (high measurement rate). It is faster than OMP but has less stability.

2.2.5 Distributed Compressed Sensing Simultaneous Orthogonal Matching Pursuit (DCS-SOMP)

Distributed Compressed Sensing (DCS) uses the concept of joint sparsity, which is the sparsity of every signal in the ensemble [27][29]. It is used under the environment that there are a number of **y** whose original signals (**s**) are related. The reconstructed sparse signals of these **y**'s share some information (common components) even though they are not the same. The unique information of each **y** is defined as innovation. There are 3 models in DCS.

(1) sparse common component + innovations: both the common information (component) and the unique information (innovation) in **y** are sparse.
(2) common sparse support: every **y** is constructed from the sparse signal whose non-zero elements locate at the same position. The non-zero amplitude may be different.
(3) non-sparse common component + sparse innovations: the common component in **y** is non-sparse signal, but the innovation is sparse.

In this dissertation, the common sparse support model is used. As there is only one **y**, there is no innovation in the ensemble of the sampled **y**. Simultaneous OMP (SOMP) [27][32] is proposed as the reconstruction algorithm. SOMP is adapted from OMP.

DCS-SOMP searches for the solution that contains maximum energy in the signal ensemble. Given that the ensemble of **y** is $\{\mathbf{y}_i\}$; $i = 1,2,...,L$. The basis selection criterion in DCS-SOMP is changed from $\lambda_t = \arg \max_{j=[1,N], j\notin\Lambda_{t-1}} \left\langle \mathbf{r}_{t-1}, \varphi_j \right\rangle$ to $\lambda_t = \arg \max_{j=[1,N], j\notin\Lambda_{t-1}} \sum_{i=1}^{L} \left| \left\langle \mathbf{r}_{i,t-1}, \varphi_{i,j} \right\rangle \right|$, where $\mathrm{r}_{i,t\text{-}1}$ is the residual of $\mathbf{y}_i$ to the projection of $\mathbf{y}_i$ on to the space spanned by $\mathbf{\Phi}_{t\text{-}1}$. The rest of the procedure remains the same as OMP. The indexes of non-zero components in the reconstructed $\mathbf{s}_i$ (i = 1, 2, ..., L) are the same, but the value of non-zero components may differ. It should be noted that when L is equal to one, the DCS-SOMP is OMP.

CHAPTER III

PROPOSED METHODS

This chapter addresses the problems of reconstructing from a compressed measurement signal (**y**) in three noise environments: (1) Gaussian noise (2) impulsive noise and (3) Gaussian and impulsive noise. The block processing is applied to reduce the computational cost. The block processing and the vectorization of the wavelet coefficients are described in Section 3.1. The proposed reconstruction process in Gaussian noise environment is explained in Section 3.2. The proposed impulsive noise rejection method is described in Section 3.3. The reconstruction in both Gaussian and impulsive noises environment is presented in Section 3.4.

3.1 Block processing and the vectorization of the wavelet coefficients

In this dissertation, the Discrete Wavelet Transform (DWT) is used to obtain the sparsified version of an image. Figure 3.1 shows an example of block processing and the vectorization of the wavelet coefficients. Figure 3.1(a) shows the structure of a wavelet transformed image. The LL_3 subband is presented in red. Other subbands (LH, HL, and HH) in the third, the second and the first levels are presented in green, orange, and blue, respectively. The LL_3 subband is the most important subband, because it contains most of the energy in the image. Figure 3.1(b) shows the re-ordering of the wavelet coefficients. The coefficients are ordered such that the LL_3 subband is located at the beginning of each row. The LL_3 subband is followed by the other subbands in the third, the second, and the first levels.

The wavelet-domain image in Figure 3.1(b) is divided into blocks along its rows as shown in Figure 3.1(c). In Figure 3.1(c), the image has 8 rows; consequently, it is divided into 8 blocks. Each row in Figure 3.1(c) is considered as a sparse signal in this dissertation.

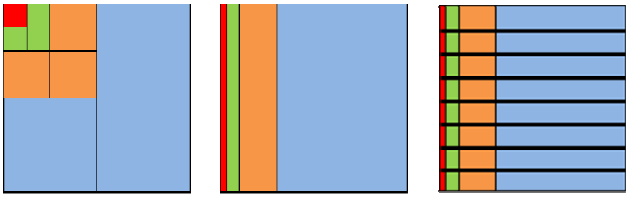

(a) (b) (c)

Figure 3.1: The illustration of block processing and vectorization in Section 3.1; (a) wavelet transformed image, (b) wavelet subbands vectorization and reorganization, and (c) wavelet blocks.

The signal can be made more sparse by the wavelet shrinkage thresholding [34]. In the wavelet shrinkage thresholding, all coefficients in the LL_3 subband are preserved, while coefficients outside the LL_3 subband with magnitude less than the wavelet shrinkage threshold are set to zero. Note that not all coefficients outside the LL_3 subband are set to zero. Since only the small coefficients in high frequency subband are set to zero, most distinct edges in the image are preserved. The sparsifying transformation by the wavelet shrinkage thresholding has little distinct visual degradation if the wavelet shrinkage threshold is selected properly. Figure 3.2 shows one example of an image before and after wavelet shrinkage thresholding.

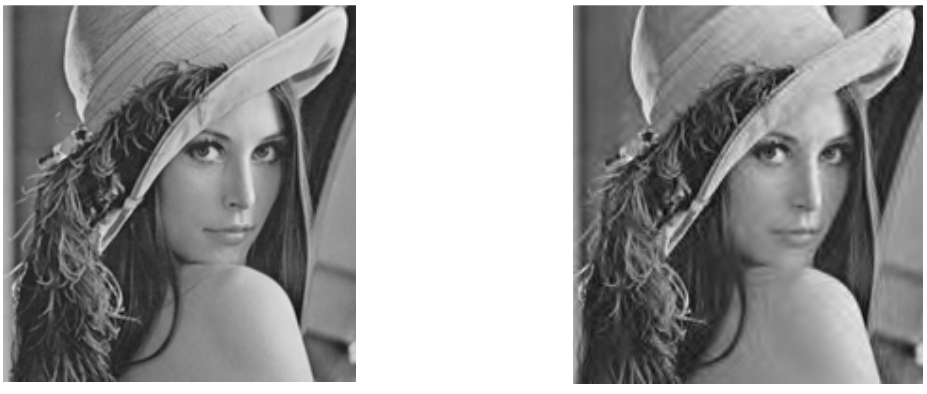

(a) (b)

Figure 3.2: The part of Lena before and after wavelet shrinkage thresholding; (a) original Lena and (b) Lena which has 90% of its wavelet coefficients set to zero by wavelet shrinkage thresholding (threshold = 23.4). The mother wavelet is db8.

(a) Lena

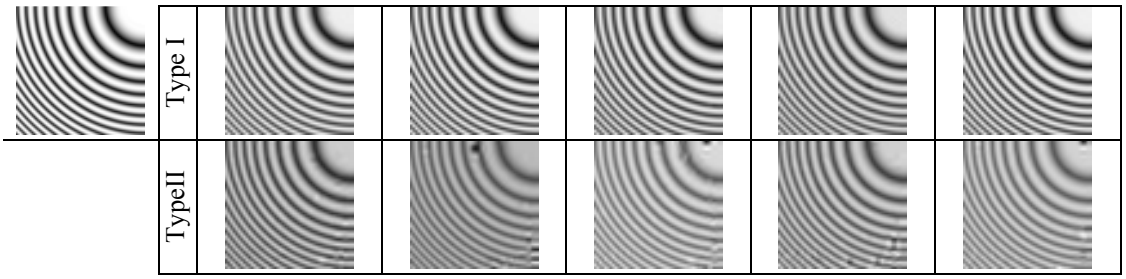

(b) Artificial image

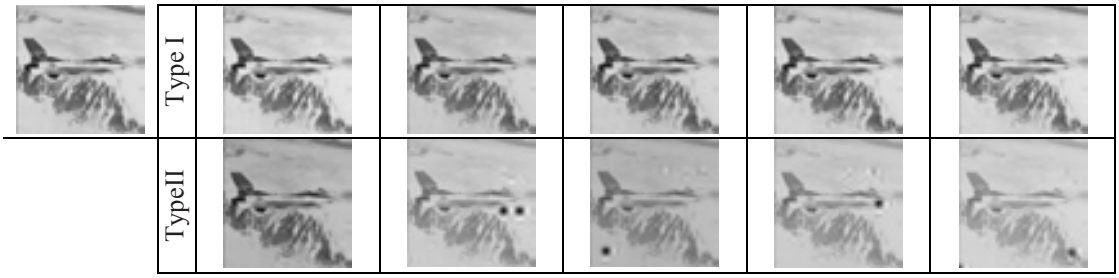

(c) Airplane (F-16)

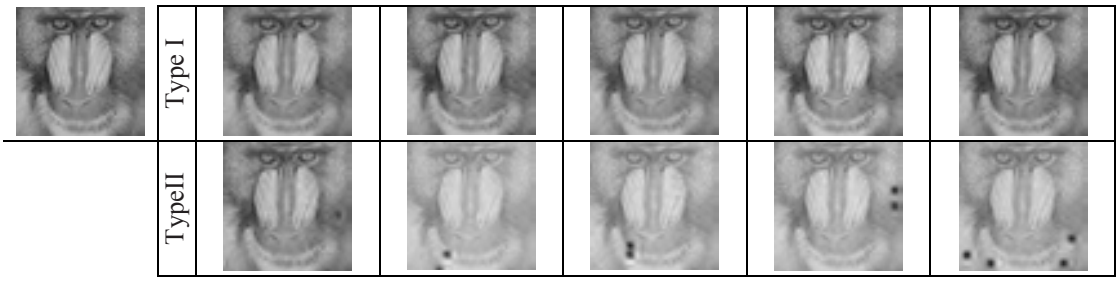

(d) Mandrill

Figure 3.3: The reconstruction examples for different vectorization of the wavelet blocks. Type I and Type II indicate the vectorization according to the structure in Figure 3.1(c) and the vectorization by the lexicographic order of Figure 3.1(a), respectively. (a) Lena, (b) Artificial image, (c) Airplane (F-16), and (d) Mandrill.

In the experiments, it is found that the vectorization according to the structure of Figure 3.1(c) is better than the one by the lexicographic order of Figure 3.1(a). Figure 3.3 shows some reconstruction examples when these two vectorization methods were used. The sparsity rate (k/N) and the measurement rate (M/N) were set to 0.1 and 0.3, respectively. All images were reconstructed by OMP-PKS. The top row of each image shows the reconstruction when the vectorization in each block was done such that it had the structure as shown in Figure 3.1(c). The bottom row of each image shows the reconstruction when the vectorization in each block was done by the lexicographic order of the structure shown in Figure 3.1(a). There was no fail reconstruction (dark spot) in the top row; whereas, there were some in the bottom row.

3.2 Reconstruction in Gaussian noise environment

The reconstruction method is divided into three stages: the construction of the ensemble of $\mathbf{y}$, the reconstruction by OMP-PKS [30], and data merging.

3.2.1 Construction of the ensemble of y

Given that there are L different pM-dimension signals in the ensemble of $\mathbf{y}$. p is the ratio of the sampled signal's size to the original size and $0 < p \leq 1$. p and L are predefined. The i-th signal in the ensemble is denoted by $\mathbf{y}_i$. The algorithm for constructing $\mathbf{y}_i$ is as follows.

Input:

- An $M \times N$ measurement matrix, $\mathbf{\Phi}$
- The M-dimensional compressed measurement signal, $\mathbf{y}$
- The dimension of $\mathbf{y}_i$, $\beta = pM$

Output:

- The i-th signal in the ensemble, $\mathbf{y}_i$
- The truncated measurement matrix for $\mathbf{y}_i$, $\mathbf{\Phi}_i$

Procedure:

a) Create the set of β random integers, $R = \{r_1, r_2,...,r_\beta\}$, having the following properties.

b) For all $j, l \in [1, \beta]$, $r_j \in [1, M]$ and $r_j = r_l$ only if $j = l$.

c) Construct $\mathbf{y}_i$ by setting the j-th component of $\mathbf{y}_i$ to the r_j-th component of $\mathbf{y}$ for all $j \in [1, \beta]$.

d) Construct $\mathbf{\Phi}_i$, according to the following function.
For all $j \in [1, \beta]$, set the jth row of $\mathbf{\Phi}_i$ to the r_j-th row of $\mathbf{\Phi}$.

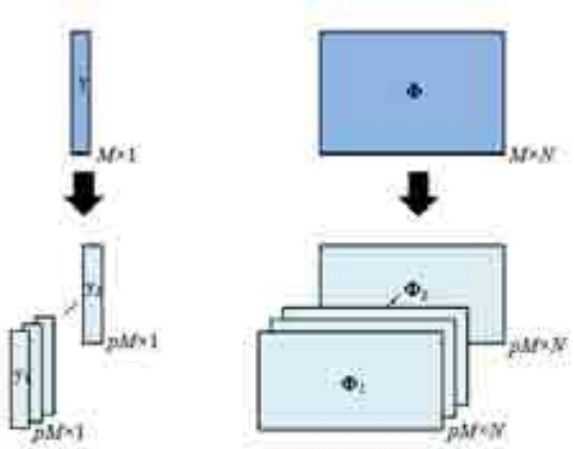

Figure 3.4: The ensemble of compressed measurement vector and measurement matrix.

Figure 3.4 shows the result of applying the above procedure for L times to create the ensemble of L sampled signals. The total dimension of the ensemble is $pM \times 1 \times L$. The ensemble is accompanied by L truncated measurement matrices. The size of the truncated matrix is $pM \times N$. Since all $\mathbf{y}_i$'s are the parts of the same $\mathbf{y}$, their information is the same and they contain Gaussian noise of the same mean and the same variance. As long as the reconstruction does not use all signals in the ensemble

at once, it is safe to assume that reconstruction results from different $\mathbf{y}_i$ contain different noise.

3.2.2 Reconstruction by OMP-PKS

The reconstruction of the proposed algorithm has the following requirements:

(1) The reconstruction of the signal at low measurement rate (M/N),
(2) fast reconstruction,
(3) independent reconstruction result for each signal in the ensemble.

The first requirement comes from the fact that the reconstruction is performed on the sampled signal which is smaller than $\mathbf{y}$. The RIP in (2.4) is not always guaranteed. The second requirement is necessary because the reconstruction must be performed L times (L is the number of the signal in the ensemble). The third requirement is the result of taking the information from only one signal. By combining every sampled signal, original noisy $\mathbf{y}$ will be acquired. In the proposed algorithm, the denoising by averaging is possible when each $\mathbf{y}_i$ has the distinct reconstruction result from one another. Since each $\mathbf{y}_i$ carries different set of the $\mathbf{y}$'s components, its total noise is different. Consequently, the reconstruction on each $\mathbf{y}_i$ gives the result having different noise corrupted to each pixel. The noise in each pixel can be reduced by averaging.

Even though the reconstruction is performed on the ensemble of $\mathbf{y}$ as DCS, DCS-SOMP is not applicable, since it does not meet the third requirement. Any greedy algorithms applied to each $\mathbf{y}_i$ meet the second and the third requirements. The measurement rate can be kept low (the first requirement) by including the model into the reconstruction. OMP-PKS [30] is chosen in this algorithm, because its requirement for measurement rate is low. The experiment in [30] shows that the requirement of OMP-PKS was lower than CoSaMP-PKS.

OMP-PKS is applied to every $\mathbf{y}_i$ in the ensemble and forms L different sparse signals (wavelet coefficient). At the end of this stage, there are L noisy images.

3.2.3 Data merging

L noisy cropped images at the end of the reconstruction process have noise that is similar to Gaussian noise (Figure 3.5). At the same position, the noise in different reconstructed images had distinctly different magnitude; consequently, it can be reduced by taking the average at each pixel in spatial domain. Because the average is not done in spatial domain, therefore the loss in spatial resolution is low. The denoising in spatial domain can be done by using the conventional denoising algorithms such as the Gaussian smoothing model [36], the Yaroslavsky neighborhood filters and an elegant variant [37]-[38], the translation invariant wavelet thresholding [39], and the discrete universal denoiser [40].

(a) Airplane (F-16)

(b) Mandrill

Figure 3.5: The reconstruction examples of $\mathbf{y}_i$.

3.3 Reconstruction in impulsive noise environment

The proposed noise rejection method is applied before the reconstruction and divided into two stages. In the first stage, the algorithm to detect impulsive noise is applied. Then OMP-PKS is also applied to estimate the information that is lost due to

the impulsive noise. The algorithm to detect the impulsive noise and the estimation of the missing information are described in Subsections 3.3.1 and 3.3.2, respectively.

3.3.1 The detection of the impulsive noise

Figures 3.6 and 3.7 show the examples of the reconstruction from $\mathbf{y}$ corrupted by impulsive noise. In these two figures, Figures (a), (b) and (c) show the original blue $\mathbf{y}$ corrupted by the red impulsive noise, the original $\mathbf{s}$ and the reconstructed $\hat{\mathbf{s}}$ from Figure (a), respectively. The figures clearly indicate that the energy distribution was different. The energy of the signals in Figures 3.6(c) and 3.7(c) was spread out, while most energy of the signals in Figures 3.6(b) and 3.7(b) was contained in the third-level subbands.

Even though there is no definite structure of $\mathbf{y}$, Figures 3.6 and 3.7 indicate that the energy distribution of $\mathbf{s}$ can be exploited to detect the existence of impulsive noise. The large impulsive noise leads to a bad approximation of $\hat{\mathbf{s}}$ whose energy leaks out of the third level subband. The ratio of the energy outside the third level subband to the total energy is used to determine the existence of the impulsive noise in $\mathbf{y}$. The high ratio indicates that the energy is spread out; thus, the existence of the impulsive noise. The impulsive noise has very large magnitude in comparison to $\mathbf{y}$. Consequently, if the impulsive noise exists, it has the largest magnitude. The removal of the impulsive noise is simply the removal of the elements with the largest magnitude. The size of the impulsive noise may vary, so the removal is performed iteratively until either of the following two stopping criteria is satisfied.

(1) The reconstructed $\hat{\mathbf{s}}$ has most of its energy inside the third level subband.
(2) The reconstruction is unlikely to be successful because too many elements in $\mathbf{y}$ have been removed.

According to the stopping criteria, there are two thresholds that need to be defined. The threshold in the first criterion is used to indicate the amount of the energy that is allowed to be leaked out of the third level subband. The amount of the energy is measured as the ratio to the total energy. The threshold is defined as the

(leakage) energy-ratio threshold, η. The threshold in the second criterion is required to ensure that there is sufficient information left for the reconstruction. This threshold is called rejection-ratio threshold, *T*, which is defined as the ratio between the numbers of the removed elements to the size of **y** (*M*). Thus, the maximum number of the elements that can be removed is *TM*. The optimum values of η and *T* are investigated in Chapter 4.

At each iteration, the noise corrupted elements are removed from **y** and the size of the available measurement signal becomes smaller. Hence, it is required that the reconstruction algorithm is still effective at low measurement rate. OMP-PKS is adopted by including the algorithm for the detection and the removal of impulsive noise as follows.

Input:

- An $M \times N$ measurement matrix, $\mathbf{\Phi}$
- The *M*-dimensional compressed measurement signal, **y**
- The sparsity level of the sparse signal, *k*
- The number of wavelet coefficients in the third level subband, l_3
- The (leakage) energy-ratio threshold, η
- The rejection-ratio threshold, *T*

Output:

- The number of impulsive noise corrupted elements, n_δ
- The set containing the n_δ indexes of the impulsive noise corrupted elements, $\varsigma_\delta = \{\varpi_1, \varpi_2, ..., \varpi_{n_\delta}\}$

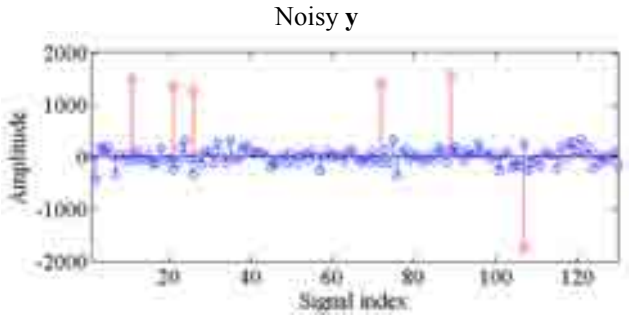

(a)

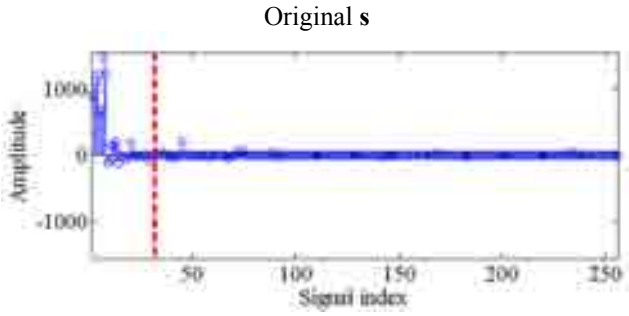

(b)

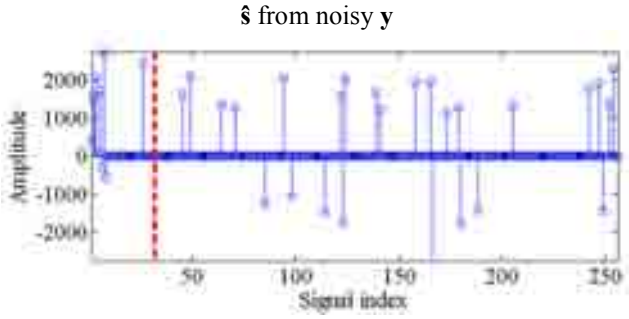

(c)

Figure 3.6: The first reconstruction example when **y** was corrupted by impulsive noise. (a) The 128-D **y** corrupted by 6 impulsive noise, (b) the original 256-D **s** (k = 25) and (c) the signal reconstructed from (a) by OMP-PKS. In (b) and (c), the area to the left of the red dashed line belongs to the third level subband; the area to the right belongs to the first and the second level subbands.

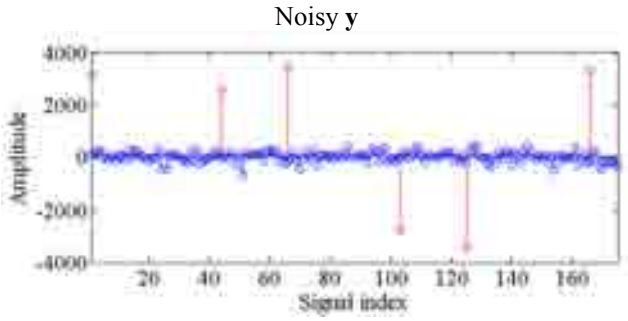

(a)

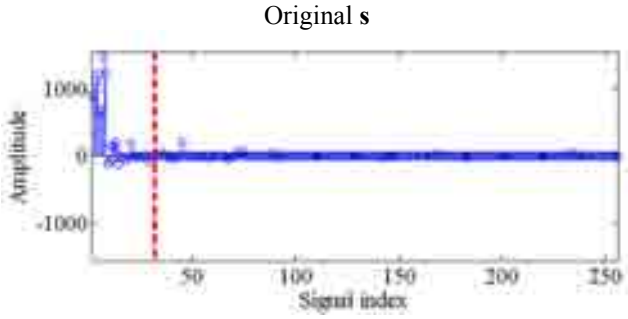

(b)

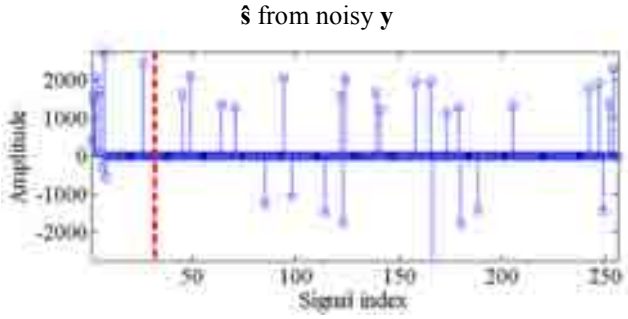

(c)

Figure 3.7: The second reconstruction example when **y** was corrupted by impulsive noise. (a) The 128-D **y** corrupted by 6 impulsive noise, (b) the original 256-D **s** (k = 25) and (c) the signal reconstructed from (a) by OMP-PKS. In (b) and (c), the area to the left of the red dashed line belongs to the third level subband; the area to the right belongs to the first and the second level subbands.

Procedure:

a) Initialize $t = 0, n_\delta = 0, \varsigma_\delta = \varnothing, \mathbf{y}_t = \mathbf{y}, \mathbf{\Phi}_t = \mathbf{\Phi}$.

b) Apply OMP-PKS to reconstruct $\hat{\mathbf{s}}$ from $\mathbf{y}_t$ and $\mathbf{\Phi}_t$.

c) Calculate the (leakage) energy-ratio (ER).

$$\mathrm{ER} = \frac{\sum_{i=l_3+1}^{N} \hat{s}_i^{\,2}}{\sum_{j=1}^{N} \hat{s}_j^{\,2}},$$

where $\hat{s}_i$ and l_3 are the i-th element of $\hat{\mathbf{s}}$ and the number of wavelet coefficients in the third level subband.

d) Terminate if ER < η.

e) Assign the elements in $\mathbf{y}_t$ having the maximum magnitude as the impulsive noise. α_m ($m = 1, 2, \ldots, n_{\delta_t}; n_{\delta_t}$ is the number of the elements having the maximum magnitude in $\mathbf{y}_t$.) are defined as the indexes of the recently assigned impulsive noise elements. Note that α_m are the indexes of $\mathbf{y}$. In case that there are more than one element having the maximum magnitude ($n_{\delta_t} > 1$), all of them are to be removed in Step i)

f) Increment n_δ by n_{δ_t} and add α_m to ς_δ.

g) Terminate if $n_\delta \geq TM$.

h) Set $t = t + 1$.

i) $\mathbf{y}_t$ is assigned the value of $\mathbf{y}$ after the noise elements (the elements with the indexes in ς_δ) are removed from $\mathbf{y}$. $\mathbf{\Phi}_t$ is assigned the value of $\mathbf{\Phi}$ after the rows corresponding to the noise elements are removed from $\mathbf{\Phi}$.

j) Go to step b).

If the algorithm is terminated in step g), the removal of impulsive noise is unsuccessful. Too many elements have been removed and it is unlikely that there is sufficient information to reconstruct $\hat{\mathbf{s}}$ and estimate the missing information in the next stage.

It should be noted that the proposed algorithm is applicable to images because image data have some degree of redundancy. The rejection-ratio threshold, *T*, can be set quite large. For the signal data that has low degree of redundancy, the value of *T* has to be very small. In this case, the reconstruction is unlikely to succeed if every information in **y** is not used.

3.3.2 Estimation of the missing information

The outputs (n_δ and ς_δ) from the detection stage and **y** are used as the inputs of this stage. The noise corrupted elements, specified in ς_δ, are removed. After the noise removal, the size of the compressed measurement signal **y** is smaller than the size of the original **y**; consequently, the reconstruction methods requiring high measurement rate may fail to reconstruct $\hat{\mathbf{s}}$. It is necessary to estimate the values of the removed elements to preserve the measurement rate. In the proposed method, the values are estimated such that they comply with other noiseless elements. The estimation algorithm is as follows.

Input:

- The *M*-dimension compressed measurement signal, **y**
- The number of impulsive noise corrupted elements, n_δ
- The set containing the n_δ indexes of the impulsive noise corrupted elements, $\varsigma_\delta = \{\varpi_1,\ \varpi_2,\ ...,\ \varpi_{n_\delta}\}$

Output :

The estimated noise-free **y**, $\hat{\mathbf{y}}$

Procedure:

a) Define $\mathbf{y_s}$ as **y** with its ϖ_i-th $(i = 1, 2, ..., n_\delta)$ elements removed. Define $\mathbf{\Phi_s}$ as $\mathbf{\Phi}$ with its ϖ_i-th $(i = 1, 2, ..., n_\delta)$ rows removed.

b) Apply OMP-PKS to reconstruct $\hat{\mathbf{s}}_s$ from $\mathbf{y_s}$ and $\mathbf{\Phi_s}$.

c) Define $\tilde{\mathbf{y}} = \mathbf{\Phi}\hat{\mathbf{s}}_s$ and estimate the *i*-th elements in $\hat{\mathbf{y}}$ as follows.

$$\hat{y}_i = \begin{cases} y_i & ;i \notin \varsigma_\delta \\ \tilde{y}_i & ;i \in \varsigma_\delta \end{cases},$$

where the subscript *i* indicates the *i*-th elements of the signal and $i = 1, 2, ..., M$.

After this process, the impulsive noise corrupted elements in **y** are replaced by values complying with noise-free elements. Conventional CS reconstruction methods can be applied to reconstruct $\hat{\mathbf{s}}$ from the impulsive noise free $\hat{\mathbf{y}}$.

3.4 Reconstruction in both Gaussian and impulsive noises environment

It is possible that more than one kind of noise exist in the system. Figures 3.8 and 3.9 show the examples of the reconstruction signal from **y** corrupted by the Gaussian and impulsive noise. Figures 3.8(a) and 3.9(a) show the blue **y** corrupted by the red Gaussian noise and impulsive noise. Figures 3.8 (b), (c), and (d) and 3.9(b), (c), and (d) show the original **s**, the reconstructed $\hat{\mathbf{s}}$ from the noisy **y**, and $\hat{\mathbf{s}}$ from the noisy **y** without impulsive noise corrupted elements, respectively. In Figures 3.8(b), (c), and (d) and 3.9(b), (c), and (d), the area to the left of the red dash line belongs to the third level subband; the area to the right belongs to the first and the second level subbands. The figures clearly indicate that the energy distribution were different. Most energy in Figures 3.8(b), (d) and 3.9(b), (d) located in the third-level subbands. While the energy in Figures 3.8(c) and 3.9(c) were spread out from the effect of the impulsive noise.

The characteristic of energy distribution of $\hat{\mathbf{s}}$ from Gaussian noise corrupted **y** is similar to the characteristic of energy distribution $\hat{\mathbf{s}}$ from noise-free **y**. Thus, the impulsive noise rejection method in Section 3.3 can be applied to estimate impulsive noise free of **y**. However, the reconstructed signal is not exactly the same as the original **s**, because of the Gaussian noise in $\hat{\mathbf{s}}$ (Figures 3.8(d) and 3.9(d)). The effect of Gaussian noise can be removed by using the method in Section 3.2.

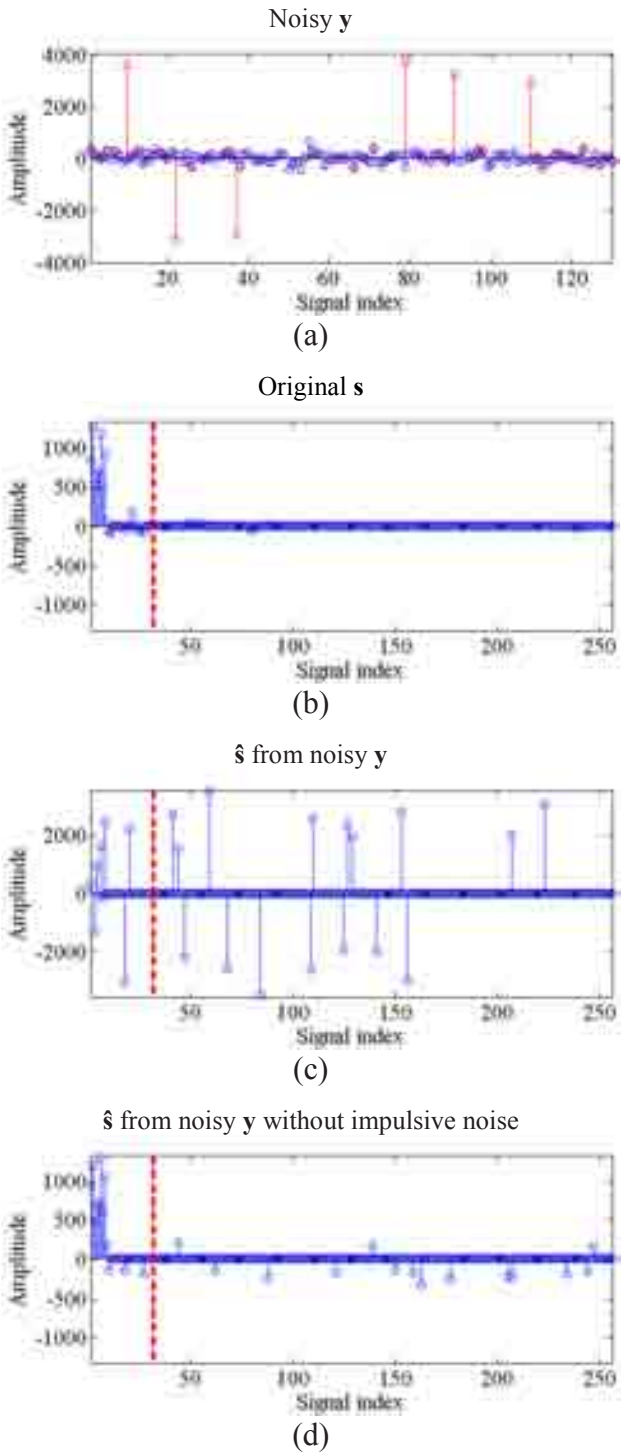

Figure 3.8: The first reconstruction example when **y** was corrupted by Gaussian and impulsive noises. (a) The 128-D **y** corrupted by 6 impulsive noise and Gaussian noise with 10 dB SNR. (b) The original 256-D **s** (k = 25). (c) The signal reconstructed from the noisy **y** in (a). (d) The signal reconstructed from **y** without the impulsive noise corrupted elements.

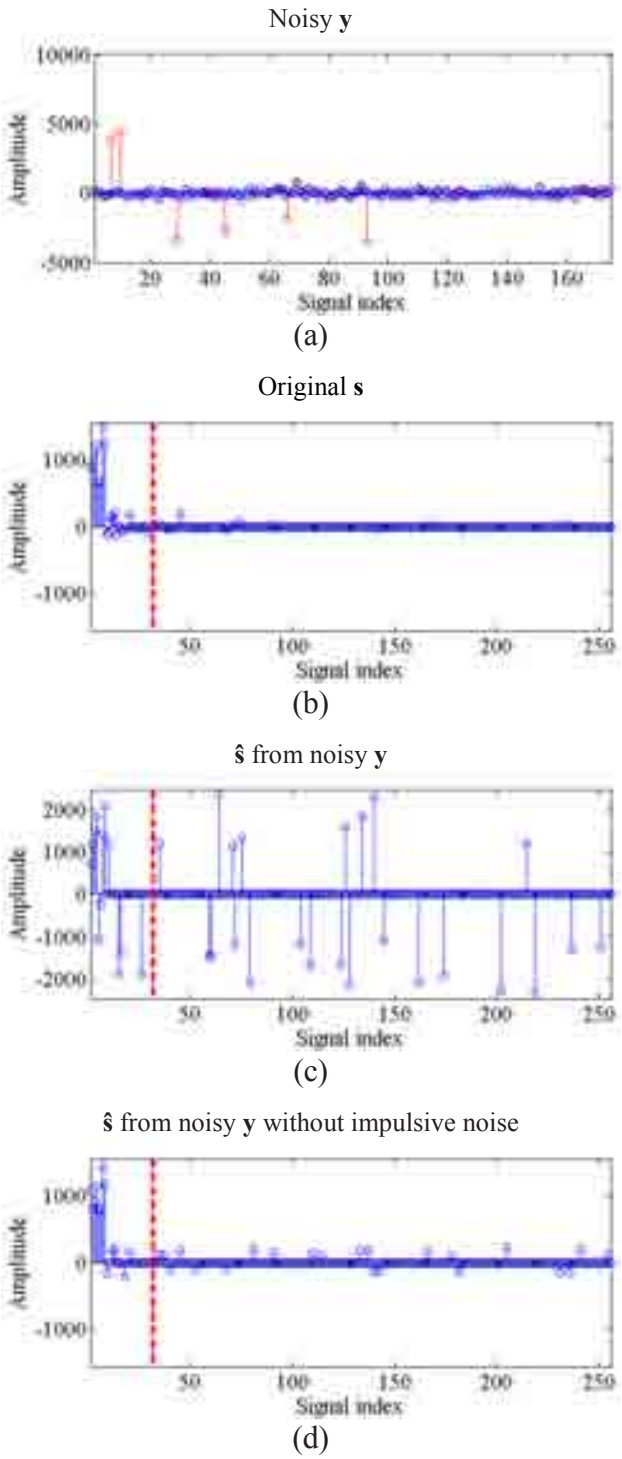

Figure 3.9: The second reconstruction example when **y** was corrupted by Gaussian and impulsive noises. (a) The 128-D **y** corrupted by 6 impulsive noise and Gaussian noise with 10 dB SNR. (b) The original 256-D **s** ($k = 25$). (c) The signal reconstructed from the noisy **y** in (a). (d) The signal reconstructed from **y** without the impulsive noise corrupted elements.

CHAPTER IV
EXPERIMENT AND DISCUSSION

4.1 Experiment setup

The experiment was conducted on a PC with 2.83GHz Intel Core 2 Quad CPU and 4 GB of RAM. All methods were implemented by 64-bit MATLAB R2011a. The proposed methods were tested on 40 images. All test images were resized to 256×256. Figure 4.1 shows the test images. Images in the first row and the second row are the standard test images. The remaining images in the third row, the fourth row and the first two images in the fifth row are the artificial images. The remaining images are the natural images. (The artificial and natural images are available at http://sourceforge.net/projects/testimages/files/.)

Octave-tree DWT was used to transform test images to sparse domain. The mother wavelet was Daubechies 8 (db8). The wavelet shrinkage thresholding [33] was applied to make the signal sparser. The measurement matrix was based on Hadamard matrix. Each wavelet image was divided into the block of 1×256. The number of blocks was 256. The average sparsity rate (k/N) of blocks in an image was 0.1. The average measurement rates used in the experiment were 0.2, 0.3, 0.4, 0.5 and 0.6. Peak signal-to-noise ratio (PSNR) and visual inspection were used for performance evaluation. All PSNRs shown in the graph were average PSNRs.

4.2 Experiment on Gaussian noise environment

OMP-PKS+Resampling (OMP-PKS+ReS) and OMP-PKS+Random Subsampling (OMP-PKS+RS) were compared with BPDN, LIHT, OMP-PKS, DCS-SOMP+ReS, and DCS-SOMP+RS. Since the compression step in CS consists mostly of linear operations, Gaussian noise corrupting the signal in the earlier states is approximated as the Gaussian noise corrupting the compressed measurement vector.

Figure 4.1: The test images

The state where the noise corrupted the image was not specified; therefore, in this study, the compressed measurement **y** was simply corrupted by Gaussian noise. The level of Gaussian noise was varied according to its variance.

The experiment consisted of three parts: (1) the evaluation for the size of an ensemble (L) and the size of a signal in the ensemble (p) for OMP-PKS+RS and DCS-SOMP+RS in Section 4.2.1, (2) the evaluation for OMP-PKS+ReS and DCS-SOMP+ReS in Section 4.2.2, and (3) the performance evaluation in Section 4.2.3.

4.2.1 Evaluation for *L* and *p* for DCS-SOMP+RS and OMP-PKS+RS

Both OMP-PKS+RS and DCS-SOMP+RS require the ensemble of **y**. **y** was randomly subsampled with the algorithm described in Section 3.2.1 to create the ensemble. L and p for the optimum performance were investigated. p was measured in term of the ratio to the size of **y**. It should be noted that p is always less than 1.

Figures 4.2-4.5 show the PSNR of the reconstruction images at different L and p when the noise variance (σ^2) were 0.025, 0.05, 0.075, and 0.1, respectively. The figures clearly show that the best performance of OMP-PKS+RS was better than the one of DCS-SOMP+RS in all cases.

The line in the graph of Figures 4.2-4.5 was shown in different color to represent different p. The effect of p was more pronounced in OMP-PKS+RS than in DCS-SOMP+RS. The maximum PSNR in OMP-PKS+RS was achieved when p = 0.9, 0.7, 0.6, and 0.6 when σ^2 was 0.025, 0.05, 0.075, and 0.1, respectively. When the noise was low, the reconstruction by OMP-PKS+RS at higher p provided the higher PSNR; whereas, when the noise was high, the reconstruction at lower p was better. At lower p, the information of the signal was lower leading to the higher reconstruction error. However, when the signal was noisy, more information at higher p led to the ensemble of more similar noisy signals and averaging had lower effect for Gaussian denoising. On the other hand, at lower p, signals were more different leading to the different reconstruction images, which could be considered as the images corrupted by Gaussian noise of the same variance. Consequently averaging

would lead to the noise reduction. The effect of the reconstruction error was more pronounced at low noise environment, while the effect of Gaussian noise was more pronounced at the high noise environment. The PSNRs of DCS-SOMP+RS were almost the same because all signals were combined in the reconstruction which led to the original signal.

The x-axis in Figures 4.2-4.5 represents L. When L was changed, the performance of DCS-SOMP+RS was almost unchanged. On the other hand, the performance of OMP-PKS+RS was better, when L was larger. When the noise was higher, OMP-PKS+RS required larger L to achieve the optimum performance. In order to achieve the best performance, OMP-PKS+RS required the larger L than DCS-SOMP+RS in all cases. In most cases, DCS-SOMP+RS and OMP-PKS+RS had already converged to their optimum performance at L = 6 and 16, respectively.

The optimum p and L at various M/N and various noise levels were summarized in Tables 4.1 and 4.2, respectively. In DCS-SOMP+RS, the optimum p varied from 0.6 to 0.9. Out of 20 cases shown in the table, the optimum p was 0.9 in 18 cases. Figures 4.2-4.5 indicated that p had little effect to the PSNR, so p for DCS-SOMP+RS was set to 0.9 in Section 4.2.2. In OMP-PKS+RS, the optimum p varied from 0.6 to 0.9, note that in most cases (11 out of 20 cases), the optimum p was 0.6. Even though p in OMP-PKS+RS had more effect to the result's PSNR than DCS-SOMP+RS, it was found that the PSNR difference between the best case and p = 0.6 was less than 1.2 dB. Hence, p for OMP-PKS+RS was set to 0.6 in Section 4.2.3.

From Table 4.2, the optimum L for DCS-SOMP+RS was always equal to 6; thus, L for DCS-SOMP+RS was set to 6 in Section 4.2.3. In OMP-PKS+RS, the optimum L varied from 16 to 26. Out of 20 cases shown in the table, the optimum L was 21 in 9 cases. The optimum L for OMP-PKS+RS was set to 21 in Section 4.2.3.

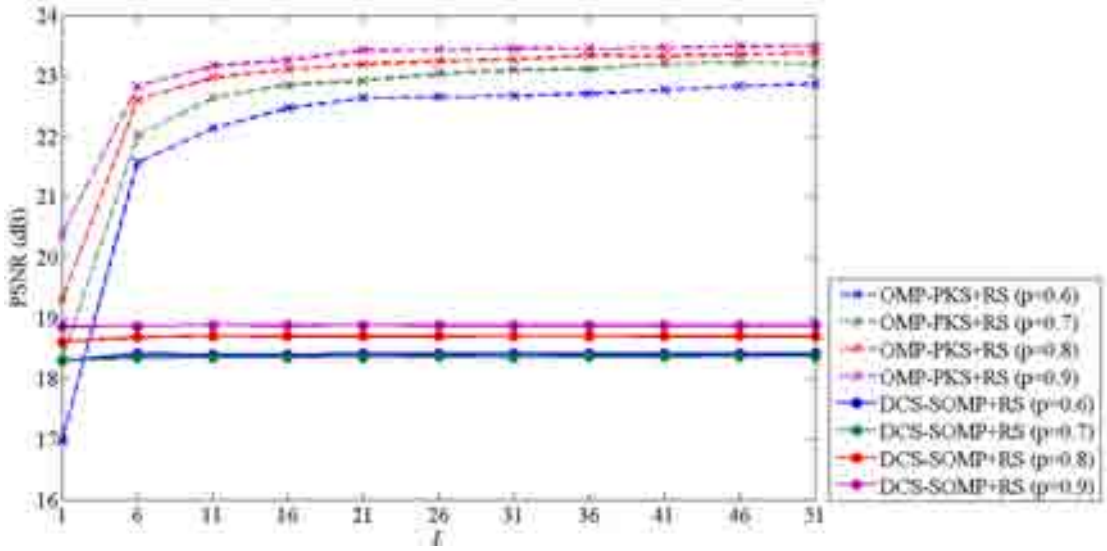

Figure 4.2: The average PSNR of reconstruction images by DCS-SOMP+RS and OMP-PKS+RS at $M/N = 0.3$ from $\mathbf{y}$ corrupted by Gaussian noise at $\sigma^2 = 0.025$.

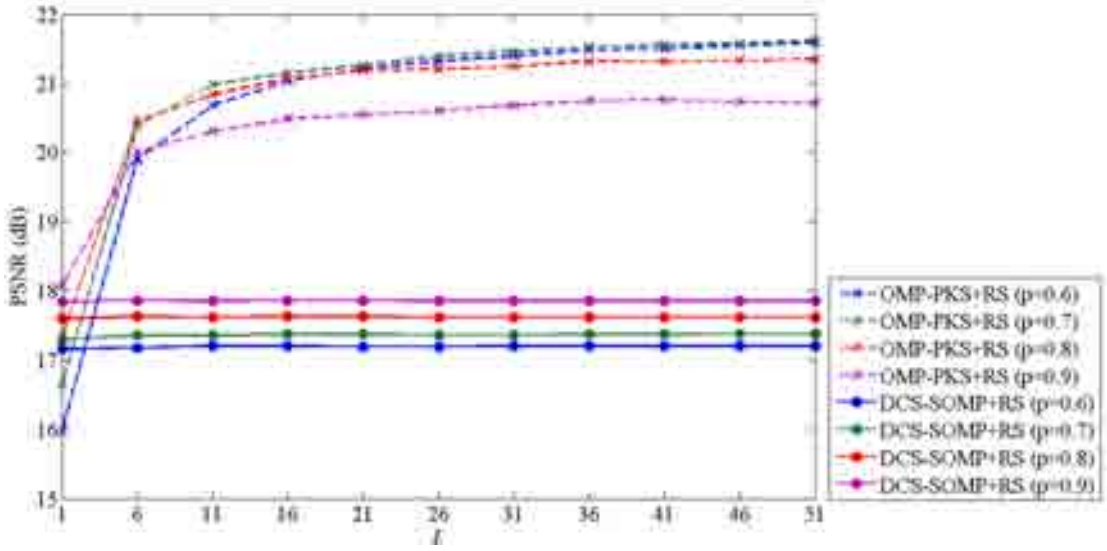

Figure 4.3: The average PSNR of reconstruction images by DCS-SOMP+RS and OMP-PKS+RS at $M/N = 0.3$ from $\mathbf{y}$ corrupted by Gaussian noise at $\sigma^2 = 0.05$.

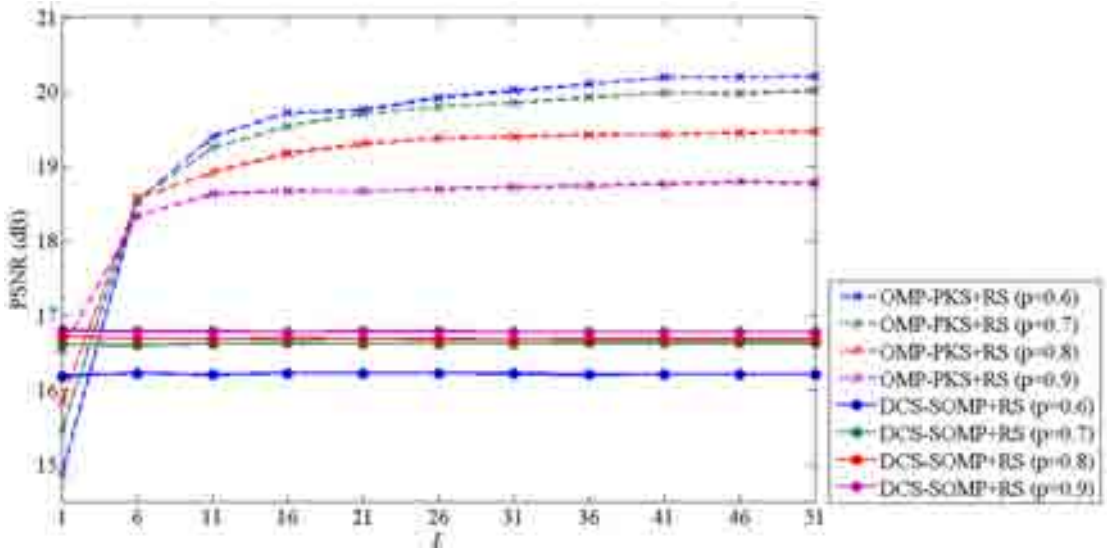

Figure 4.4: The average PSNR of reconstruction images by DCS-SOMP+RS and OMP-PKS+RS at $M/N = 0.3$ from $\mathbf{y}$ corrupted by Gaussian noise at $\sigma^2 = 0.075$.

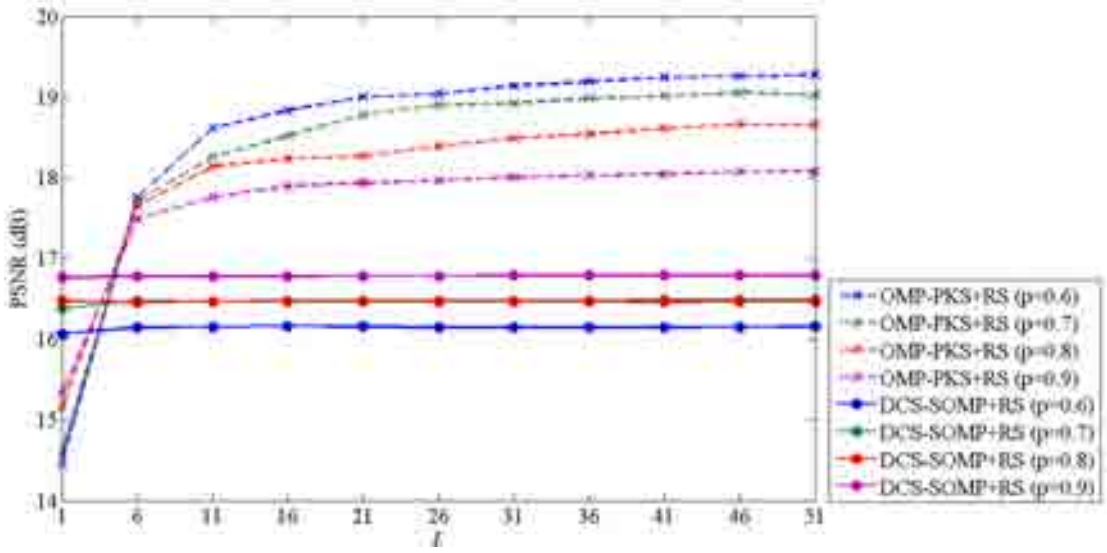

Figure 4.5: The average PSNR of reconstruction images by DCS-SOMP+RS and OMP-PKS+RS at $M/N = 0.3$ from $\mathbf{y}$ corrupted by Gaussian noise at $\sigma^2 = 0.1$.

Table 4.1: The number of p which provided the highest PSNR

	M/*N*									
	0.2		0.3		0.4		0.5		0.6	
σ^2	DCS-SOMP +RS	OMP-PKS +RS	DCS-SOMP +RS	OMP-PKS +RS	DCS-SOMP +RS	OMP-PKS +RS	DCS-SOMP +RS	OMP-PKS +RS	DCS-SOMP +RS	OMP-PKS +RS
0.025	0.9	0.8	0.9	0.9	0.9	0.9	0.9	0.9	0.9	0.9
0.05	0.9	0.8	0.9	0.7	0.9	0.8	0.9	0.6	0.9	0.7
0.075	0.6	0.6	0.9	0.6	0.9	0.6	0.9	0.6	0.9	0.6
0.1	0.8	0.6	0.9	0.6	0.9	0.6	0.9	0.6	0.9	0.6

Table 4.2: The number of L at which the converged PSNR was guaranteed and p were set according to Table 4.1.

	M/*N*									
	0.2		0.3		0.4		0.5		0.6	
σ^2	DCS-SOMP +RS	OMP-PKS +RS	DCS-SOMP +RS	OMP-PKS +RS	DCS-SOMP +RS	OMP-PKS +RS	DCS-SOMP +RS	OMP-PKS +RS	DCS-SOMP +RS	OMP-PKS +RS
0.025	6	16	6	16	6	21	6	21	6	21
0.05	6	16	6	21	6	26	6	21	6	26
0.075	6	26	6	16	6	21	6	31	6	26
0.1	6	21	6	16	6	21	6	21	6	26

4.2.2 Evaluation for *L* in DCS-SOMP+ReS and OMP-PKS+ReS

The size of the signal in the ensemble for OMP-PKS+ReS and DCS-SOMP+ReS was equal to the original size of y. Thus, only L was investigated for DCS-SOMP+ReS and OMP-PKS+ReS. $\mathbf{y}$ was resampled by the algorithm described in Section 3.2.1 to create the ensemble and p was set to 1.

Figures 4.6-4.10 show the average PSNR of the reconstruction images at different L and variances. The measurement rate (M/N) in Figures 4.6-4.10 was set to 0.2, 0.3, 0.4, 0.5, and 0.6, respectively. The solid line and the dashed line show the

PSNR of the reconstruction by DCS-SOMP+ReS and OMP-PKS+ReS, respectively. The figures clearly show that the best performance of OMP-PKS+ReS was better than the one of DCS-SOMP+ReS in all cases.

The line in the graph of Figures 4.6-4.10 was shown in different color to represent different level of Gaussian noise level (in term of variance (σ^2)). The maximum PSNRs in both OMP-PKS+ReS and DCS-SOMP+ReS were achieved at $\sigma^2 = 0.025$ (the lowest noise level). Moreover, when the measurement rate was increased, the PSNR improvement of OMP-PKS+ReS over DCS-SOMP+ReS decreased.

The *x*-axis in Figures 4.6-4.10 represents *L*. The performance of DCS-SOMP+ReS was almost unchanged when *L* was changed. While the performance of OMP-PKS+ReS was better, when *L* was larger. OMP-PKS+ReS required the same *L* to achieve the optimum performance at different noise levels. In order to achieve the best performance, OMP-PKS+ReS required the larger *L* than DCS-SOMP+ReS in all cases. In most cases, DCS-SOMP+ReS and OMP-PKS+ReS had already converged to their optimum performance at $L = 6$ and 21, respectively. Thus, in Section 4.2.3, *L* for DCS-SOMP+ReS and OMP-PKS+ReS was set to 6 and 21, respectively.

4.2.3 Performance evaluation

The performance of OMP-PKS+RS and OMP-PKS+ReS were compared to the ones of BPDN, LIHT, OMP-PKS, DCS-SOMP+RS and DCS-SOMP+ReS in this section. BPDN, LIHT, and OMP-PKS used the single $\mathbf{y}$ to reconstruct the result, while OMP-PKS+RS, OMP-PKS+ReS, DCS-SOMP+RS, and DCS-SOMP+ReS used the ensemble of $\mathbf{y}$. The error bound of BPDN was set to σ^2. The value of α in LIHT was set to the optimum value of 0.25 [24].

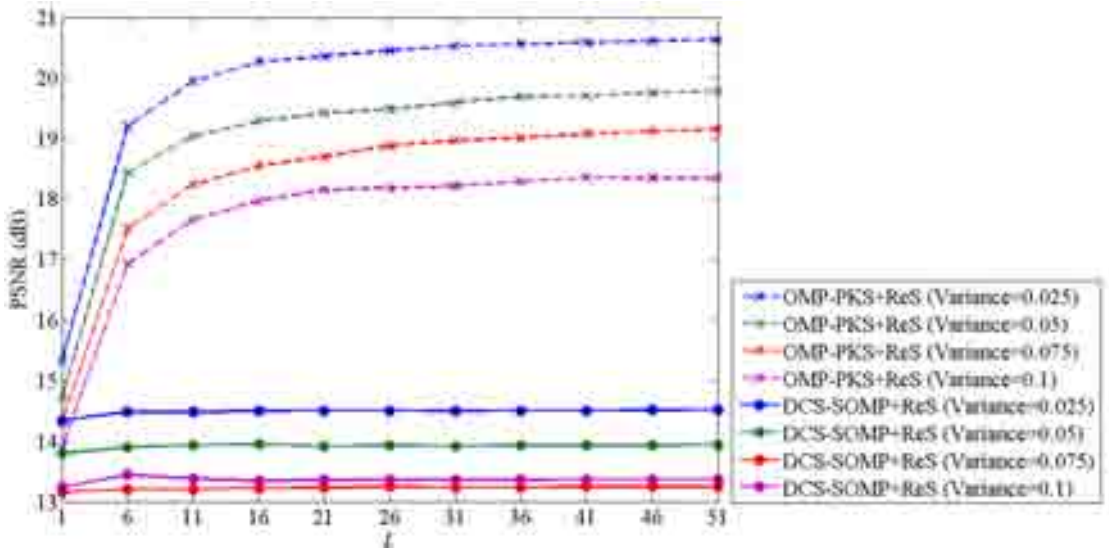

Figure 4.6: The average PSNR of reconstruction images by DCS-SOMP+ReS and OMP-PKS+ReS at M/N = 0.2 from **y** corrupted by different levels (variances) of Gaussian noise.

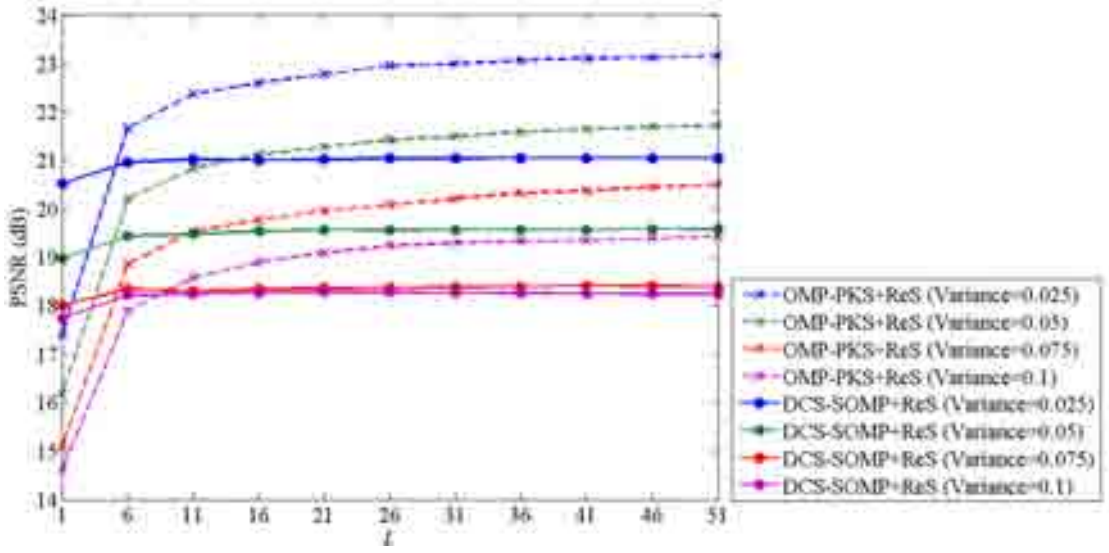

Figure 4.7: The average PSNR of reconstruction images by DCS-SOMP+ReS and OMP-PKS+ReS at M/N = 0.3 from **y** corrupted by different levels (variances) of Gaussian noise

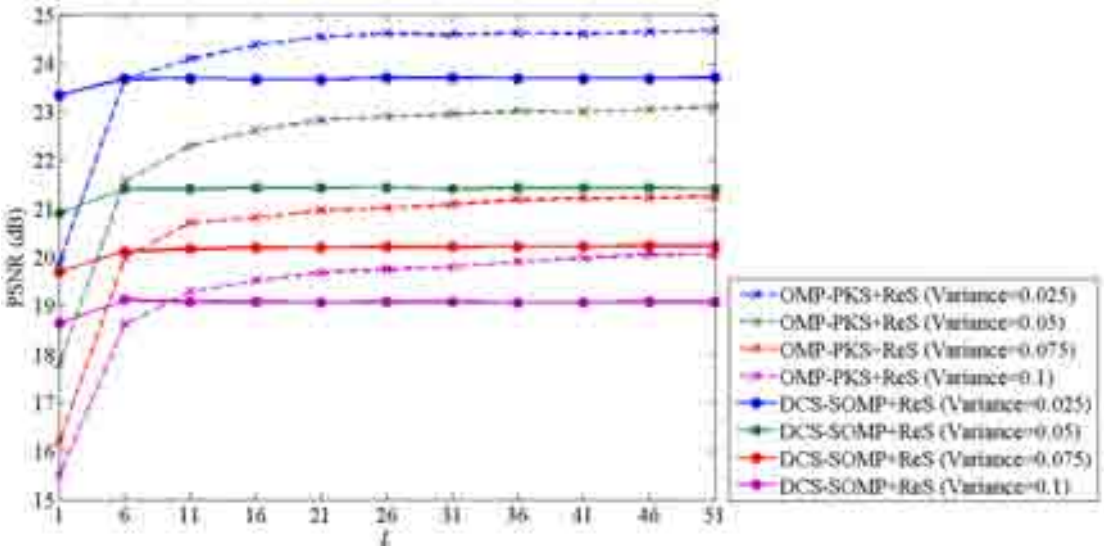

Figure 4.8: The average PSNR of reconstruction images by DCS-SOMP+ReS and OMP-PKS+ReS at M/N = 0.4 from **y** corrupted by different levels (variances) of Gaussian noise

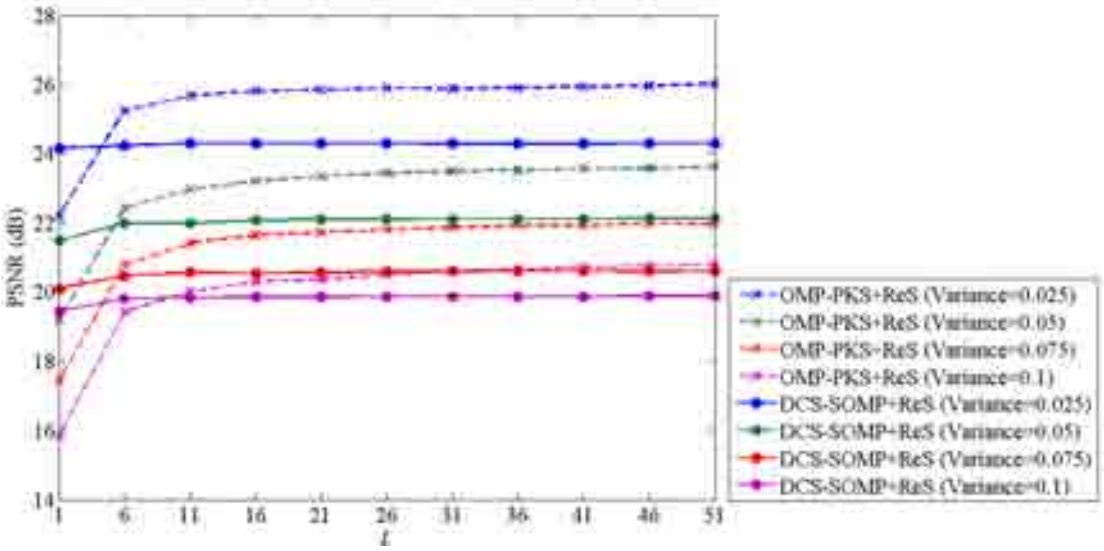

Figure 4.9: The average PSNR of reconstruction images by DCS-SOMP+ReS and OMP-PKS+ReS at M/N = 0.5 from y corrupted by different levels (variances) of Gaussian noise.

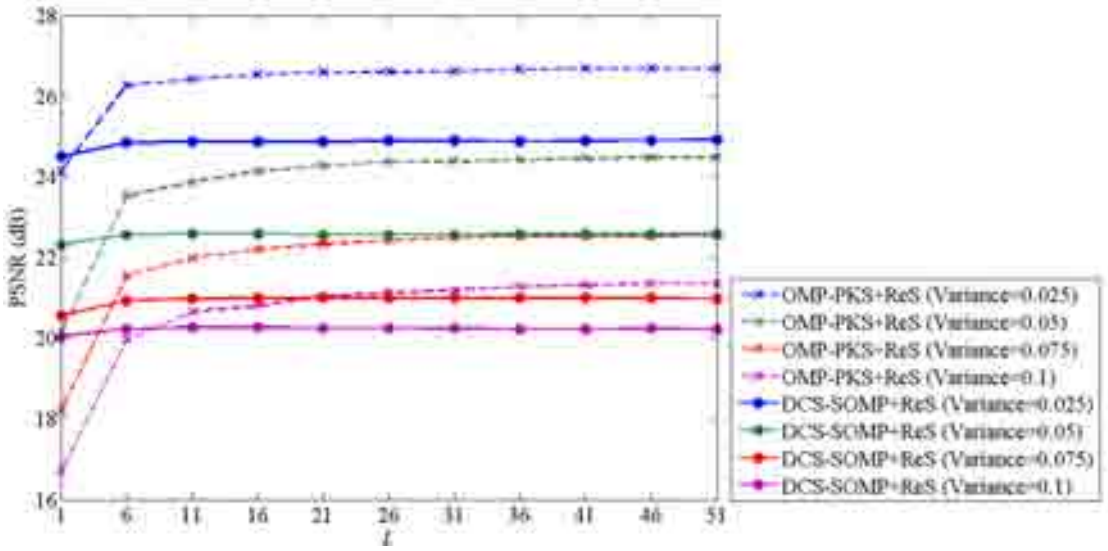

Figure 4.10: The average PSNR of reconstruction images by DCS-SOMP+ReS and OMP-PKS+ReS at M/N = 0.6 from **y** corrupted by different levels (variances) of Gaussian noise.

4.2.3.1 Evaluation by PSNR

Figures 4.11-4.14 show the PSNR when σ^2 was set to 0.025, 0.05, 0.075, and 0.1, respectively. BPDN, LIHT, and OMP-PKS are shown in blue, magenta, and black solid line with circle maker, respectively. OMP-PKS+ReS and DCS-SOMP+ReS are shown in red and green solid line with square marker, respectively. OMP-PKS+RS and DCS-SOMP+RS are shown in red and green dash line with x marker, respectively. When M/N was higher, the reconstruction was better in all cases. However, the effect of the measurement rate to the performance of OMP-PKS+RS was lower than the others techniques.

Figures 4.11-4.14 also indicate that the proposed OMP-PKS+ReS was the most effective reconstruction at all M/N, except at M/N = 0.4, σ^2 = 0.025. The PSNR acquired by the reconstruction from OMP-PKS+ReS and OMP-PKS+RS was approximately the same. When the noise was increased, the reconstruction from the signal ensemble (OMP-PKS+ReS, OMP-PKS+RS, and DCS-SOMP+ReS) was better

than the performance of the reconstruction from one signal (BPDN, LIHT, and OMP-PKS) in all cases but at $M/N = 0.2$.

It should be noted that even though LIHT was designed for the reconstruction of noisy signal, its performance was the worst in almost all cases. This was due to its requirement of very sparse data (or very high M/N). Its performance was still not converged at $M/N = 0.6$; however, M/N could not be increased indefinitely. The major benefit of CS is the capability to reconstruct the signal from small $\mathbf{y}$, so the large M/N will eliminate the CS benefit. For example, at the sparsity rate of 0.1, $M/N = 0.5$ would lead to $\mathbf{y}$ with the size of 50% of the original image size. Such large compressed image could be achieved by conventional image compression techniques. Thus, it was rare that M/N could be increased to 0.5 or larger.

Since OMP-PKS+ReS, OMP-PKS+RS, and OMP-PKS used the same reconstruction method, the PSNR difference between OMP-PKS+ReS, OMP-PKS+RS and OMP-PKS indicated the PSNR improvement by using the ensemble of $\mathbf{y}$. The average PSNR improvement was more than 0.79 dB when $\sigma^2 > 0.025$. The PSNRs from OMP-PKS based ensemble method at $M/N = 0.2$ were higher than the one from OMP-PKS for all σ^2. It indicated that by using the ensemble of signal, OMP-PKS+ReS and OMP-PKS+RS required lower M/N to achieve the same performance level of OMP-PKS.

4.2.3.2 Evaluation by visual inspection

The reconstruction results of seven test images were evaluated in this section. Figures 4.15-4.20 show the reconstruction of Peppers, Woman, Ripple, Arc, Pillar, and Fence, respectively. M/N and σ^2 were 0.3 and 0.1, respectively. The original images are shown in the first column of the top row. The reconstruction results based on BPDN, LIHT, and OMP-PKS are shown in the second, the third, and the fourth columns of the top row, respectively. DCS-SOMP+ReS, OMP-PKS+ReS, DCS-SOMP+RS, and OMP-PKS+RS are shown in the first, the second, the third, and the

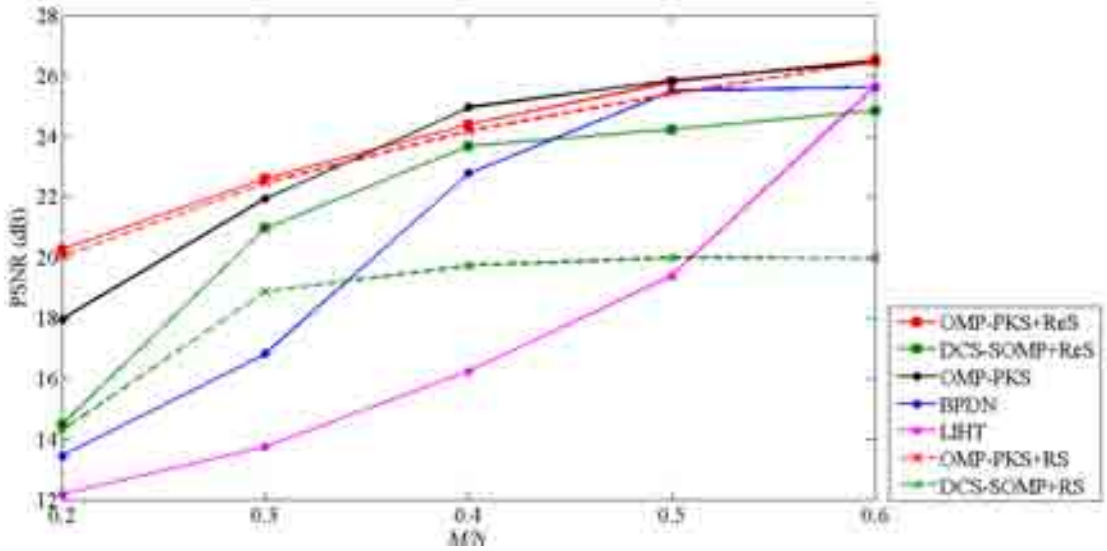

Figure 4.11: The average PSNR of reconstruction images based on BPDN, LIHT, OMP-PKS, OMP-PKS+ReS (L = 21), DCS-SOMP+ReS (L = 6), OMP-PKS+RS (p = 0.6, L = 21), and DCS-SOMP+RS (p = 0.9, L = 6) when $\mathbf{y}$ is corrupted by Gaussian noise with $\sigma^2 = 0.025$.

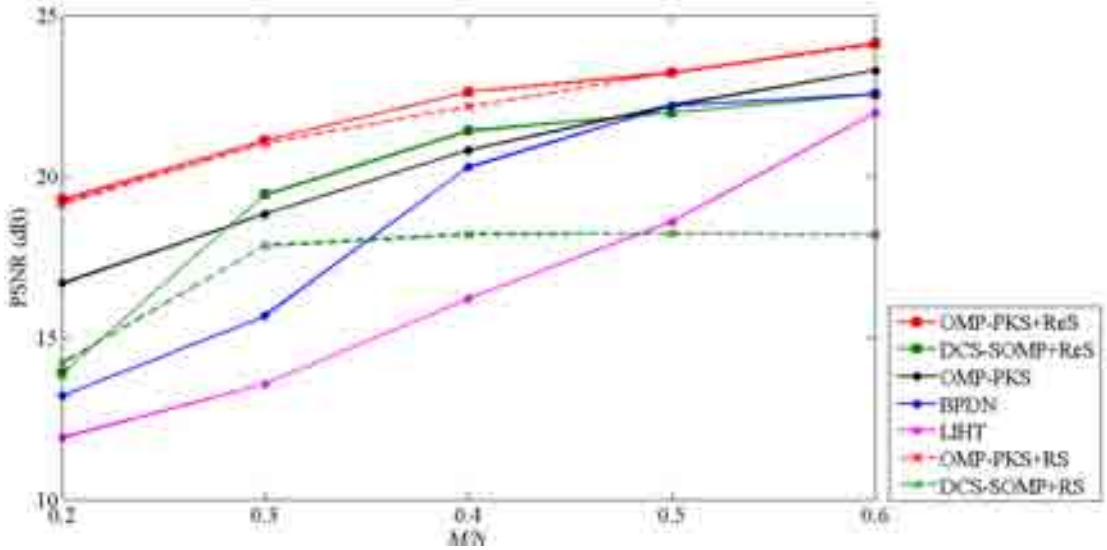

Figure 4.12: The average PSNR of reconstruction images based on BPDN, LIHT, OMP-PKS, OMP-PKS+ReS (L = 21), DCS-SOMP+ReS (L = 6), OMP-PKS+RS (p = 0.6, L = 21), and DCS-SOMP+RS (p = 0.9, L = 6) when $\mathbf{y}$ is corrupted by Gaussian noise with $\sigma^2 = 0.05$.

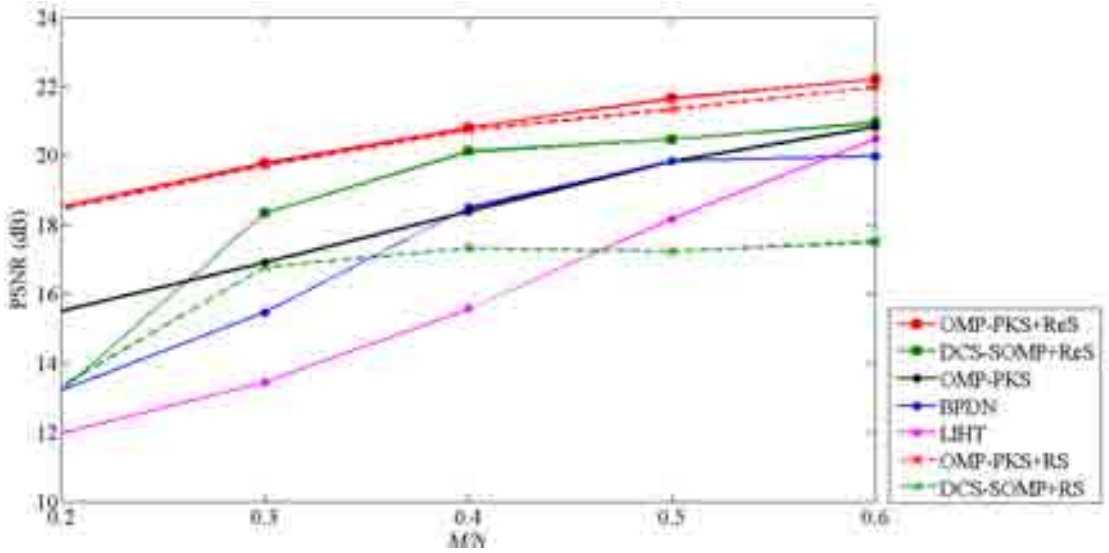

Figure 4.13: The average PSNR of reconstruction images based on BPDN, LIHT, OMP-PKS, OMP-PKS+ReS (L = 21), DCS-SOMP+ReS (L = 6), OMP-PKS+RS (p = 0.6, L = 21), and DCS-SOMP+RS (p = 0.9, L = 6) when **y** is corrupted by Gaussian noise with $\sigma^2 = 0.075$.

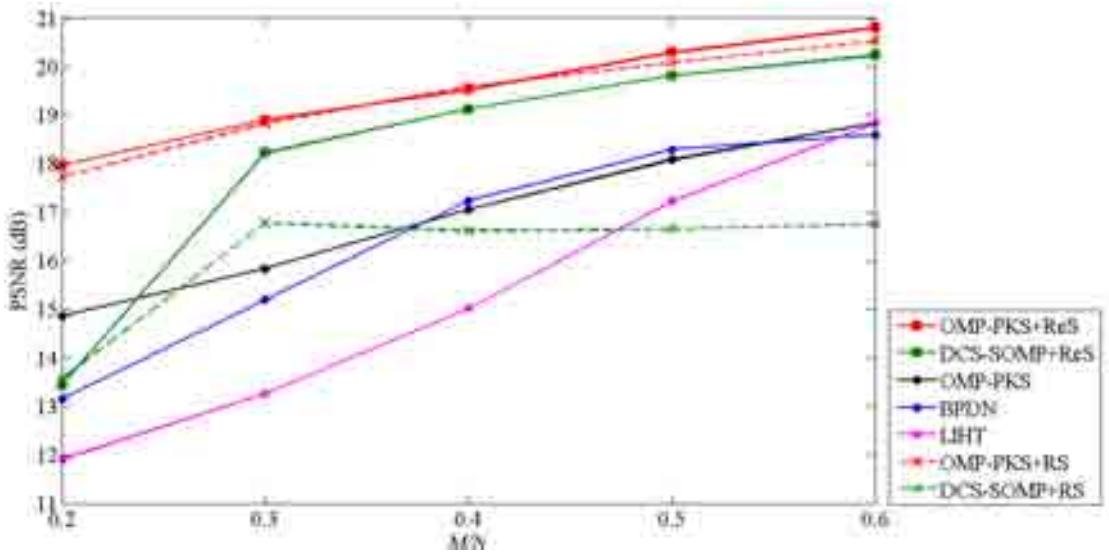

Figure 4.14: The average PSNR of reconstruction images based on BPDN, LIHT, OMP-PKS, OMP-PKS+ReS (L = 21), DCS-SOMP+ReS (L = 6), OMP-PKS+RS (p = 0.6, L = 21), and DCS-SOMP+RS (p = 0.9, L = 6) when **y** is corrupted by Gaussian noise with $\sigma^2 = 0.1$

fourth columns of the bottom row, respectively. BPDN and LIHT failed to reconstruct some blocks as shown as dark dots (such as on the face of woman in Figure 4.16, the middle of the vertical pillar in Figure 4.19). DCS-SOMP+ReS method gave the results that were too smoothed in some regions and noisy in some other regions. The results by DCS-SOMP+ReS contained less noise but in some case (Figure 4.15-4.16, 4.19-4.20), most of its information was smoothed out. OMP-PKS, OMP-PKS+ReS and OMP-PKS+RS successfully reconstructed all seven images. The reconstruction by OMP-PKS+ReS and OMP-PKS+RS provided the result that was not oversmoothed; most edges were visible and Gaussian noise was suppressed in most area. In all images, the change in the intensity contrast was due to the normalization of the inverse wavelet transform.

The PSNR performance and visual quality of the proposed OMP-PKS+ReS and OMP-PKS+RS were very close. Moreover, the optimum L for both methods was 21. However, the size of a sampled signal in the ensemble of OMP-PKS+RS ($p = 0.6$) was smaller than the one of OMP-PKS+ReS ($p = 1$). Thus, the processing time of OMP-PKS+RS was lower. It can then be concluded that OMP-PKS+RS was more optimal than OMP-PKS+ReS.

The reason behind the noise reduction of OMP-PKS+RS and OMP-PKS+ReS was that the reconstruction based on OMP-PKS+ReS and OMP-PKS+RS produced different result for difference signal in the ensemble; therefore, the noise in each pixel could be reduced by averaging the intensity among signals in the ensemble. On the other hand, DCS-SOMP+ReS and DCS-SOMP+RS tried to find one result for every signal in the ensemble. Because the ensemble came from only one signal; hence, the noise was the same and the noise went directly to the result.

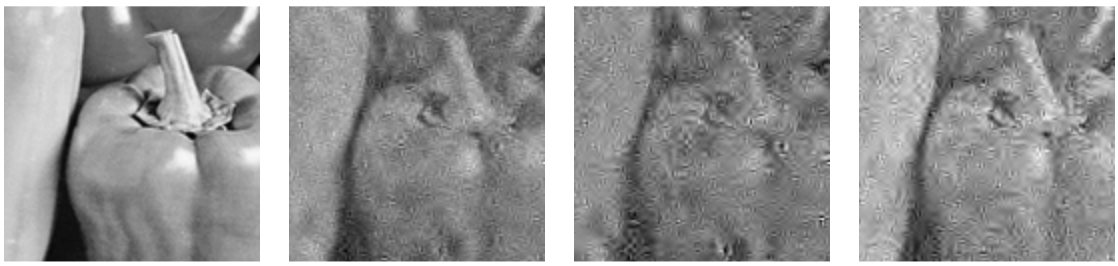

Original image | BPDN (PSNR = 17.06 dB) | LIHT (PSNR = 14.59 dB) | OMP-PKS (PSNR = 17.61 dB)

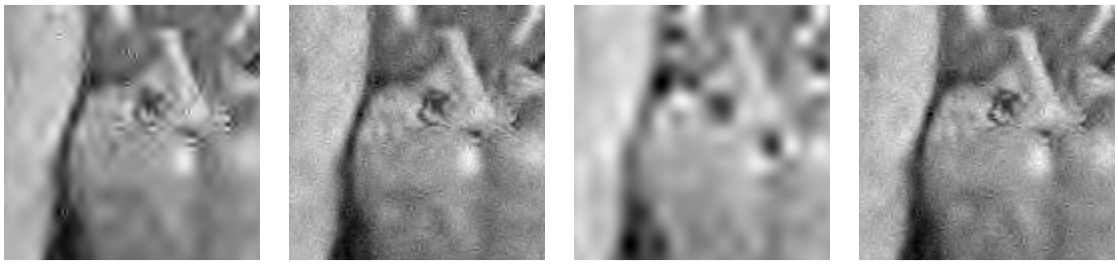

DCS-SOMP+ReS (PSNR = 19.18 dB) | OMP-PKS+ReS (PSNR = 20.89 dB) | DCS-SOMP+RS (PSNR= 18.45 dB)) | OMP-PKS+RS (PSNR= 20.91 dB)

Figure 4.15: Comparisons of the reconstructed Peppers with $M/N = 0.3$ and $\sigma^2 = 0.1$.

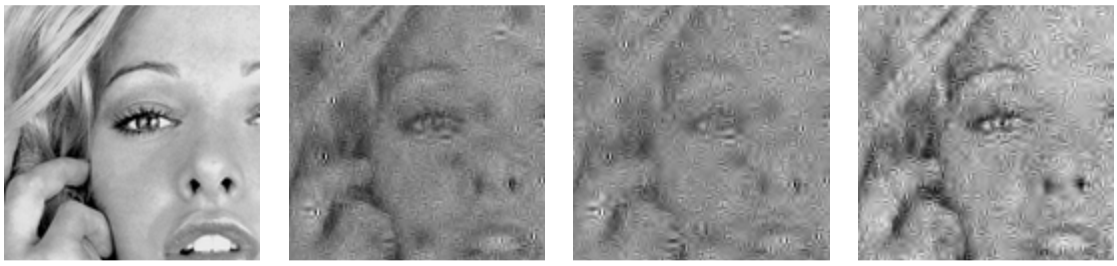

Original image | BPDN (PSNR = 14.65 dB) | LIHT (PSNR = 14.80 dB) | OMP-PKS (PSNR = 16.56 dB)

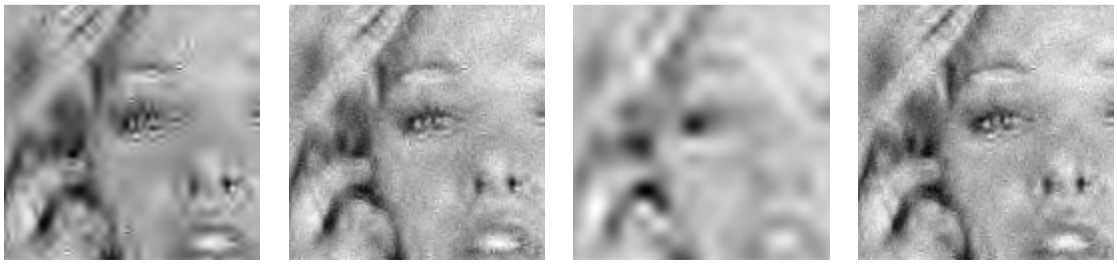

DCS-SOMP+ReS (PSNR = 19.81 dB) | OMP-PKS+ReS (PSNR = 21.34 dB) | DCS-SOMP+RS (PSNR = 19.34 dB) | OMP-PKS+RS (PSNR = 21.53 dB)

Figure 4.16: Comparisons of the reconstructed Woman with $M/N = 0.3$ and $\sigma^2 = 0.1$.

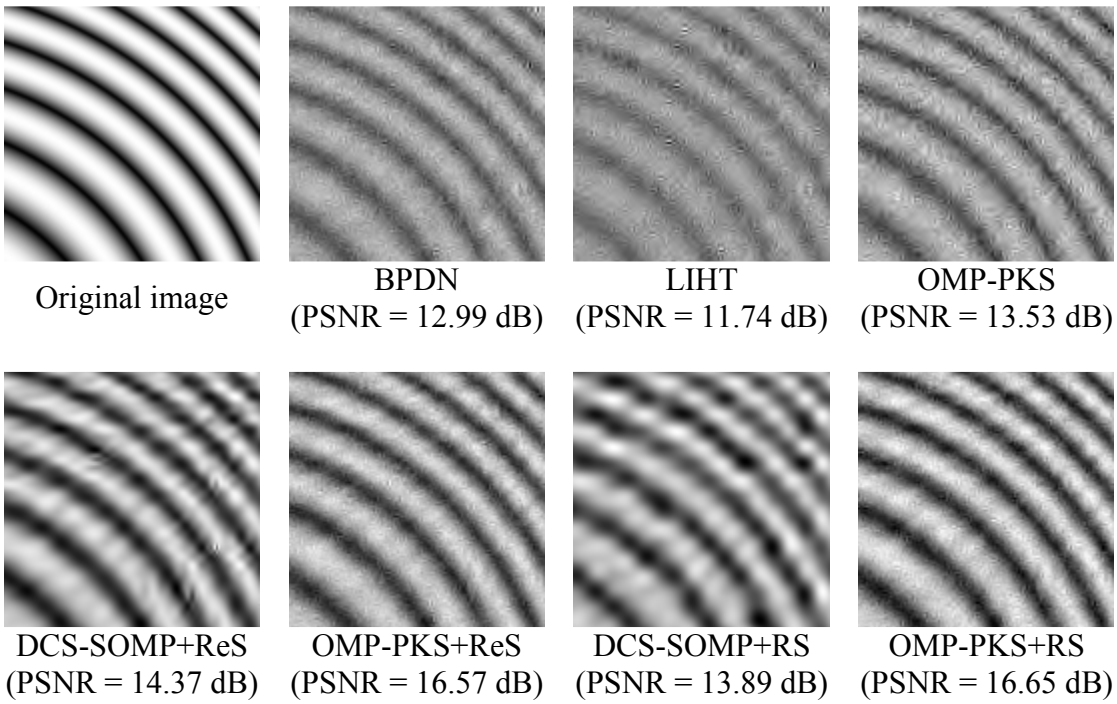

Figure 4.17: Comparisons of the reconstructed Ripple with $M/N = 0.3$ and $\sigma^2 = 0.1$.

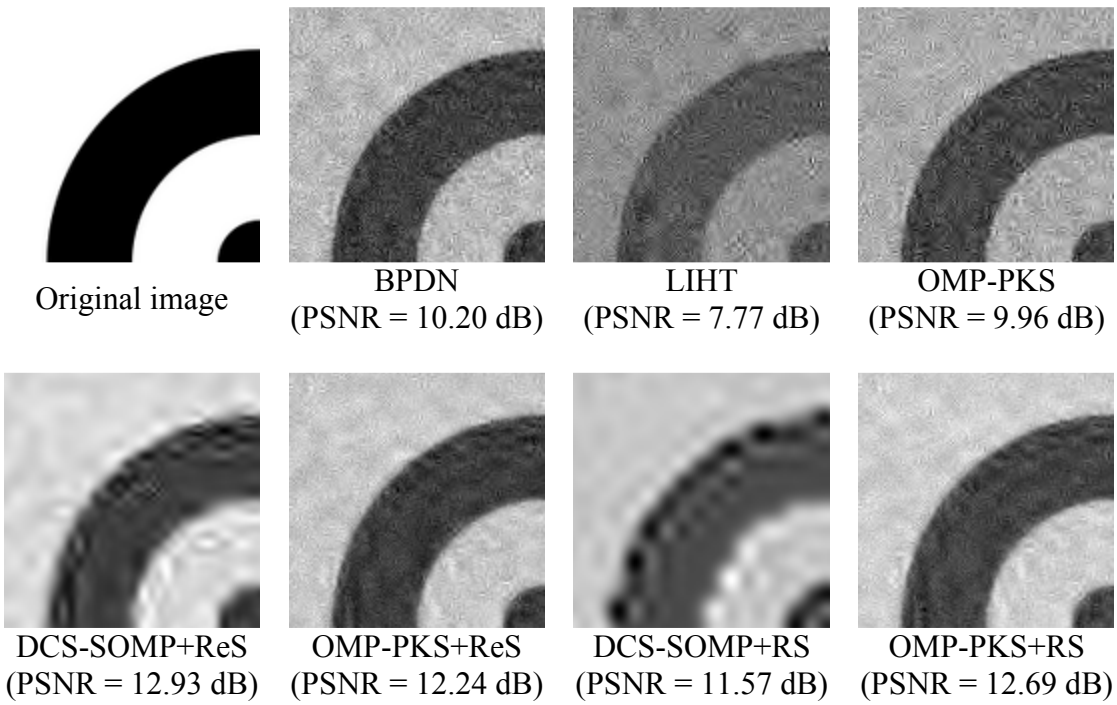

Figure 4.18: Comparisons of the reconstructed Arc with $M/N = 0.3$ and $\sigma^2 = 0.1$.

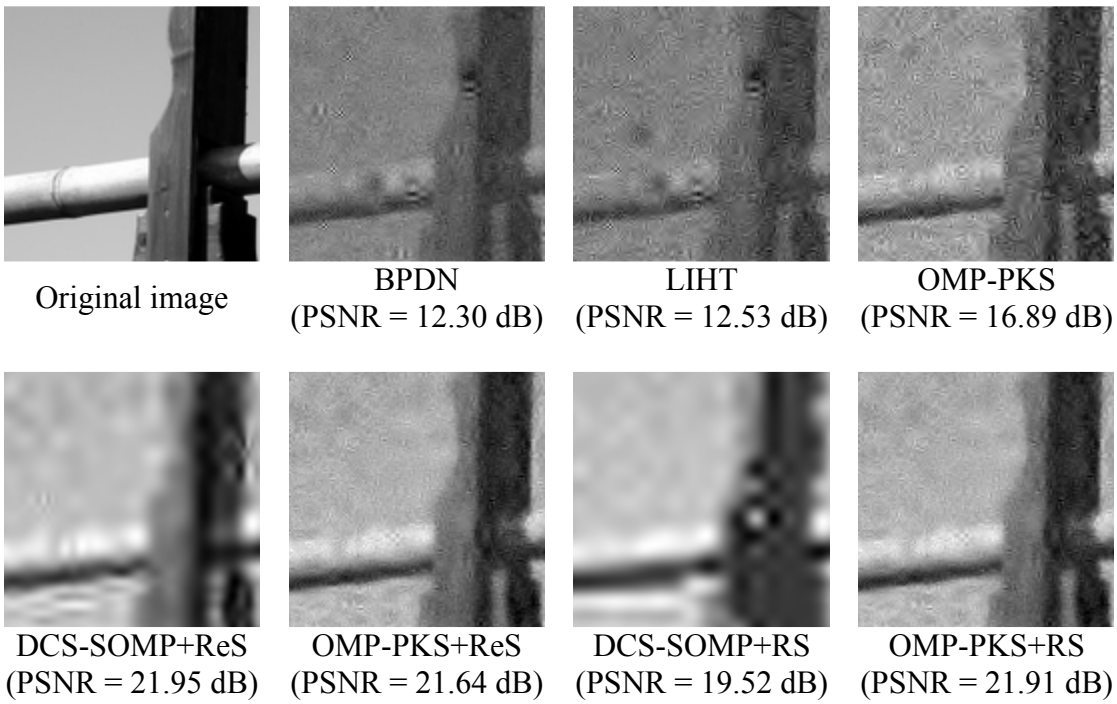

Figure 4.19: Comparisons of the reconstructed Pillar with $M/N = 0.3$ and $\sigma^2 = 0.1$.

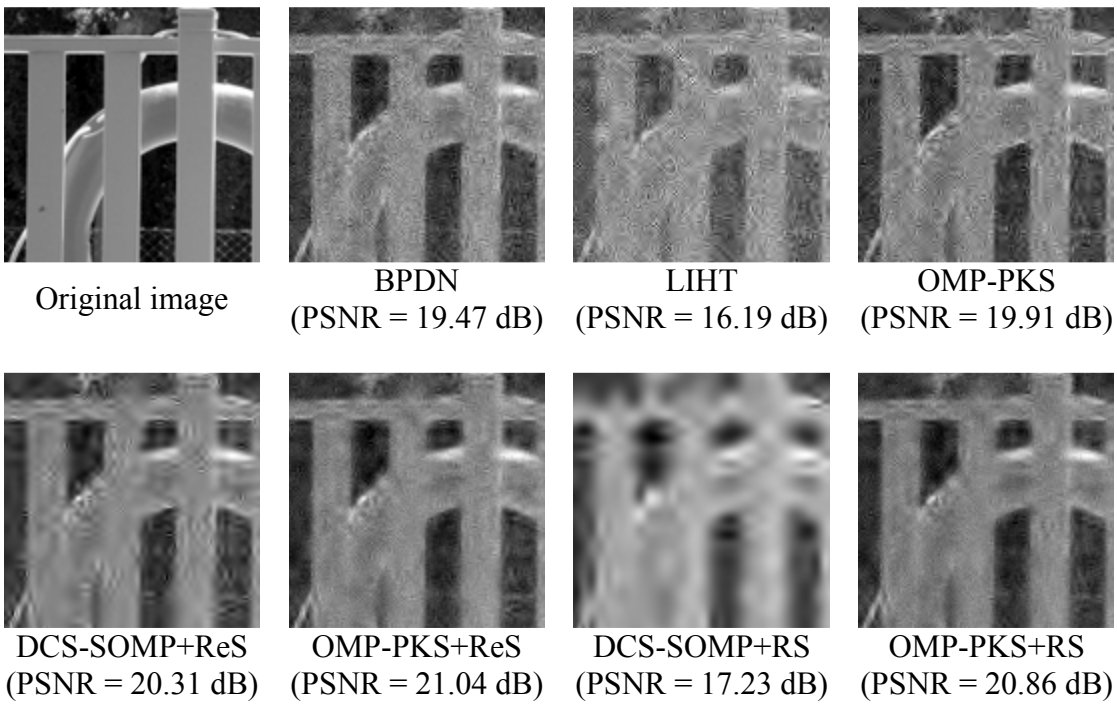

Figure 4.20: Comparisons of the reconstructed Fence with $M/N = 0.3$ and $\sigma^2 = 0.1$.

4.3 Experiment on impulsive noise environment

In this section, the performance of OMP-PKS with the proposed rejection method as the preprocessing (OMP-PKS+R) was investigated. The probability of impulsive noise is denoted as q; $q \in \{0, 0.05, 0.10, 0.15, 0.20\}$. The magnitude of impulsive noise was set relative to the maximum magnitude in $\mathbf{y}$ ($y_{\max}$). The experiment consists of two parts: (1) the evaluation of the two thresholds (η and T) and the minimum size of the detectable impulsive noise in Subsection 4.3.1 and (2) the performance evaluation of the proposed method in Subsection 4.3.2

4.3.1 Evaluation of the two thresholds and the minimum size of the detectable impulsive noise

In this section, 500 blocks were randomly selected from blocks in 40 test images. The sparsity rate was fixed at 0.1. Figure 4.21 shows the relationship between the energy ratio threshold (η) and the percent that the proposed method was unable to correctly reject the impulsive noise corrupted elements. The result form different magnitudes of impulsive noise are shown in different color. The value in the figure was the value averaged over five values of q and five values of measurement rates (M/N) which were 0.2, 0.3, 0.4, 0.5, and 0.6. The result indicated that percent of inaccurate rejection decreased when the magnitude of the impulsive noise was increased. From further investigation, it was found that the proposed impulsive noise rejection method was unable to keep the percent of inaccurate rejection to less than 0.5% if the magnitude of the impulsive noise was less than 2.5 $y_{\max}$.

Figure 4.21 also indicated the relationship of η to the percent of inaccurate rejection. The inaccurate rejection was the result of (1) the rejection of the noise-free elements and (2) the failure to reject the noise corrupted elements. When η was too small, the energy-ratio criterion was too strict and the proposed method did not accept even the correct energy distribution of $\hat{\mathbf{s}}$; consequently, it started to remove the elements uncorrupted by noise. In the opposite case, when η was too large, the energy-ratio criterion became too lax and the proposed method accepted even the

incorrect energy distribution of $\hat{\mathbf{s}}$; consequently, it failed to remove the noise corrupted elements. The range of η giving less than 0.5% of inaccurate rejection was larger, when the magnitude of the impulsive noise was larger. This was because the effect of the impulsive noise to the energy distribution became more distinct and easier to detect when the size of the noise was larger. When the magnitude of the impulsive noise was at least $2.5y_{\max}$, the values of η giving less than 0.5% inaccurate rejection were 0.07 to 0.22. Among these values, the values of η = 0.1 gave the most accurate rejection.

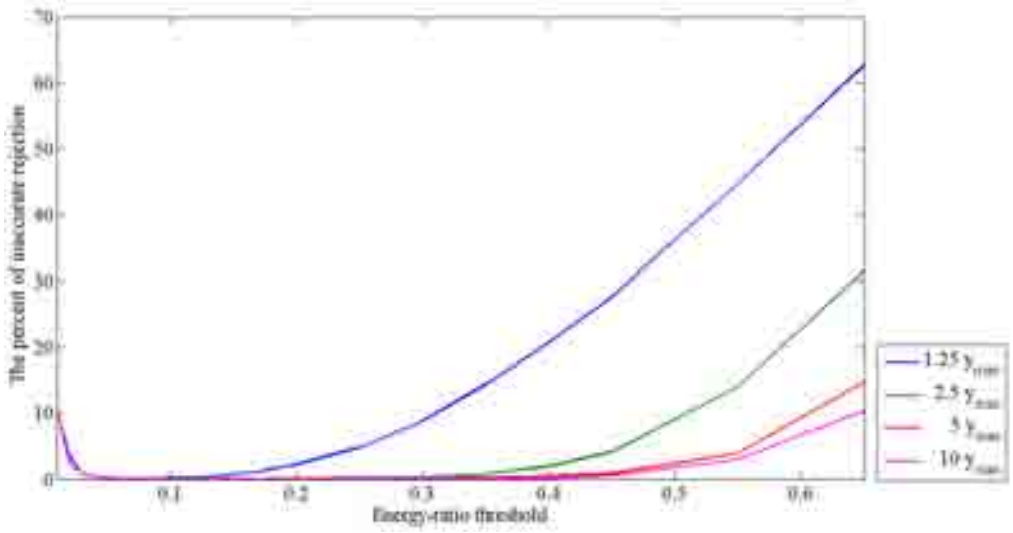

Figure 4.21: The percent of inaccurate rejection of OMP-PKS+R from y corrupted by impulsive noise when η ((leakage) energy-ratio threshold) was varied.

The evaluation for the optimum rejection-ratio threshold, *T*, was performed by investigating for the maximum number of the elements in **y** that can be removed without causing the high error between $\hat{\mathbf{s}}$ and **s**. Figure 4.22 shows the MSE of the signals reconstructed by OMP-PKS when *TM* elements in **y** were removed. Different *M*/*N* are presented with different colors. The figure indicates that when *M*/*N* increased, more elements could be removed without causing a drastic change in MSE. At *M*/*N* = 0.2, MSE approximately increased at the exponential rate, when *T* was

larger or equal to 0.45. At the higher measurement rates, the effect of T was not distinct, even when more than half of **y** was removed.

Because the benefit of CS is the capability of compressing the signal to very small size, M/N should be kept low. It is recommended that T be selected such that it is applicable even at low measurement rate. In the following section, T was set to 0.4 to ensure the high probability of successful reconstruction. The value of η was set to 0.1 as it was the optimal value.

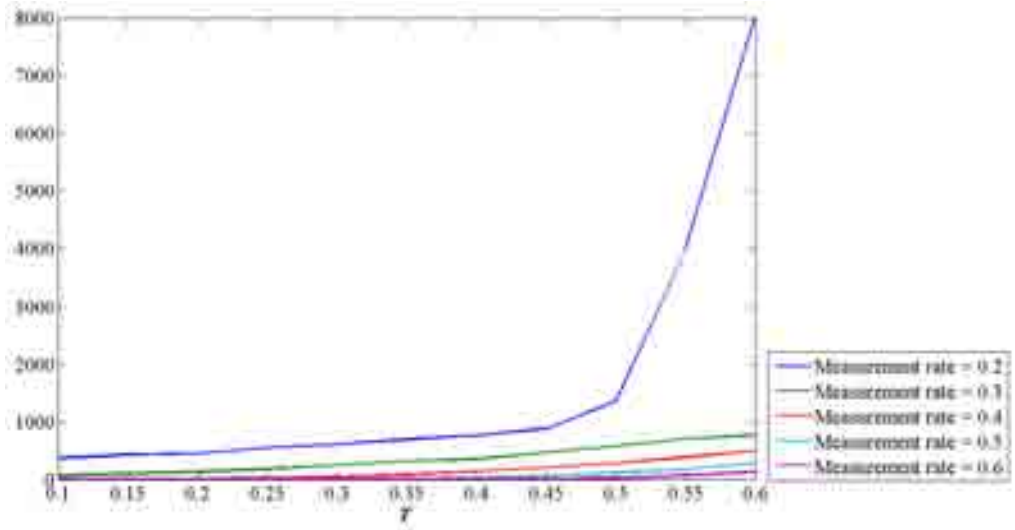

Figure 4.22: The MSE of the reconstructed signal when T was varied. The sparsity rate was set to 0.1

4.3.2 Performance Evaluation

In this section, the following four reconstruction methods were investigated.

- OMP-PKS
- OMP-PKS+R
- LIHT
- LIHT with the proposed rejection method as the preprocessing (LIHT+R)

The Lorentzian parameter and the number of iteration for LIHT were 0.25 and 100, respectively. The values of η and T were 0.1 and 0.4, respectively. There were 256 **y**'s in an image and $y_{\max}$ was chosen as the maximum magnitude among 256 **y**'s in the image. The magnitude of impulsive noise varied according to the Gaussian pdf with the mean of $7y_{\max}$ and the standard deviation of $y_{\max}$. The performance is evaluated based on the PSNR of the reconstructed images, the computational time and the visual quality of the reconstructed images.

The experiments in Figures 4.23-4.27 show the average results of the 40 test images. Figures 4.23-4.27 show the PSNR (subfigure a) and the computational time (subfigure b) at different q (noise probability). At $q = 0$ (noiseless) in Figure 4.23(a), the addition of the proposed method to OMP-PKS and LIHT did not reduce the PSNR of the reconstructed images. It indicated that the proposed method preserved **y** when there was no impulsive noise. When **y** was corrupted by impulsive noise ($q > 0$) in Figures 4.24(a)-4.27(a), the reconstruction based on OMP-PKS (the blue line) gave very low PSNR, because OMP-PKS is designed with the assumption of bounded noise. The reconstruction based on OMP-PKS could not be improved by increasing M/N. However, when the noisy **y** was preprocessed by the proposed method, the reconstruction based on OMP-PKS (the dashed blue line) was very effective. At $M/N = 0.4$ and higher, the reconstruction from the noisy **y** by OMP-PKS+R had the comparable PSNR to the reconstruction from the noiseless **y** by OMP-PKS.

At $p = 0.05$ in Figure 4.24(a), the effect of adding the proposed method as the preprocessing to LIHT was minimal; however, at higher q, the addition of the proposed method (the dashed red line) resulted in higher PSNR than the reconstruction by LIHT alone (the red line). When q was 0.15 or higher as shown in Figures 4.26(a)-4.27(a), LIHT was no longer an effective reconstruction method, but LIHT+R was still effective. It indicated that the addition of the proposed method increased the robustness against q to LIHT.

It should be noted that even though LIHT was based on LIHT which was designed to be robust against impulsive noise. LIHT+R provided less PSNR than OMP - PKS + R, because LIHT required the higher M/N. Figures 4.23(a)-4.27(a)

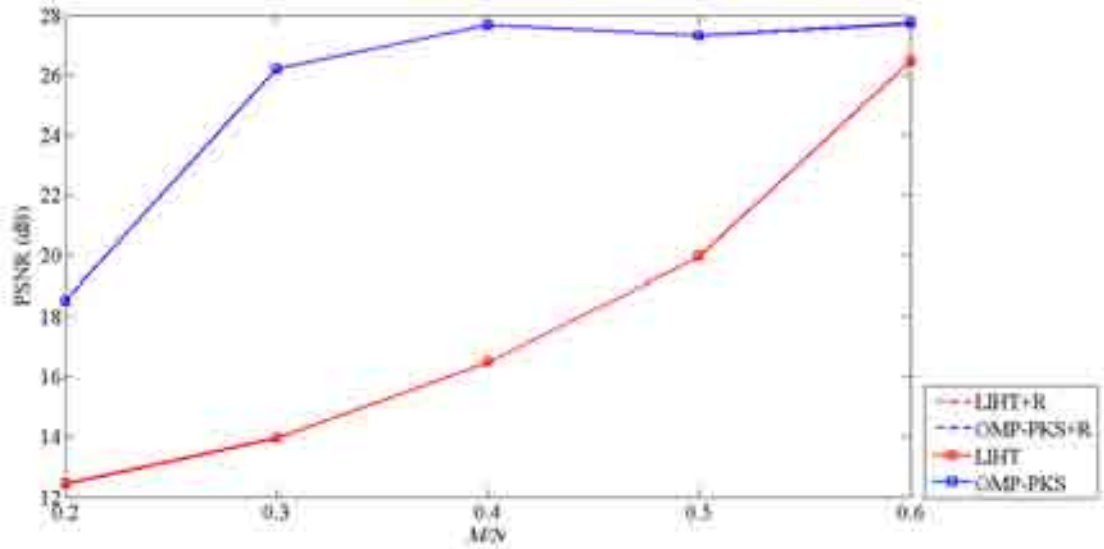

(a)

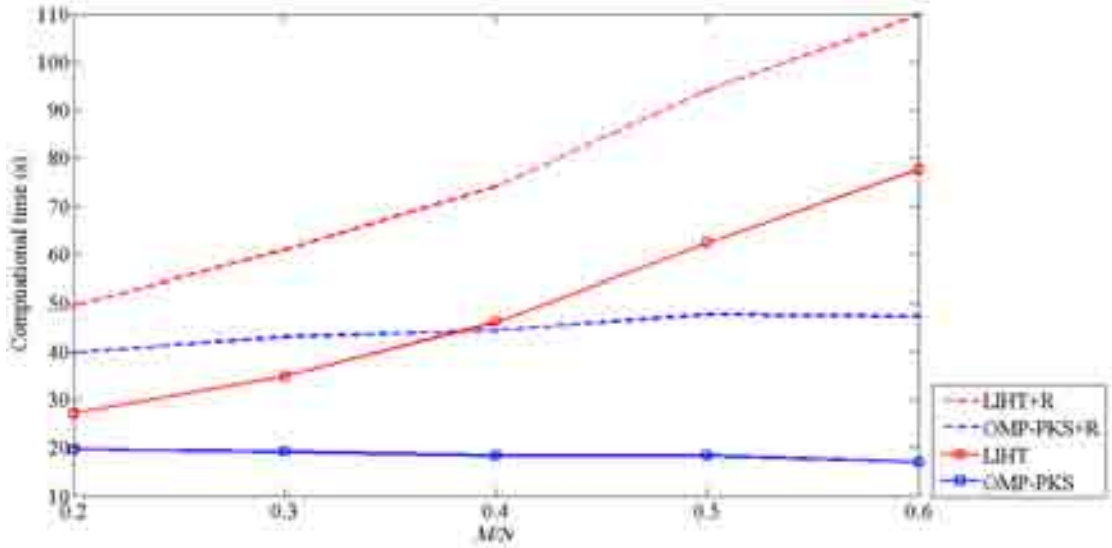

(b)

Figure 4.23: The performance comparisons in term of (a) PSNR and (b) computational time at various M/N when $q = 0$.

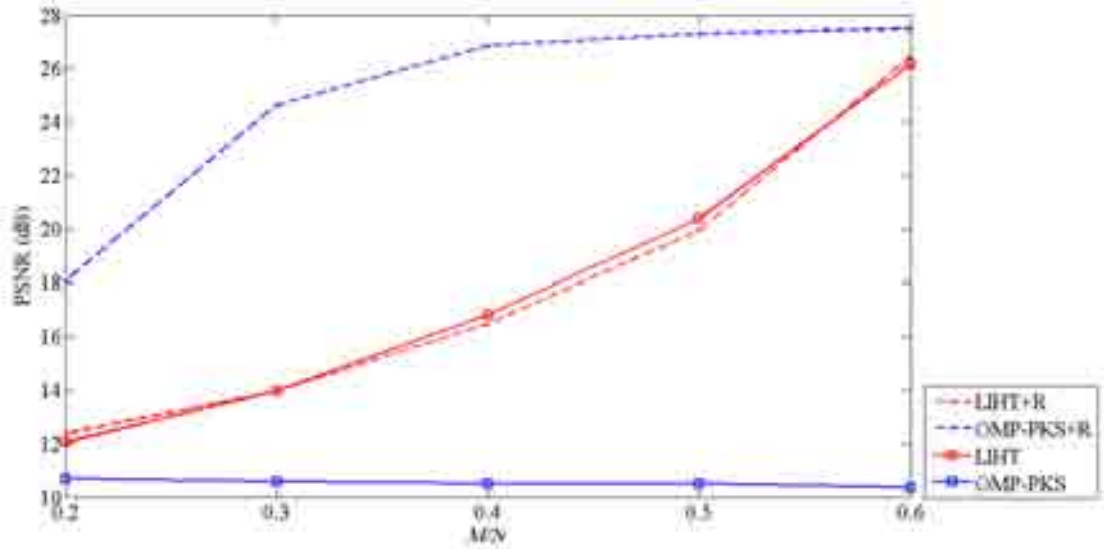

(a)

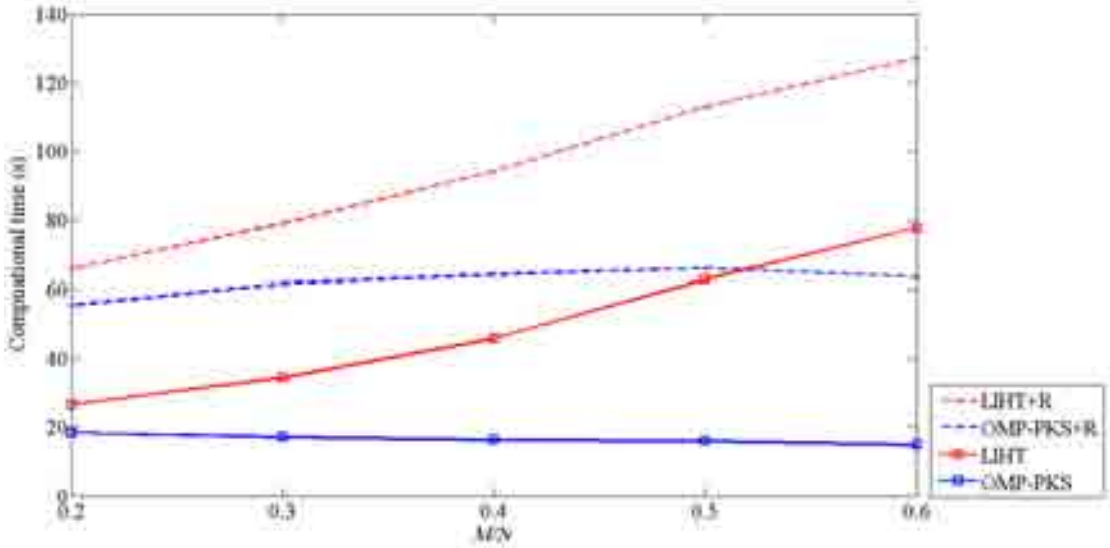

(b)

Figure 4.24: The performance comparisons in term of (a) PSNR and (b) computational time at various M/N when noise $q = 0.05$.

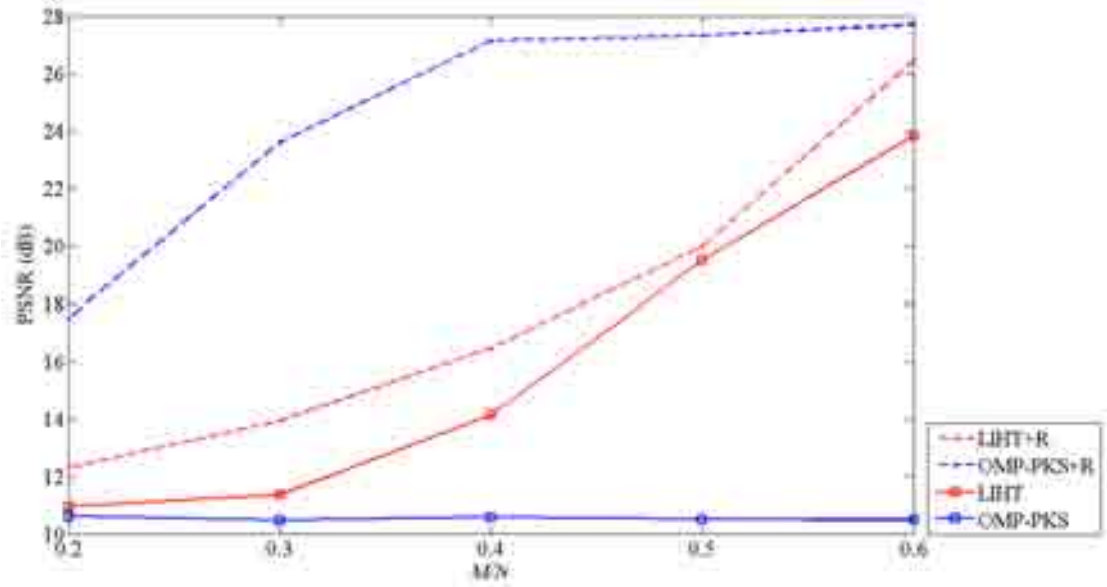

(a)

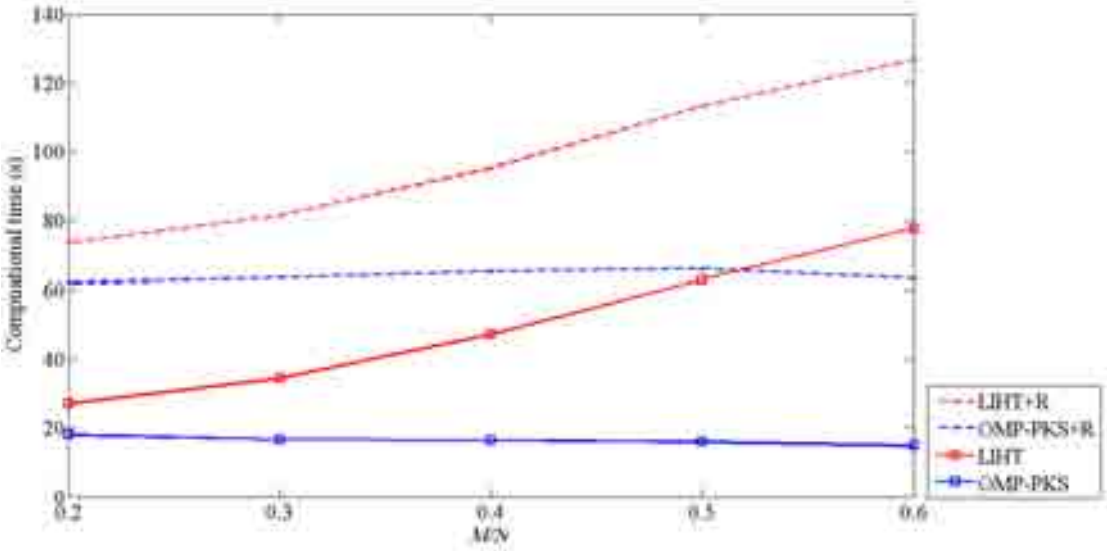

b)

Figure 4.25: The performance comparisons in term of (a) PSNR and (b) computational time at various M/N when $q = 0.1$.

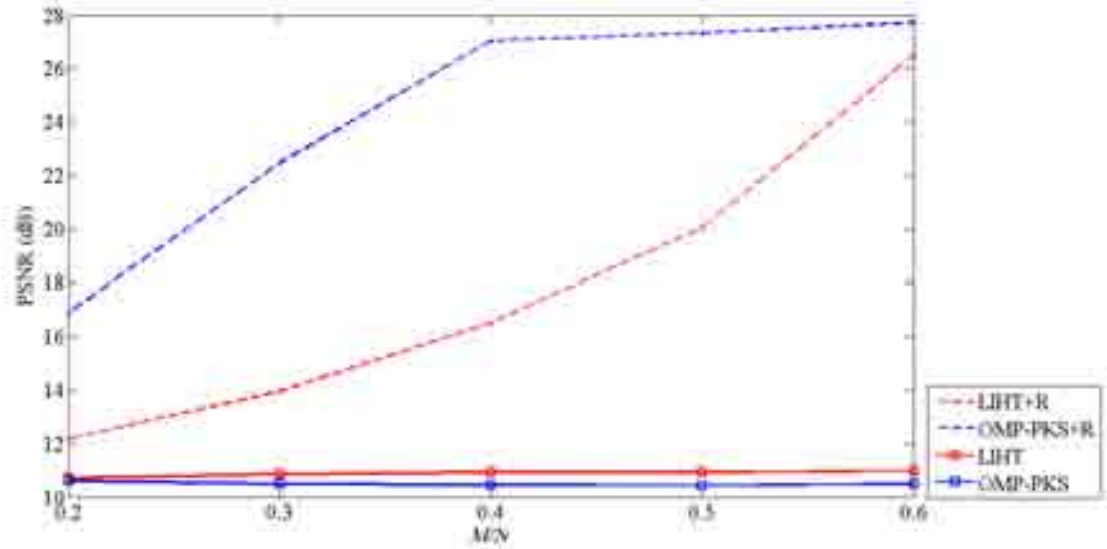

(a)

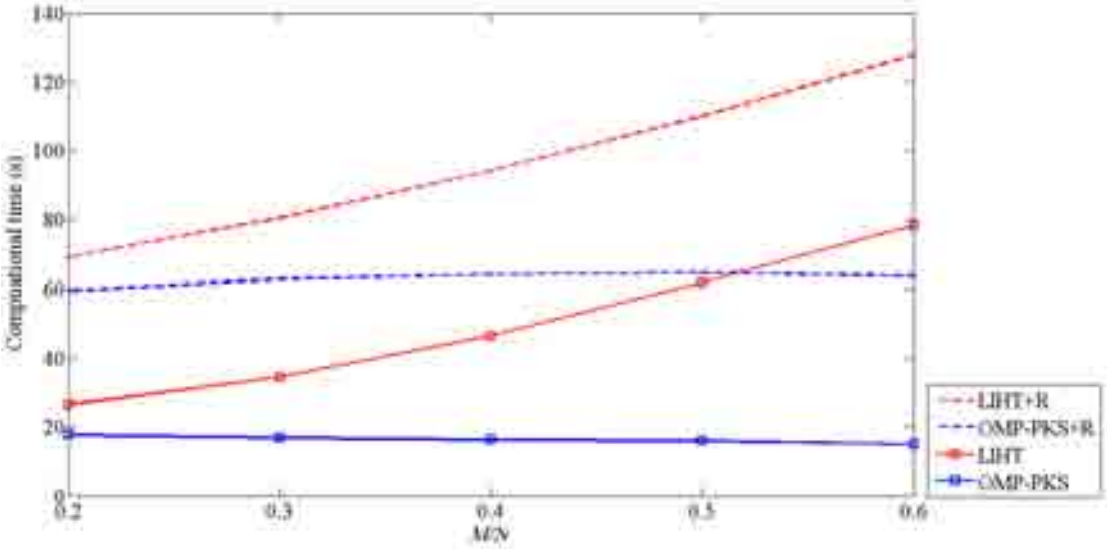

(b)

Figure 4.26: The performance comparisons in term of (a) PSNR and (b) computational time at various M/N when $q = 0.15$.

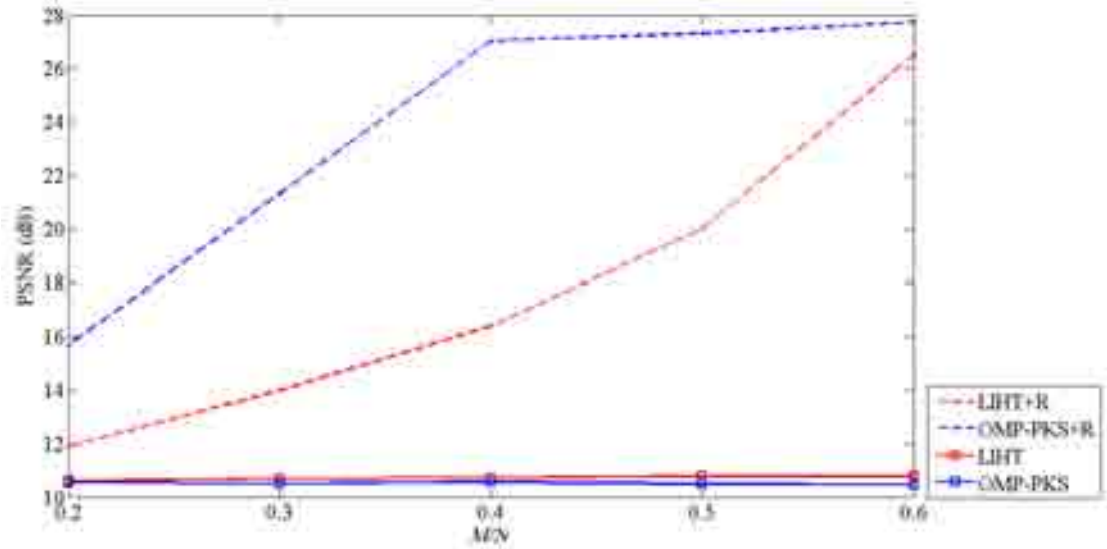

(a)

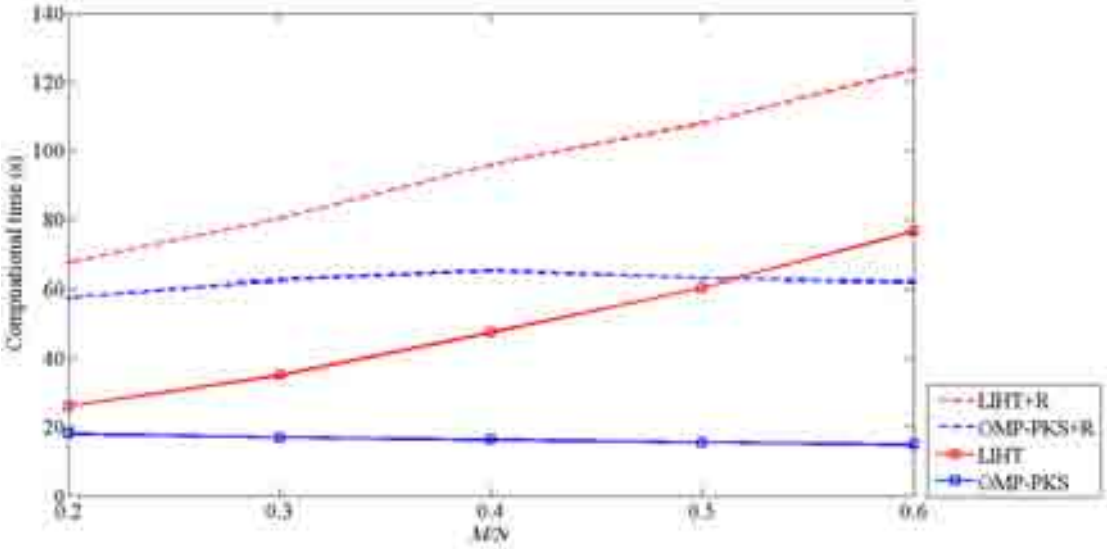

(b)

Figure 4.27: The performance comparisons in term of (a) PSNR and (b) computational time at various M/N when $q = 0.2$.

indicated that LIHT+R provide the most effective PSNR when M/N was 0.6 and it should become better at the higher M/N. However, the improvement by increasing M/N is not recommended because it leads to the large size of $\mathbf{y}$ and eliminates the benefit of CS.

Figures 4.23(a)-4.27(a) also indicates the relationship between M/N and q. When q was higher, M/N should be set higher. This was because the number of the noise corrupted elements was larger at higher q. Consequently, the larger size of $\mathbf{y}$ was required to cope with the removal of more elements. The figures show that in OMP-PKS+R, M/N of 0.4 gave the good reconstruction for all q in this experiment.

Figures 4.23(b)-4.27(b) show the computational time of OMP-PKS, OMP-PKS+R, LIHT and LIHT+R. Since at least one reconstruction is required in the proposed method, the computation time will be at least doubled. The computational time for reconstructing 256 blocks in an image could be reduced as follows.

a) Apply the proposed rejection method to the first block. Define β as the smallest magnitude of the noise corrupted elements in the first block.
b) Move to the next block. Define the compressed measurement of the new block as $\mathbf{y}_{curr}$.
c) Assign the elements in $\mathbf{y}_{curr}$ having the magnitude not less than β as the impulsive noise. Initialize variables in Step a) of Section 3.3.1 such that they reflect the removal of the elements with the magnitude not less than β.
d) Apply the proposed rejection method to $\mathbf{y}_{curr}$. If β is larger than the smallest magnitude of the noise corrupted elements in $\mathbf{y}_{curr}$, set β to this value.
e) If the current block is the last block in the image, terminate. Otherwise, go to step b).

The assumption of the above algorithm is that the magnitude of impulsive noise in every block is approximately the same (or share the same distribution). The graphs indicated that the computational time of the reconstruction with the proposed rejection method was no more than 4 times the computational time of the reconstruction without the proposed rejection method.

From the experiments, it could be concluded that the proposed method should be included in the reconstruction from the impulsive noise corrupted **y**. The addition of the proposed method increased the computational time no more than 4 times the original computational time. Finally, OMP-PKS+R was more optimal than LIHT+R.

Figures 4.28-4.33 show the examples of the reconstruction images when M/N is 0.3. The original image is shown in the first column. The reconstruction results based on LIHT, LIHT+R, OMP-PKS and OMP-PKS+R are shown in the second, the third, the fourth and the fifth columns, respectively. When the impulsive noise was added to **y**, the reconstruction based on OMP-PKS failed in every case. The reconstruction based on LIHT failed in some cases at $q = 0.1$, and failed in every case at $q \geq 0.15$. The addition of the proposed algorithm to OMP-PKS and LIHT, namely OMP-PKS+R and LIHT+R led to the successful reconstruction in every case. Furthermore, the reconstruction based on OMP-PKS+R provided the reconstruction results that were more similar to the original images than the ones based on LIHT+R. These results complied with the conclusion that was drawn from the PSNR graphs in Figures 4.23-4.27.

4.4 Experiment on Gaussian and impulsive noises environment

The experiments in Sections 4.2 and 4.3 showed that the reconstruction from OMP-PKS+RS and OMP-PKS+R could reduce the effect of Gaussian and impulsive noise. Thus, if **y** is corrupted by both Gaussian and impulsive noise, the combination of OMP-PKS+RS and OMP-PKS+R should be applied. In this section, the proposed method (OMP-PKS+R+RS) is compared with LIHT. The parameters for OMP-PKS+R+RS were analyzed in the previous sections. p, L and T were set to 0.6, 21, and 0.4, respectively.

The experiment consists of two parts: (1) evaluation for η in Section 4.4.1 and (2) performance evaluation in Section 4.4.2.

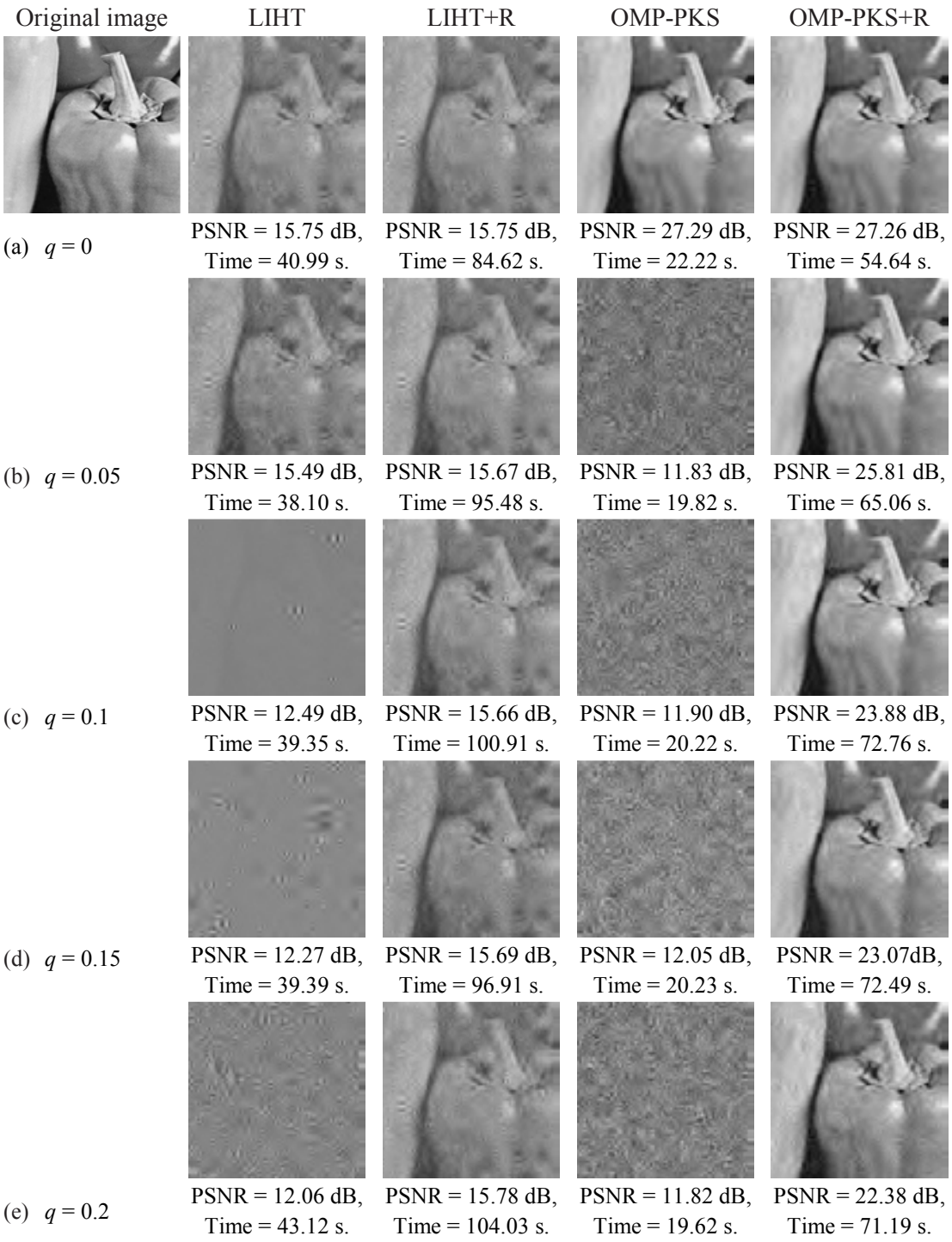

Figure 4.28: The part of the reconstructed Peppers at M/N = 0.3 with the noise probability (q) of (a) 0, (b) 0.05, (c) 0.1, (d) 0.15 and (e) 0.2. The images from left to right are the original image and reconstructed images based on LIHT, LIHT+R, OMP-PKS and OMP-PKS+R, respectively.

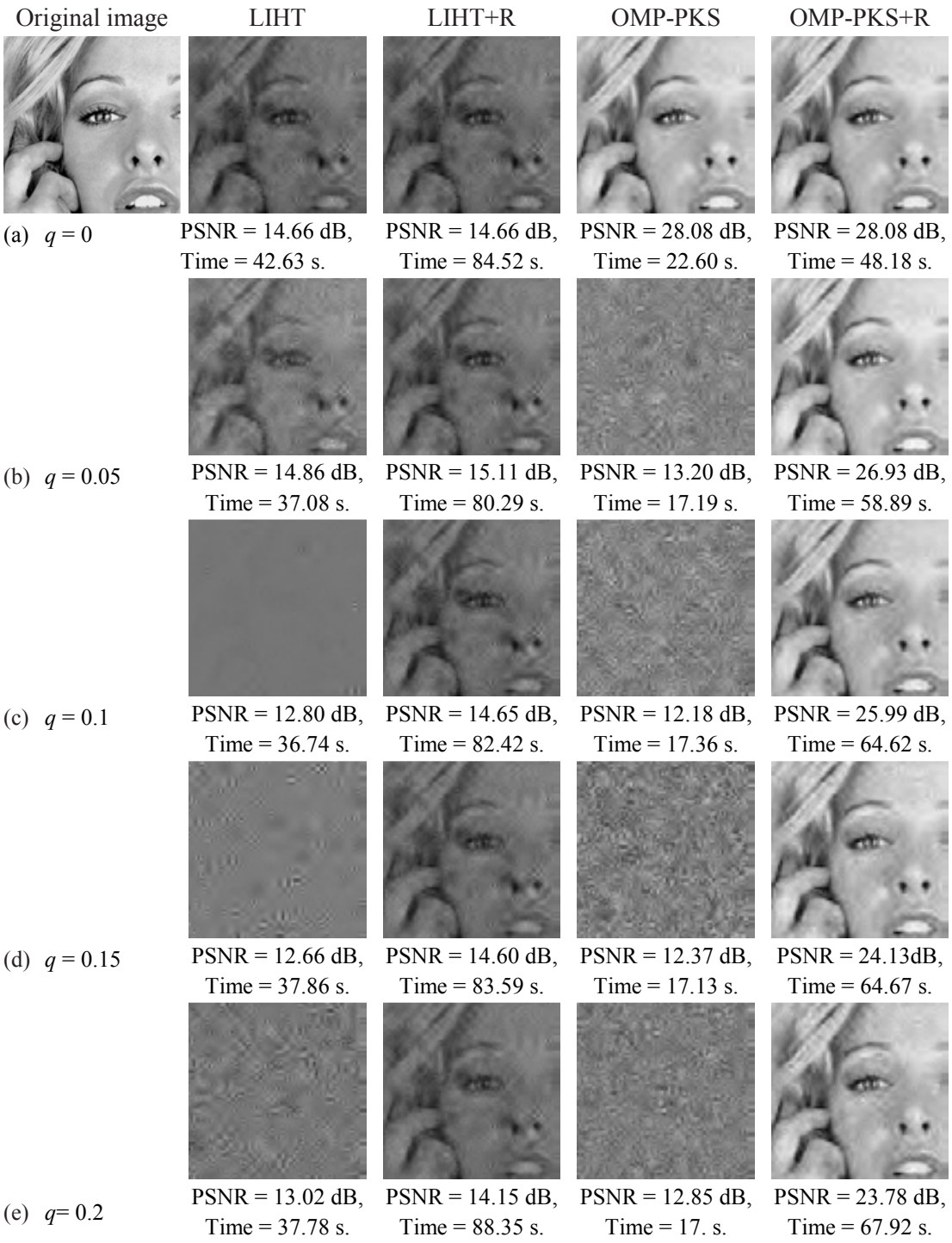

Figure 4.29: The part of the reconstructed Woman at M/N = 0.3 with the noise probability (q) of (a) 0, (b) 0.05, (c) 0.1, (d) 0.15 and (e) 0.2. The images from left to right are the original image and reconstructed images based on LIHT, LIHT+R, OMP-PKS and OMP-PKS+R, respectively.

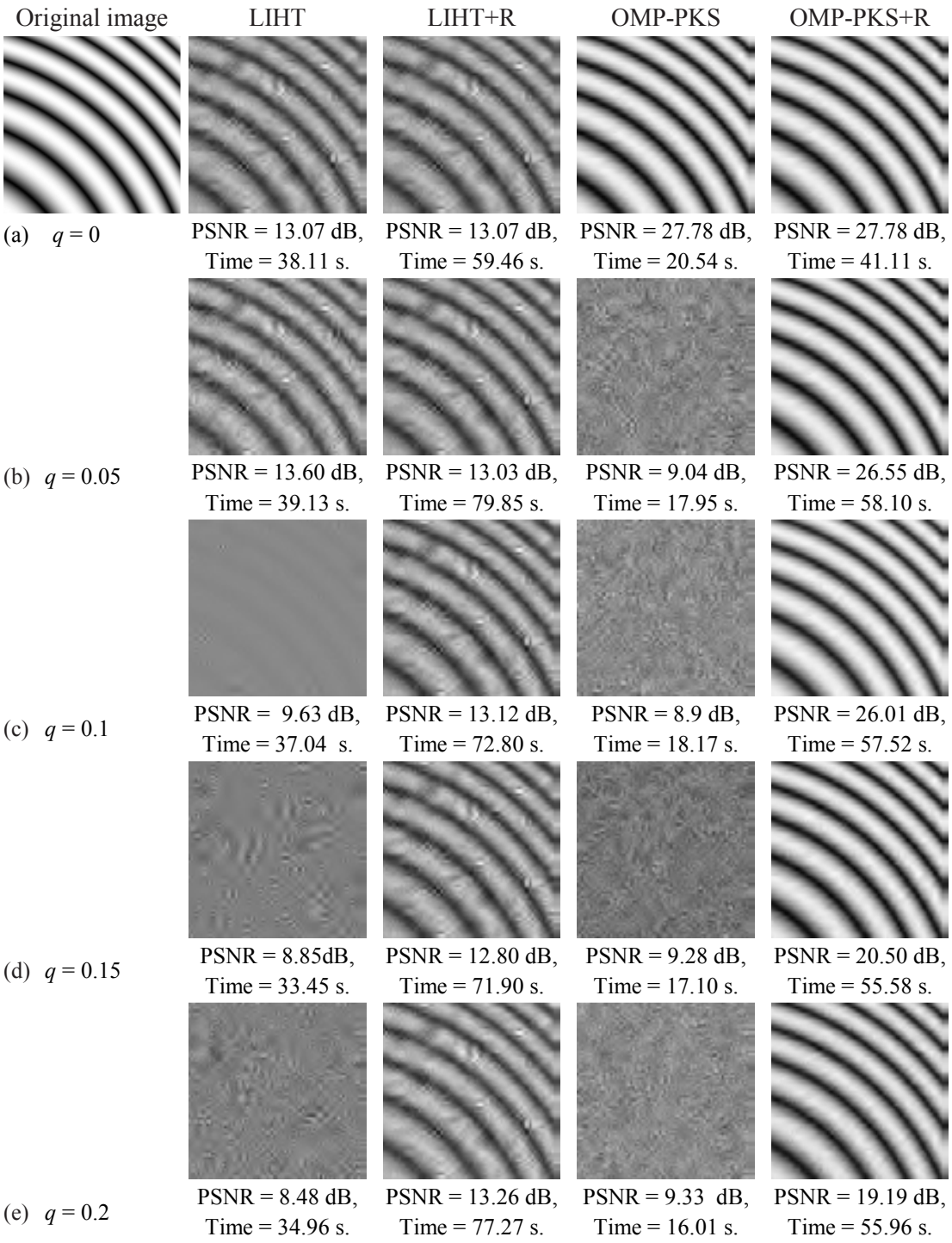

Figure 4.30: The part of the reconstructed Ripple at $M/N = 0.3$ with the noise probability (q) of (a) 0, (b) 0.05, (c) 0.1, (d) 0.15 and (e) 0.2. The images from left to right are the original image and reconstructed images based on LIHT, LIHT+R, OMP-PKS and OMP-PKS+R, respectively.

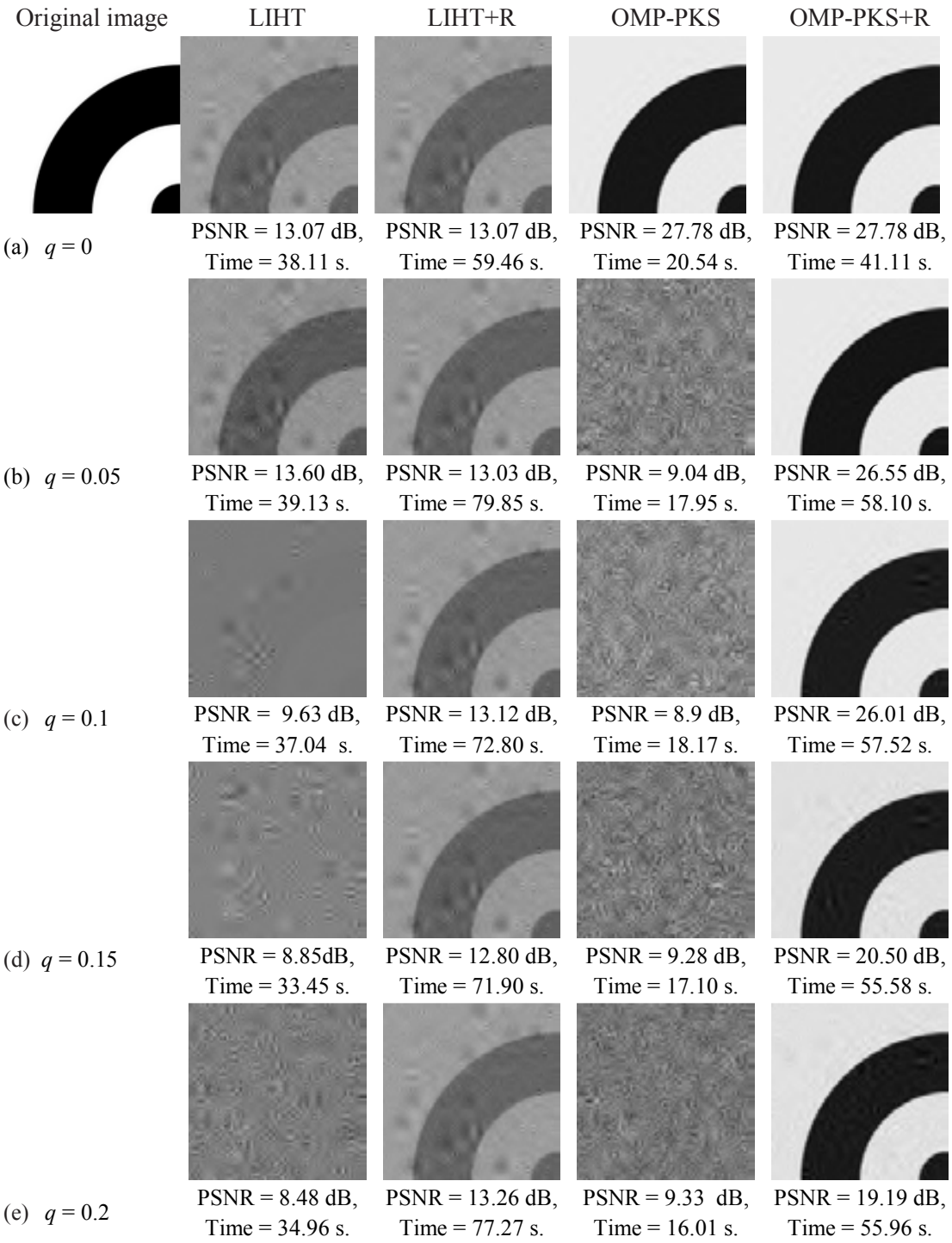

Figure 4.31: The part of the reconstructed Arc at $M/N = 0.3$ with the noise probability (q) of (a) 0, (b) 0.05, (c) 0.1, (d) 0.15 and (e) 0.2. The images from left to right are the original image and reconstructed images based on LIHT, LIHT+R, OMP-PKS and OMP-PKS+R, respectively.

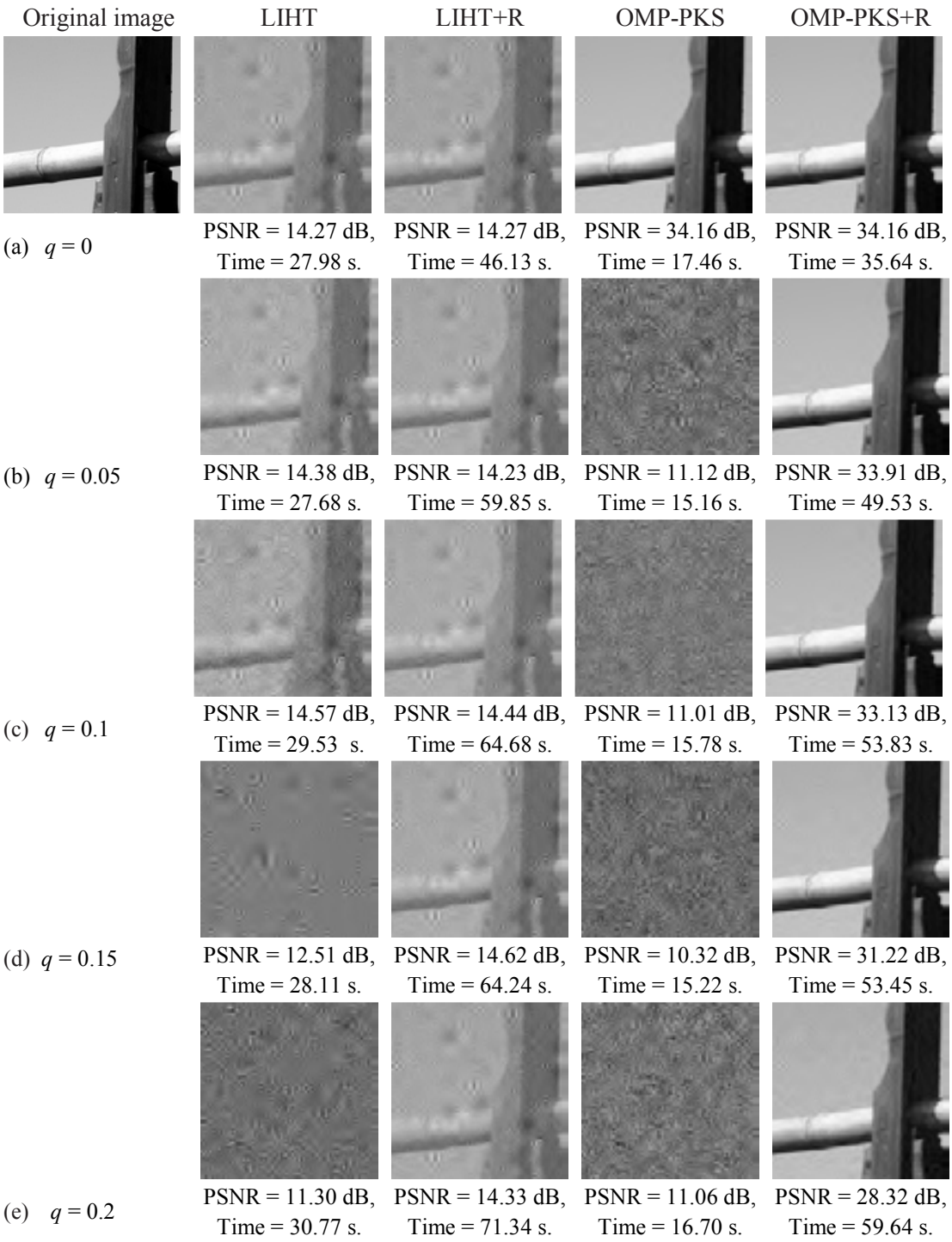

Figure 4.32: The part of the reconstructed Pillar at measurement M/N = 0.3 with the noise probability (q) of (a) 0, (b) 0.05, (c) 0.1, (d) 0.15 and (e) 0.2. The images from left to right are the original image and reconstructed images based on LIHT, LIHT+R, OMP-PKS and OMP-PKS+R, respectively.

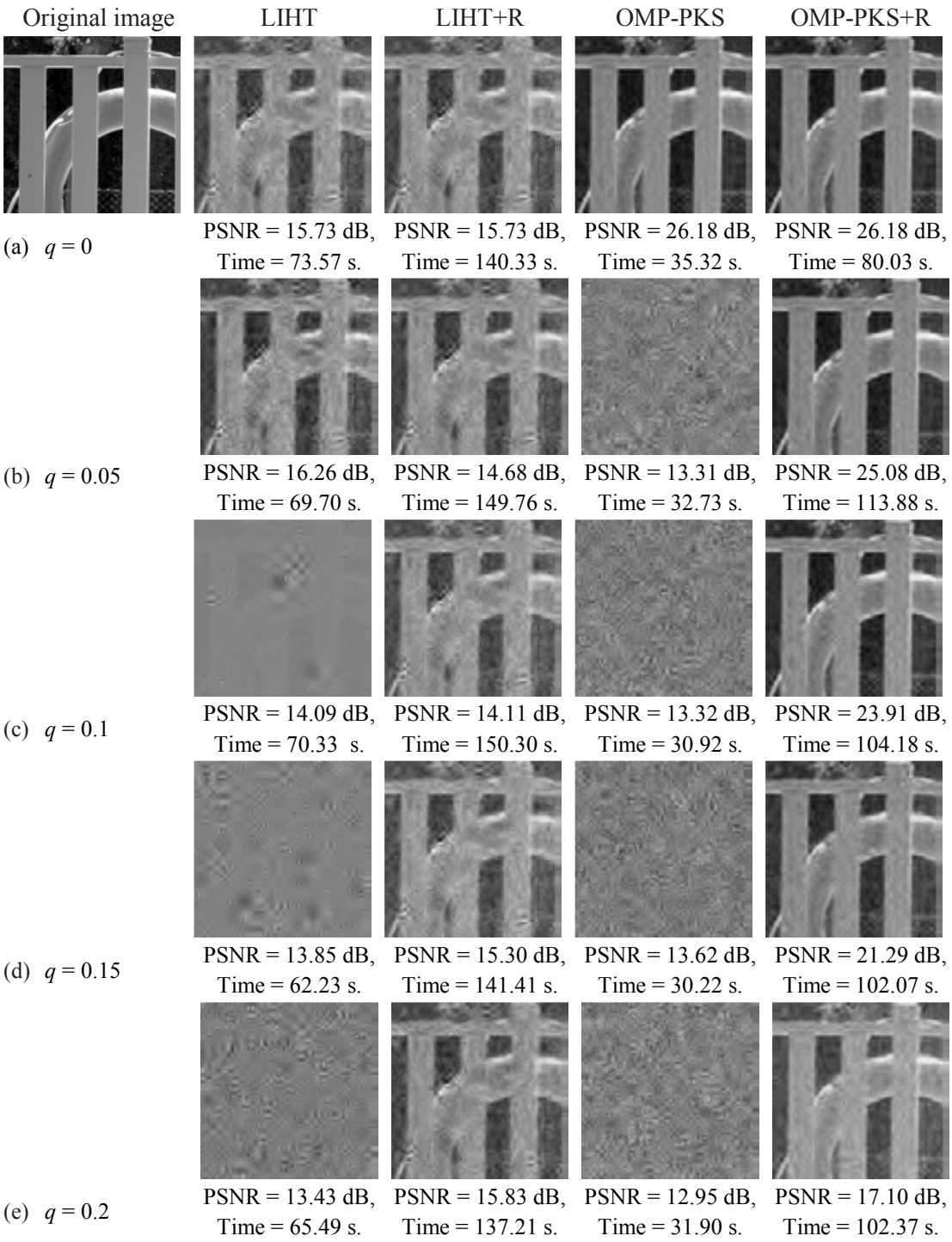

Figure 4.33: The part of the reconstructed Fence at M/N = 0.3 with the noise probability (q) of (a) 0, (b) 0.05, (c) 0.1, (d) 0.15 and (e) 0.2. The images from left to right are the original image and reconstructed images based on LIHT, LIHT+R, OMP-PKS and OMP-PKS+R, respectively.

4.4.1 Evaluation for η

In order to cope with the higher error from the Gaussian noise, more energy was allowed outside the third level subband and more data were required for the reconstruction. η was evaluated based on the percent of inaccurate rejection from **y** corrupted by both Gaussian and impulsive noises as shown in Figures 4.33-4.36. In Figures 4.34-4.37, the variances of Gaussian noise (σ^2) were 0.025, 0.05, 0.075, and 0.1, respectively. The figures shown that when σ^2 was increased; the percent of inaccurate rejection at η < 0.05 was very high. However, the trend of percent of inaccurate rejection at different values of σ^2 was the same. When the magnitude of the impulsive noise was at least 2.5 y_{max}, the values of η giving less than 0.5% inaccurate rejection was between 0.07 to 0.22. The result was in accordance with the one in the Subsection 4.3.1. Thus, the values of η was set to 0.1 in Section 4.4.2.

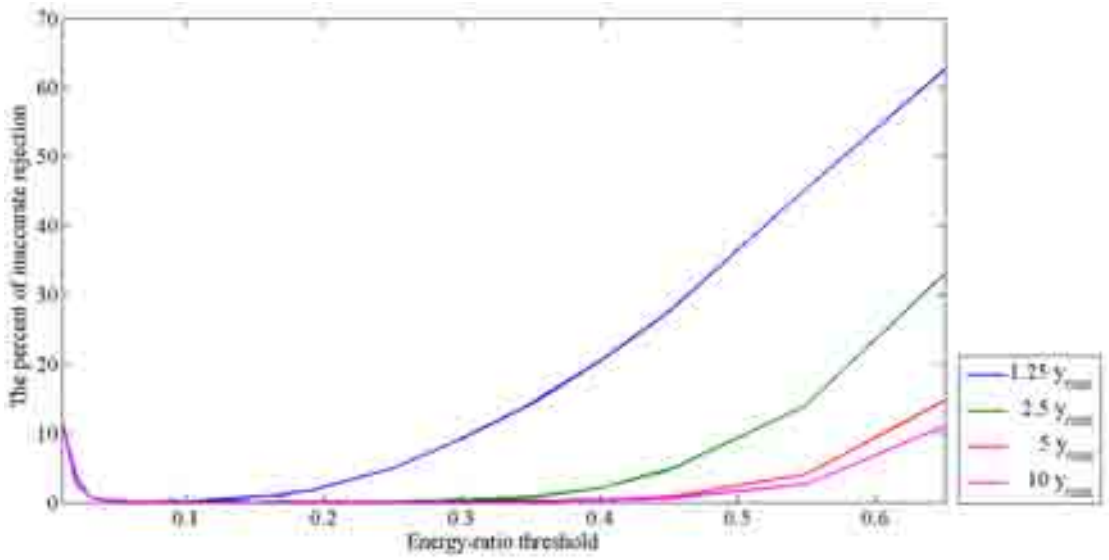

Figure 4.34: The percent of inaccurate rejection of OMP-PKS+R from **y** corrupted by Gaussian noise (σ^2 = 0.025) and impulsive noise when η was varied.

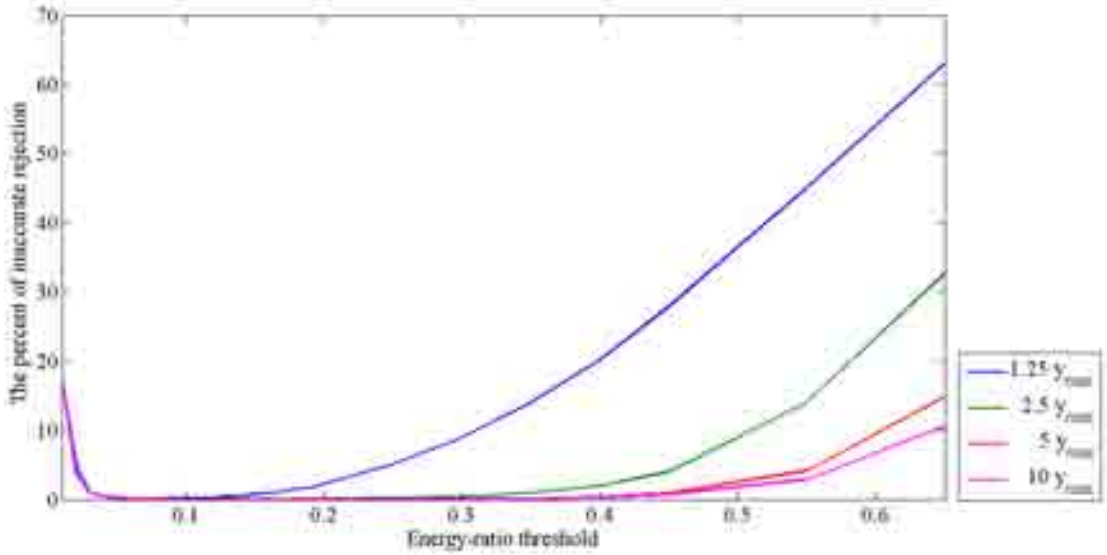

Figure 4.35: The percent of inaccurate rejection of OMP-PKS+R from **y** corrupted by Gaussian noise ($\sigma^2 = 0.05$) and impulsive noise when η was varied.

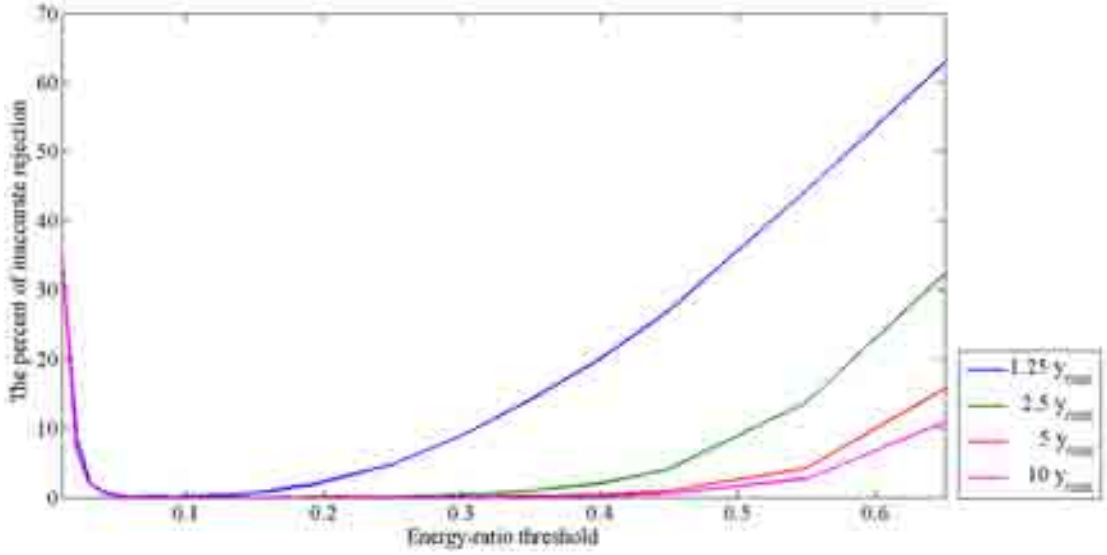

Figure 4.36: The percent of inaccurate rejection of OMP-PKS+R from **y** corrupted by Gaussian noise ($\sigma^2 = 0.075$) and impulsive noise when η was varied.

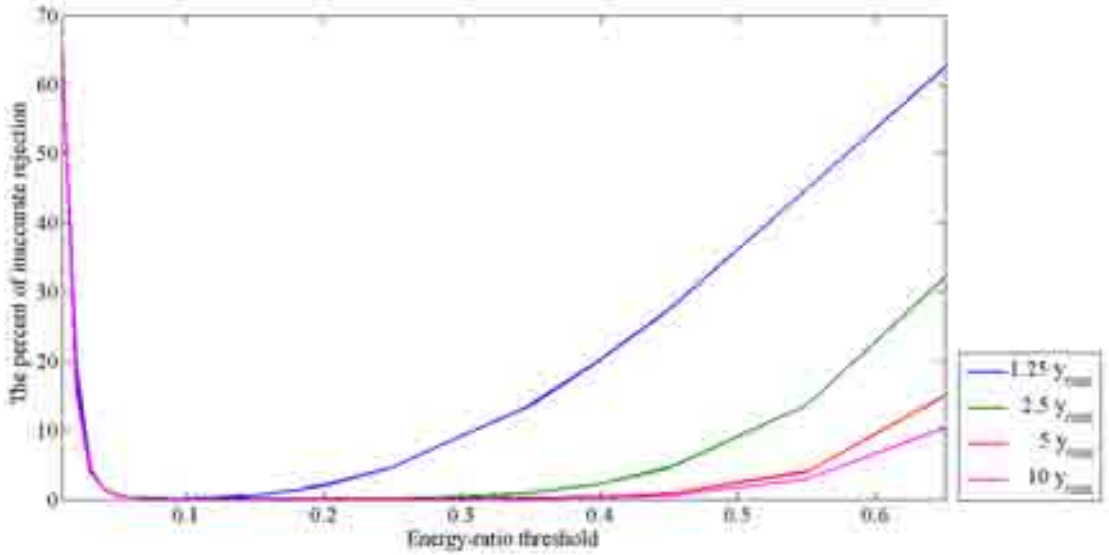

Figure 4.37: The percent of inaccurate rejection of OMP-PKS+R from **y** corrupted by Gaussian noise ($\sigma^2 = 0.1$) and impulsive noise when η was varied.

4.4.2 Performance evaluation

Figures 4.38-4.41 show the average PSNR of reconstruction images at σ^2 of 0.025, 0.05, 0.075, and 0.1, respectively. The performances of both methods were degraded by Gaussian noise. However, OMP-PKS+R+RS provided better performance over LIHT in all cases. At $q = 0.15$, there were cases that LIHT failed to reconstruct as found in Section 4.3.2. The performance of LIHT could be improved by increasing measurement rate.

Since LIHT gave the successful reconstruction when $q = 0.05$, the part of reconstruction images at $q = 0.05$, $M/N = 0.3$, and $\sigma^2 = 0.1$ were showed in Figures 4.42-4.47 for visual evaluation. The image in the first column was the original image. The second and the third columns were reconstruction based on LIHT and OMP-PKS+R+RS, respectively. The results from LIHT were noisy, while the results from OMP-PKS+R+RS were smoother with higher contrast. OMP-PKS+R+RS combined two benefits of OMP-PKS+RS and OMP-PKS+R, i.e. the tolerance to Gaussian and impulsive noise. The experiments demonstrated that OMP-PKS+R+RS gave the

successful reconstruction results in the environment corrupted by both Gaussian and impulsive noise.

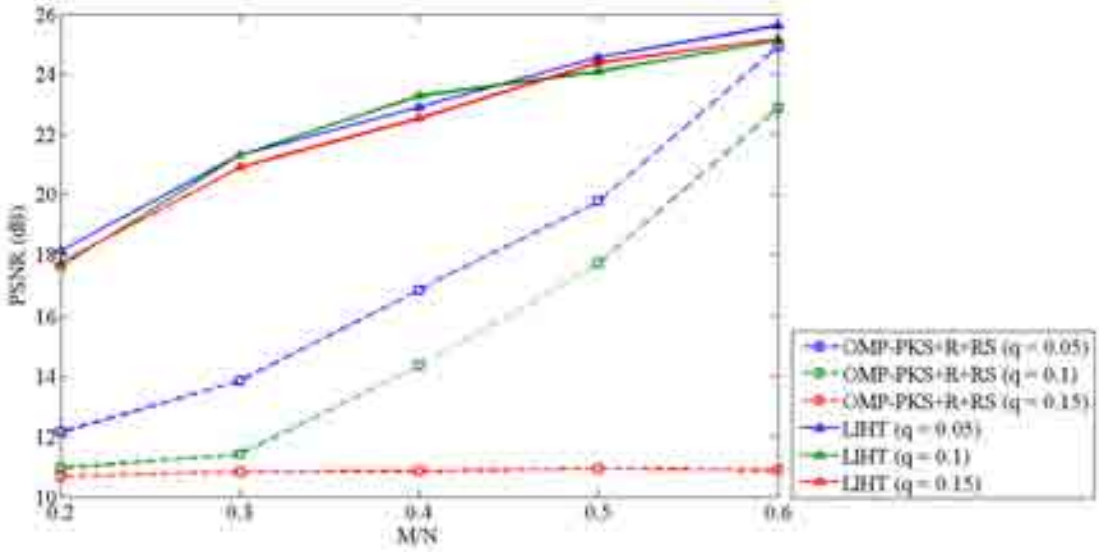

Figure 4.38: The average PNSR of reconstruction images based on OMP-PKS+R+RS and LIHT when **y** is corrupted by Gaussian noise with $\sigma^2 = 0.025$ at various M/N and q.

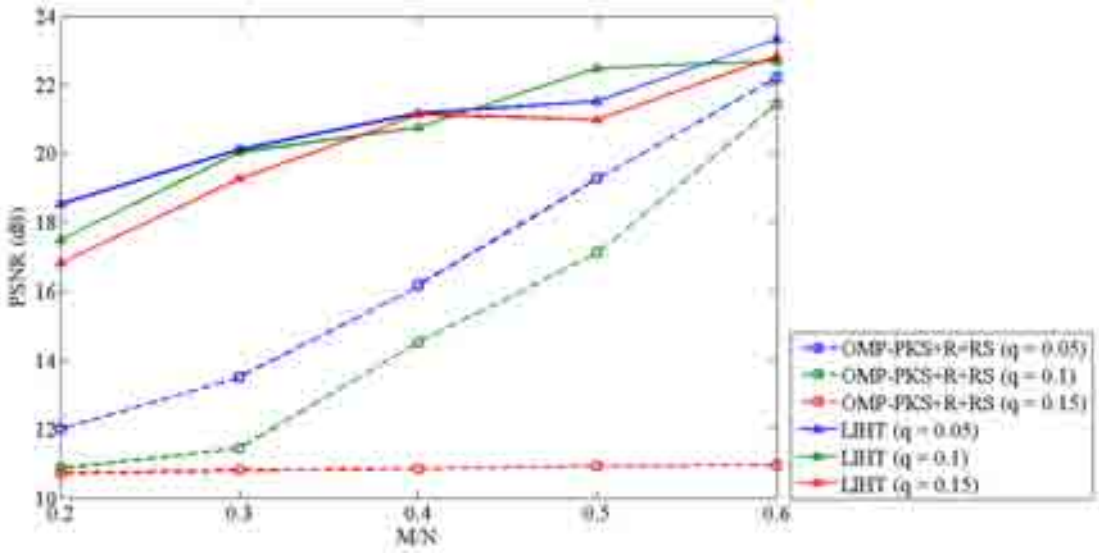

Figure 4.39: The average PNSR of reconstruction images based on OMP-PKS+R+RS and LIHT when **y** is corrupted by Gaussian noise with $\sigma^2 = 0.05$ at various M/N and q.

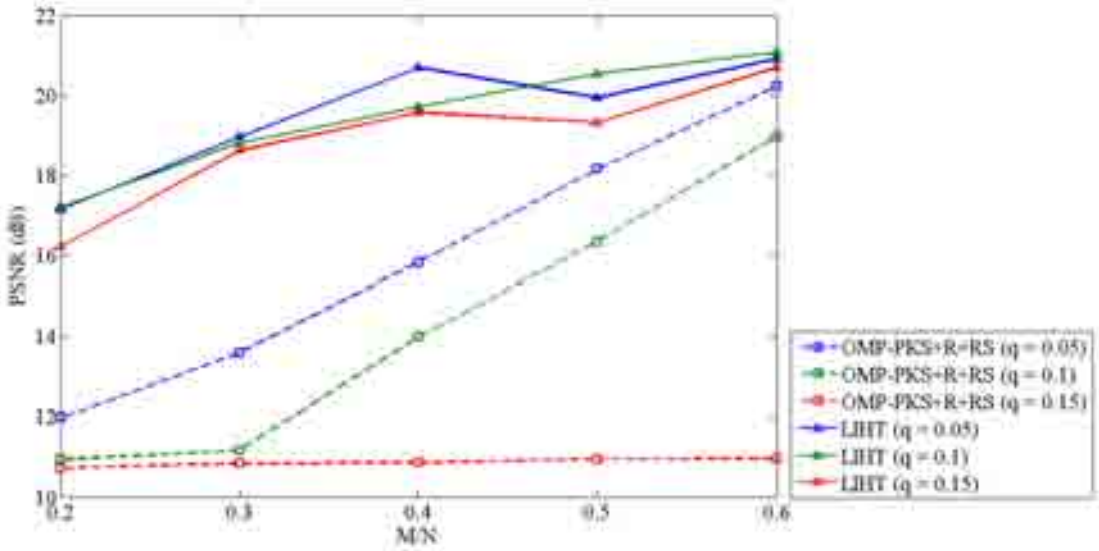

Figure 4.40: The average PNSR of reconstruction images based on OMP-PKS+R+RS and LIHT when y is corrupted by Gaussian noise with $\sigma^2 = 0.075$ at various M/N and q.

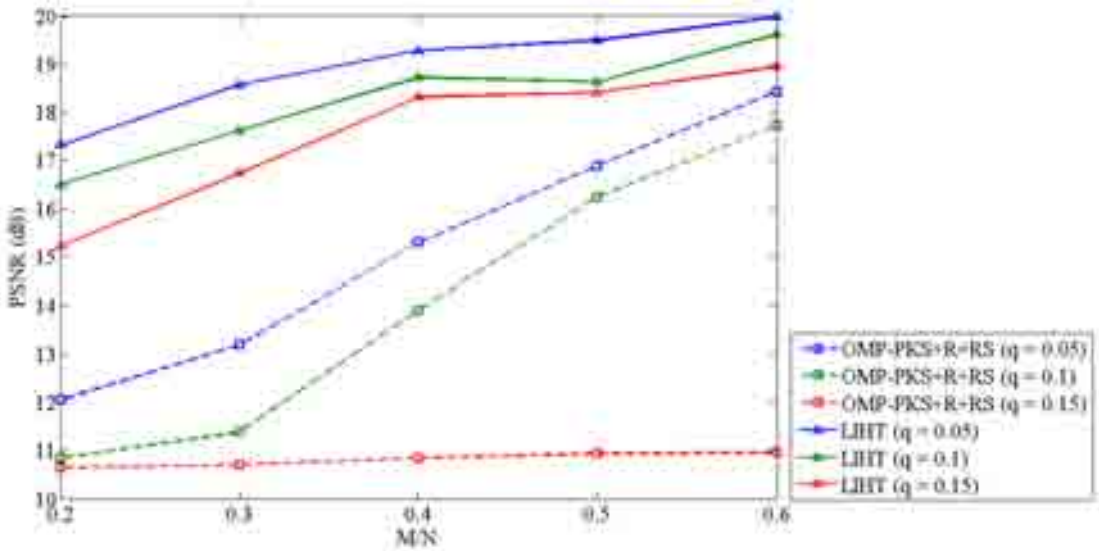

Figure 4.41: The average PNSR of reconstruction images based on OMP-PKS+R+RS and LIHT when **y** is corrupted by Gaussian noise with $\sigma^2 = 0.1$ at various M/N and q.

Figure 4.42: The part of reconstructed Peppers based on LIHT and OMP-PKS+R+RS when **y** is corrupted by Gaussian and impulsive noise at $M/N = 0.3$, $\sigma^2 = 0.1$ and $q = 0.05$.

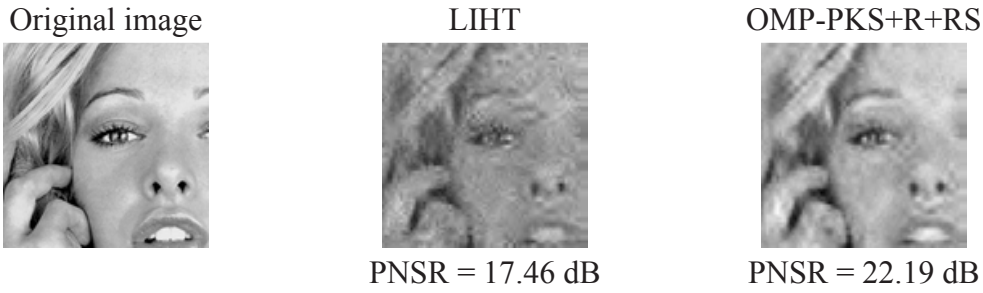

Figure 4.43: The part of reconstructed Woman based on LIHT and OMP-PKS+R+RS when **y** is corrupted by Gaussian and impulsive noise at $M/N = 0.3$, $\sigma^2 = 0.1$ and $q = 0.05$.

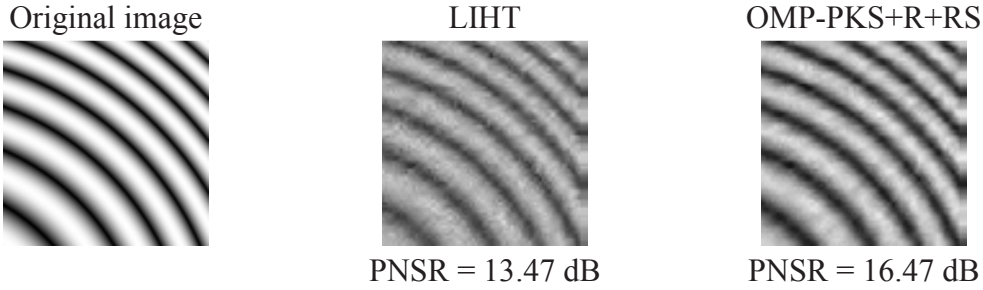

Figure 4.44: The part of reconstructed Ripple based on LIHT and OMP-PKS+R+RS when **y** is corrupted by Gaussian and impulsive noise at $M/N = 0.3$, $\sigma^2 = 0.1$ and $q = 0.05$.

Original image LIHT OMP-PKS+R+RS



PNSR = 9.91 dB PNSR = 12.59 dB

Figure 4.45: The part of reconstructed Arc based on LIHT and OMP-PKS+R+RS when **y** is corrupted by Gaussian and impulsive noise at $M/N = 0.3$, $\sigma^2 = 0.1$ and $q = 0.05$.

Original image LIHT OMP-PKS+R+RS



PNSR = 17.45 dB PNSR = 21.01 dB

Figure 4.46: The part of reconstructed Pillar based on LIHT and OMP-PKS+R+RS when **y** is corrupted by Gaussian and impulsive noise at $M/N = 0.3$, $\sigma^2 = 0.1$ and $q = 0.05$.

Original image LIHT OMP-PKS+R+RS



PNSR = 18.54 dB PNSR = 22.09 dB

Figure 4.47: The part of reconstructed Fence based on LIHT and OMP-PKS+R+RS when **y** is corrupted by Gaussian and impulsive noise at $M/N = 0.3$, $\sigma^2 = 0.1$ and $q = 0.05$.

CHAPTER V

CONCLUSIONS

5.1 Conclusions

In this dissertation, the robust CS reconstruction algorithms for images in the presence of Gaussian and/or impulsive noise are proposed. In the Gaussian noise environment, OMP-PKS+RS was proposed. It first applied random subsampling to create the ensemble of L sampled signals. Then OMP-PKS was used to reconstruct the signal. The Gaussian denoising was performed by averaging the image reconstructed from every signal in the ensemble. The experiment shows that by using the ensemble of signal, the proposed algorithm improved the PSNR of the original OMP-PKS by at least 0.79 dB. The proposed algorithm was efficient in removing the noise when the compression rate was high (small measurement rate). Moreover, OMP-PKS+RS provided higher PSNR improvement when the noise level was higher. However, the computation complexity of OMP-PKS+RS was more than OMP-PKS because it required the reconstruction of L signals instead of only one. The computational complexity is shown in Appendix A.

In the impulsive noise environment, the preprocessing method for impulsive noise rejection is proposed. In this method, the sparsified version of an image is obtained by applying octave-tree DWT using db8 as the mother wavelet. The energy distribution in wavelet domain and the capability to reconstruct the signal from an incomplete $\mathbf{y}$ are exploited in order to detect the presence of the impulsive noise. After the noise-corrupted elements are removed, the values of the removed elements are estimated. The experiment on 40 test images indicates that the proposed rejection method provided the robustness against the impulsive noise to conventional CS reconstruction methods. The performance of the impulsive noise rejection method depended on the probability of impulsive noise (q) and the magnitude of impulsive noise. Since the proposed method iteratively truncated the detectable impulsive noise element from $\mathbf{y}$, the size of $\mathbf{y}$ was smaller. When q was too high, the size of truncated

y was too small to give a successful reconstruction. Regarding the magnitude of impulsive noise, when the magnitude of the impulsive noise was very close to the maximum magnitude of **y**, the energy distribution of the reconstructed signal was not much different from the reconstructed impulsive noise-free signal. On the other hand, when the impulsive noise was large, the energy distribution was very different. It could then be concluded that there was the lower limit on the impulsive noise that the proposed rejection method could reject. From the experiment, the lower limit was set to 2.5 times of the maximum value of **y**.

Finally, the robustness of the reconstruction method against both Gaussian and impulsive noises was investigated. The combination of the proposed rejection method as the preprocessing and the reconstruction on the signal ensemble was used as the reconstruction method. The experiment indicates that the combination of the two algorithms led to the reconstruction that was robust to both Gaussian and impulsive noise.

5.2 Recommendations

1) Gaussian noise environment

- When the noise was high ($\sigma^2 \geq 0.05$), OMP-PKS+RS should be used when the fast computing time is not required. At high measurement rate ($M/N \geq 0.4$) , DCS-SOMP+ReS could be applied as the faster method at the cost of lower PSNR of the reconstruction image.
- When the noise is low ($\sigma^2 < 0.05$), the original OMP-PKS should be applied.
- The value of p in OMP-PKS+RS is set such that it is lower when the noise is higher.

2) Impulsive noise environment

- The proposed preprocessing should be applied with the (leakage) energy-ratio threshold (η) and the rejection-ratio threshold (T) are set at 0.1 and 0.4, respectively.

- The proposed preprocessing can be applied even in noiseless environment.

3) Mixed Gaussian and impulsive noise environment
   - The reconstruction should be performed by using both systems with the same recommendations as in 1) and 2).

5.3 Future research

1) Additional denoising after the reconstruction should be included to improve the performance of the reconstruction under Gaussian noise.

2) Since the computation complexity of impulsive noise rejection method was varied as q, the fast impulsive noise rejection method is the plan of our future research.

3) Characteristics of the energy distribution for general signal should be investigated in order to design the impulsive noise rejection for signals other than images.

REFERENCES

[1] D. L. Donoho. Compressive sensing. IEEE Trans. Inf. Theory 52 (4) (2006) : 1289-1306.

[2] E. J. Candes and J. Romberg. Sparsity and incoherence in compressive sampling. Inverse Problem 223 (3) (2007) : 969-985.

[3] E. J. Candes and M. B. Wakin. An introduction to compressive sampling. IEEE Signal Processing Mag. 25 (March 2008) : 21-30.

[4] F. Marvasti, A. Amini, F. Haddadi, M. Soltanolkotabi, B. H. Khalaj, A. Aldroubi, S. Sanei and J. Chambers. A unified approach to sparse signal processing. EURASIP J. on Advances in Signal Processing (2012) : doi:10.1186/PREACCEPT-1686979482577015.

[5] S. Chen, D. L. Donoho, and M. Saunders. Atomic decomposition by basis pursuit. SIAM Review 43 (1) (2001) : 129-159.

[6] J. A. Tropp. Just Relax: Convex Programming Methods for Identifying Sparse Signals in Noise. IEEE Trans. Inf. Theory 52 (2006): 1030-1051.

[7] E. J. Candes, J. Romberg, and T. Tao. Stable signal recovery from incomplete and inaccurate measurements. Comm. on Pure and Applied Math. 59 (2006) : 1207-1223.

[8] D. Needell and R. Vershynin. Uniform uncertaintity principle and signal reconstruction via regularized orthogonal matching pursuit. Foundations Comput. Math 9 (2008) : 317-334.

[9] D. Omidiran and M. J. Wainwright. High-dimensional subset recovery in noise: Sparsified measurements without loss of statistical efficiency. In Proc. CoRR (2008).

[10] E. J. Candès and T. Tao. The dantzig selector: Statistical estimation when p is much larger than n. Ann. Statist. 35 (6) (2007) : 2313-2351.

[11] D. Needell and J. A. Tropp. CoSaMP: Iterative signal recovery from incomplete and inaccurate samples. Appl. Comput. Harmonic Anal. 26 (3) (2008) : 301-321.

[12] Z. Ben-Haim, Y. C. Eldar, and M. Elad. Coherence-based near-oracle performance guarantees for sparse estimation under Gaussian noise. In Proc. ICASSP (2010) : 3590-3593.

[13] D. Needell. Topics in Compressed Sensing. Ph.D. dissertation Math. Univ. of California, 2009.

[14] T. Blumensath and M. E. Davies. Iterative hard thresholding for compressed sensing. Appl. and Comput. Harmonic Anal. 27 (3) (2009) : 265-274.

[15] T. Blumensath and M. E. Davies. Normalized iterative hard thresholding: guaranteed stability and performance. IEEE. J. Sel. Topics Sigal Process. 4 (2) (2010) : 298-309.

[16] J. A. Tropp and A. C. Gilbert. Signal recovery from random measurements via orthogonal matching pursuit. IEEE Trans. Inf. Theory 53 (12) (2007) : 4655-4666.

[17] B. Popilka, S. Setzer and G. Steidl. Signal recovery from incomplete mesurements in the presence of outliers. Inverse problems and Imaging 1 (4) (2007) : 661-672.

[18] R. E. Carrillo, T. C. Aysal aand K. E. Barner. A theoretical framework for problem requiring robust behavior. In Proc. IEEE CAMSAP (2009): 25-28.

[19] R. E. Carrillo, T. C. Aysal, and K. E. Barner. A Generalized Cauchy Distribution Framework for Problems Requiring Robust Behavior. EURASIP J. on Advance in Sigal Processing 2010 (2010) : Article ID 312989. 19 pages.

[20] R. E. Carrillo, K. E. Barner, and T. C. Aysal. Robust sampling and reconstruction methods for sparse signals in the presence of impulsive noise. IEEE J. Sel. Topics Signal Process. 4 (2) (2010) : 392-408.

[21] G. R. Arce, D. Otero, A. B. Ramirez, and J. Paredes. Reconstruction of sparse signal from l_1 dimensionality reduced cauchy random-projections. In Proc. IEEE ICASSP (2010) : 4014-4017.

[22] A. B. Ramirez, G. R. Arce, and B. M. Sadler. Fast algorithm for reconstruction of sparse signal from cauchy random projections. In Proc. EUSIPCO (2010) : 432-436.

[23] J. L. Paredes and G. R. Arce. Compressive sensing signal reconstruction by weighted median regression estimates. IEEE Trans. Signal Process. 59 (6) (2011) : 2585-2601.

[24] R. E. Carrillo and K. E. Barner. Lorentzian based iterative hard thresholding for compressed sensing. In Proc. IEEE ICASSP (2011) : 3664-3667.

[25] C. La and M. N. Do. Signal reconstruction using sparse tree representation. In Proc. of SPIE Conf. on Wavelet Applications in Signal and Image Process. 5914 (2005).

[26] C. La and M. N. Do. Tree-based orthogonal matching pursuit algorithm for signal reconstruction. In Proc. IEEE ICIP (2006) : 1277-1280.

[27] M. F. Duarte. Compressed sensing for signal ensembles. Ph.D. dissertation Dept. Elect. Eng. Rice Univ. Texas, 2009.

[28] L. He and L. Carin. Exploiting strucrure in wavelet-based Baysian compressive sensing. IEEE Trans. Signal Process. 57 (2009) : 3488-3497.

[29] D. Baron, M. B. Wakin, M. F. Duarte, S. Sarvotham, and R. G. Baraniuk. Distributed compressed sensing. Tech. Rep. TREE-0612 Rice Univ. Dept. Elect. and Com. Eng. Texas, 2006.

[30] R. E. Carrillo, L. F. Polania, and K. E. Barner. Iterative algorithm for compressed sensing with partially know support. In Proc. IEEE ICASSP (2010) : 3654-3657.

[31] M. Xu and J. Lu. K-cluster-values compressive sensing for imaging. Eurasip J. on Advance in Signal Processing 2011 (75) (2011) : 10 pages.

[32] N. V. Aravind, K. Abhinandan, V. A. Vineeth, and D. S. Suman. Comparison of OMP and SOMP in the reconstruction of compressively sensed hyperspectral images. In Proc. IEEE ICCSP (2011) : 188-192.

[33] S. G. Mallat and Z. Zhang. Matching pursuits with time-frequency dictionaries. IEEE Trans. Signal Process. 41 (12) (1993) : 3397-3415.

[34] D. L. Donoho. De-noising by soft thresholding. IEEE Trans. Inf. Theory 38 (2) (1995) : 613-627.

[35] S. Zahedpour, S. Feizi, A. Amini, M. Ferdosizadeh, and F. Marvasti. Impulsive noise cancellation based on soft decision and recursion. IEEE Trans. Instrum. Meas. 58 (8) (2009) : 2780-2790.

[36] F. Catté, F. Dibos, and G. Koepfler. A morphological scheme for mean curvature motion and applications to anisotropic diffusion and motion of level sets. SIAM J. Numer. Anal. 32 (6) (1995) : 1845-1909.

[37] L. P. Yaroslavsky. Digital Picture Processing-An Introduction. Berlin, Heidelberg : Springer Verlag, 1985.

[38] L. Yaroslavsky and M. Eden. Fundamentals of Digital Optics. Boston: Birkhauser, 1996.

[39] R. R. Coifman and D. Donoho. Translation-Invariant De-Noising, Wavelets and Statistics . New York : Springer Verlag, 1995.

[40] E. Ordentlich, G. Seroussi, S. Verdú, M. Weinberger, and T. Weissman. A discrete universal denoiser and its application to binary image. In Proc. IEEE ICIP 1 (2003) : 117-120.

APPENDICES

APPENDIX A
Computational Complexity

Table A.1. The computational cost of the *t*-th iteration in OMP.

Step	The number of multiplication	The number of L_2 optimization
1) $\lambda_t = \arg\max_{j \notin \Lambda_t} \left\langle \mathbf{r}_{t-1}, \varphi_j \right\rangle \right\vert$.	*M(N-t* +1*)*	-
2) $\mathbf{a}_t = \mathbf{\Phi}_t \mathbf{z}_t$	*Mt*	-
3) $\mathbf{z}_t = \arg\min_{\mathbf{z}} \left\| \mathbf{y} - \mathbf{\Phi}_t \mathbf{z}_{t-1} \right\|_2$	-	L_2 optimization for t variables
Total	*MN+M*	L_2 optimization for t variables

Table A.2. The computational cost of the basis preselection in OMP-PKS.

Step	The number of multiplication	The number of L_2 optimization
1) $\mathbf{z}_t = \arg\min_{\mathbf{z}} \left\| \mathbf{y} - \mathbf{\Phi}_t \mathbf{z}_{t-1} \right\|_2$	-	L_2 optimization for |Γ| variables
2) $\mathbf{a}_t = \mathbf{\Phi}_t \mathbf{z}_t$	$\left\vert \Gamma \right\vert$	-
Total	$\left\vert \Gamma \right\vert$	L_2 optimization for |Γ| variables

Table A.3. The computational cost of the *t*-th iteration in DCS-SOMP+ReS.

Step	The number of multiplication	The number of ℓ_2 optimization
1) $\lambda_t = \arg\max_{j=1,\ldots,N} \sum_{l=1}^{L} \left\| \left\langle \mathbf{r}_{l,t-1}, \varphi_j \right\rangle \right\|$.	*LM(N-t+1)*	-
2) $\mathbf{a}_t = \mathbf{\Phi}_t \mathbf{z}_t$	*LMt*	-
3) $\mathbf{z}_t = \arg\min_{\mathbf{z}} \left\| \mathbf{y} - \mathbf{\Phi}_t \mathbf{z}_{t-1} \right\|_2$	-	*L*(L_2 optimization for *t* variables)
Total	*L* (*MN+M*)	*L*(L_2 optimization for *t* variables)

Table A.4. The computational cost of the *t*-th iteration in DCS-SOMP+RS.

Step	The number of multiplication	The number of ℓ_2 optimization
1) $\lambda_t = \arg\max_{j=1,\ldots,N} \sum_{l=1}^{L} \left\| \left\langle \mathbf{r}_{l,t-1}, \varphi_j \right\rangle \right\|$.	*LpM(N-t+1)*	-
2) $\mathbf{a}_t = \mathbf{\Phi}_t \mathbf{z}_t$	*LpMt*	-
3) $\mathbf{z}_t = \arg\min_{\mathbf{z}} \left\| \mathbf{y} - \mathbf{\Phi}_t \mathbf{z}_{t-1} \right\|_2$	-	*L*(L_2 optimization for *t* variables)
Total	*Lp*(*MN+M*)	*L*(L_2 optimization for *t* variables)

Table A.5. The total computational cost of the reconstruction of a k-sparse signal by OMP, OMP-PKS, OMP-PKS+ReS, OMP-PKS+RS, DCS-SOMP+ReS and DCS-SOMP+RS.

Method	The number of multiplication	The number of L_2 optimization
OMP	$(MN+M)k$	$\sum_{t=1}^{k}(L_2$ optimization for t variables$)$
OMP-PKS	$(MN+M)(k-\lvert\Gamma\rvert)+\lvert\Gamma\rvert$	$\sum_{t=1}^{k}(L_2$ optimization for t variables$)$
OMP-PKS+ReS	$L\left[(MN+M)(k-\lvert\Gamma\rvert)+\lvert\Gamma\rvert\right]$	$L\sum_{t=1}^{k}(L_2$ optimization for t variables$)$
OMP-PKS+RS	$L\left[p(MN+M)(k-\lvert\Gamma\rvert)+\lvert\Gamma\rvert\right]$	$L\sum_{t=1}^{k}(L_2$ optimization for t variables$)$
DCS-SOMP+ReS	$L\left[(MN+M)k\right]$	$L\sum_{t=1}^{k}(L_2$ optimization for t variables$)$
DCS-SOMP+RS	$Lp\left[(MN+M)k\right]$	$L\sum_{t=1}^{k}(L_2$ optimization for t variables$)$

APPENDIX B
Publications and Presentations

[1] Parichat Sermwuthisarn, Supatana Auethavekiat, Vorapoj Patanavijit,
"A fast image recovery using compressive sensing technique with block based orthogonal matching pursuit," Proceeding of IEEE International Symposium on Intelligent Signal Processing and Communication Systems (ISPACS 2009), Kanazawa, Japan, Dec. 2009.

[2] Parichat Sermwuthisarn, Supatana Auethavekiat, Vorapoj Patanavijit,
"High frequency preserving fast compressive sensing based on wavelet block orthogonal matching pursuit," Proceeding of IEEE International Symposium on Communications and Information Technologies 2010 (ISCIT 2010), Tokyo, Japan, Oct. 2010.

[3] Parichat Sermwuthisarn, Supatana Auethavekiat, Duangrat Gansawat, and Vorapoj Patanavijit,
"Robust reconstruction algorithm for compressed sensing in Gaussian noise environment using orthogonal matching pursuit with partially known support and random subsampling," EURASIP J. on Advance Signal Processing 2012: 34 (2012).

[4] Parichat Sermwuthisarn, Duangrat Gansawat, Vorapoj Patanavijit, and Supatana Auethavekiat,
"Impulsive noise rejection method for compressed measurement signal in compressed sensing," EURASIP J. on Advance Signal Processing 2012: 68 (2012).

[5] Parichat Sermwuthisarn, Duangrat Gansawat, Vorapoj Patanavijit, and Supatana Auethavekiat,
"Robust compressed sensing Gaussian noise environment by resampling with replacement," Accepted for the International Conference on Image Processing 2012 (ICIP 2012).

VITAE

Parichat Sermwuthisarn was born in Bangkok, Thailand, in 1982. She received her Bachelor's and Master's degree in Electrical Engineering from King Mongkut Institute Technology of North Bangkok, Thailand, in 2004 and Chulalongkorn University, Bangkok, Thailand, in 2007, respectively. She received National Telecommunications Commission Fund from the Telecommunications Research Industrial and Development Institute (TRIDI) during 2009-2011. She is currently pursuing the Doctoral degree in Electrical Engineering at Chulalongkorn University, Bangkok, Thailand, since 2008. Her research areas are compressed sensing and digital image processing.